Fabrication of optoelectronic devices based on vertically aligned one dimensional ZnO nanostructures

Thesis submitted to

COCHIN UNIVERSITY OF SCIENCE AND TECHNOLOGY

in partial fulfillment of the requirements

for the award of the degree of

DOCTOR OF PHILOSOPHY

VIKAS L S

DEPARTMENT OF PHYSICS
COCHIN UNIVERSITY OF SCIENCE AND TECHNOLOGY
COCHIN - 682022, KERALA, INDIA

July 2016

Fabrication of optoelectronic devices based on vertically aligned one dimensional ZnO nanostructures

Ph.D thesis in the field of Materials Science

Author:

Vikas L S
Nanophotonic and Optoelectronic Devices Laboratory
Department of Physics
Cochin University of Science and Technology
Cochin - 682 022, Kerala, India.
Email: lsvikas.tvm@gmail.com

Supervisor:

Dr. M. K. Jayaraj
Professor
Nanophotonic and Optoelectronic Devices Laboratory
Department of Physics
Cochin University of Science and Technology
Cochin - 682 022, Kerala, India.
Email: mkj@cusat.ac.in

July 2016

Dedicated to my friends and family

Department of Physics,
Cochin University of Science and Technology,
Kochi-682022, India

Dr. M. K. Jayaraj
Professor

16th July 2016

Certificate

Certified that the work presented in this thesis entitled ***"Fabrication of optoelectronic devices based on vertically aligned one dimensional ZnO nanostructures"*** is based on the authentic record of research carried out by Vikas L S under my guidance in the Department of Physics, Cochin University of Science and Technology, Cochin 682 022 and has not been included in any other thesis submitted for the award of any degree. All the relevant corrections and modifications suggested by the audience during the pre-synopsis seminar and recommendations by doctoral committee of the candidate have been incorporated in the thesis.

Dr. M. K. Jayaraj
(Supervising Guide)

---

phone: +91 484 2577404 extn. 33 Fax: 91 484 2577595 Email: mkj@cusat.ac.in

Declaration

I hereby declare that the work presented in this thesis entitled **"Fabrication of optoelectronic devices based on vertically aligned one dimensional ZnO nanostructures"** is based on the original research work carried out by me under the supervision and guidance of Dr. M K Jayaraj, Professor, Department of Physics, Cochin University of Science and Technology, Cochin-682022 and has not been included in any other thesis submitted previously for the award of any degree.

Kochi-22 Vikas L S

16th July 2016

Acknowledgement

I take this opportunity to place on record my gratitude to a number of people, to whom I am greatly indebted and without whom I could not have finished this thesis.

First of all, I wish to express my gratitude to my supervising guide Prof. M. K. Jayaraj, who extended his care and affection throughout the tenure. He gave me a lot of opportunities to learn, experience and gain knowledge over a wide variety of technical and experimental techniques. His unconditional support and guidance helped me complete the work on time.

Prof. Joaquin Puigdollers was always there to help me, especially during my days in Universitat Politècnica de Catalunya, Barcelona. He took special care to help me with experimental facility, money, accommodation, guidance etc. I thank him for his full support and help. I also remember the help extended by Prof. Cristobal Voz, Dr. Joan Bertomeu Balagueró, Mr. Sergi Galindo, Ms. Gema Lopez Rodriguez, Prof. Ramon Alcubilla, and all members of 'Box8' and CrNe. I thank Mr. Trifon Todorov Trifonov for helping me with characterizing many of our samples in focus ion beam microscope (FIB).

I thank head of the department Prof. S. Jayalekshmi for her kind words and caring nature. I thank Prof. M. R. Anantharaman, Prof. Ramesh Babu Thayyullathil and Prof. B. Pradeep, the former heads of the department of Physics. I thank Prof. M Sabir, Prof. V.

C. Kuriakose, Dr. Titus K Mathew, Prof. Godfrey Louis, Prof. K. P. Vijayakumar and Prof. C. Sudha Kartha for their help and support.

I remember with gratitude Prof. K. P. Vijayakumar and Prof. C. Sudha Kartha, for allowing me to characterize the solar cell samples and to perform the optical response study in their lab.

It is my pleasure to thank Dr. Aldrin Antony, who was a second mentor during my work especially when I was in Universitat Politècnica de Catalunya, Barcelona. His criticism, encouragement and new ideas guided me through my research career. He was also kind enough to help me with characterizing solar cell samples in the dedicated facility at IIT Mumbai. I also thank Dr. Salini Annie for her help and support.

I acknowledge Department of science and technology (DST) and university grants commission (UGC), Govt. of India for research fellowships. I am also grateful to DST, India and Ministerio de Economía y Competitividad (MICINN), Spain for the travel grant and fellowship during my short stay at Universitat Politècnica de Catalunya, Barcelona.

I take this occasion to thank Dr. Reshmi R, Dr. Manoj R, Bharath and Gauri for the lighter moments they shared. Dr. Reshmi and Dr. Manoj were there whenever I needed help and advice, and gave me courage to overcome the hurdles right from the beginning of my PhD work.

It is with pleasure, I acknowledge Dr. Aneesh, Dr. Arun Aravind, Dr. James, Dr. Sanal, Dr. Krishnaprasad, Dr. K. J. Saji and Mr. Satish. B for their help and support. They shared their experiences which helped me a lot. I remember all my seniors in OED Lab, Dr. Sasank, Dr. Sreeja, Dr. Joshi, Dr. Asha, Dr. Anoop, Dr. Rahna, Dr. Ajimsha, Dr. Mini and Dr. Anila. I thank Dr. Vanaja K A for all the help, support and encouragement extended, right from the beginning of my PhD work. I wish to extent my sincere thanks to Anooja and Anjala.

Special thanks to Subha, Hasna, Shijeesh and Saritha for creating a wonderful lab atmosphere. Their help and support made me feel at home in OED. I remember Kurias, Anjana, Jasna, Abhayjith and Manu for the lively time in OED Lab. I remember the time spent with Aravind, Arif, Vipin and Sruthi.

I thank Mr. Ravish Jain and Mr. Monu Verma of IIT Roorkee and Mr. Girish Kunte and Mr. Varadharaja of IISC Bangalore for helping me in characterizing the samples with FESEM facility. I thank all members of office staff in Dept. of Physics, CUSAT.

I remember Dr. Ullas, Mr. Lindo, Dr. Shaju, Dr. Shaji, Dr. Manikandan for making my hostel life a memorable one. The badminton games, swimming, outings, sarotsav etc., all made my hostel life colourful.

My sincere thanks to Dr. Nijo, Dr. Priyesh, Dr. Rajeshmon, Dr. Subin, Dr. Tharanadh, Mr. Anshad and Dr. Poornima for their

support. I thank Dr. Geetha, Dr. Anand, Dr. Santhosh, Mr. Deepu, Mr. Titu, Mr. Sreejith, Mr. Sajan, Mr. Vinod, Mr. Rijeesh, Mr. Navaneeth and Mr. Jishnu for their companionship.

I would like to thank all my parish priests and other well-wishers who extended their support and advice throughout my career. I remember the prayer and advice offered by Fr. Rajadas and Fr. Shibu Joseph.

I thank all my teachers, who played a major role in shaping me. I will always remember the teaching and mentoring offered by Sujatha teacher, Suresh sir, and Dharmaraj sir. They were wonderful role models and ideal teachers and have always inspired me.

I thank my fellow teachers Dr. Dhanesh Thomas, Ms. Arya, Dr. Binu, Ms. Ayishabi, Ms. Biji, Ms. Seema and Ms. Adheena for their help and support.

It is of no doubt that the dedicated effort of my Papa, Amma and Grandfather (late) have helped me to reach this far. They painstakingly taught, corrected and nurtured me to gain knowledge & talents that I needed the most. It was the words of my parents even from my childhood, which created a spark and a strong aim inside my mind and helped me grow. Dear Papa and Amma, thank you for all your efforts.

My dear better half Mrs. Ancy P. M. is a strong supporter of mine. Her struggle and dedicated efforts compensated my absence

when I was not at home during the studies. She encouraged me and constantly kept me alert to complete the studies. Words are inadequate to thank you for your sacrifices, love, support and affection.

I remember with gratitude my in-laws Mr. Peter Thomas, Mrs. Metilda M C, Dr. Alex P. M and Mrs. Ann for understanding me and being with me during my studies. I gratefully remember Mr. Richard Benzer, Mr. Sasidharan, Mr. Jayakumar, Mr. Baiju, Mr. Salim, Mr. Salimraj, Mr. Sajeev, Mr. Vijesh, Mr. Sajil and Mr. Sajilkumar, who constantly encouraged me throughout my life. I remember my dear brothers Prajith, Swaroop, Ajeesh, Vigil Prasad, Binil Prasad, Anil Prasad, Rison and Arun for their support. I thank Dr. Sanil Kumar and Dr. Noble Gracious for their care.

With love I remember my daughter Catherine Mariya. She accepted and adjusted my absence during the final phases of my PhD studies. Her smile gave me the thrust and enthusiasm to finish the thesis at the earliest

Above all I thank God Almighty for the gift of life, health and all opportunities.

Vikas L S

Contents

Preface vii

Abbreviations used in the thesis xv

Chapter 1: An overview of ZnO one dimensional nanostructures

1.1 Introduction 01

1.2 ZnO 1D nanostructure based devices 11

1.2.1 Heterojunction 11

1.2.2 Light emitting devices 11

1.2.3 Light sensor 12

1.2.4 Gas sensor 12

1.2.5 Solar cell 13

1.2.6 Photo catalysis 14

1.2.7 Field effect device 14

1.2.8 Antireflection coating 15

1.2.9 pH sensor 15

1.2.10 Nanogenerators 16

1.2.11 Switching memory devices 17

1.3 Conclusions 17

1.4 References 18

Chapter 2: Growth and characterization techniques

2.1 Growth techniques 25

2.1.1 Solution Process 26

i Electrodeposition 28

ii Hydrothermal synthesis 30

2.2 Characterization techniques 32

2.2.1 Morphological studies 32

i Scanning Electron Microscope 32

ii Atomic force microscope 34

2.2.2 Structural characterization 39

i X-ray diffraction studies 39

a Phase analysis (θ-2θ Scan) 43

b Pole figure analysis 46

c Reciprocal space map 47

d Rocking curve 49

2.2.3 Optical Characterization 50

i Raman Spectroscopy 50

ii Photoluminescence 51

2.2.4 Electrical characterization 53

2.3 References 63

Chapter 3: Study of dependence of substrate surface on the electrochemical growth of ZnO nanorods

3.1 Introduction 69

3.2 Experimental 72

3.3 Results and Discussions 74

3.3.1 Structural studies 74

3.3.2 Optical studies 92

3.4 Conclusions 96

3.5 References 97

Chapter 4: Vertically aligned ZnO nanorod array/CuO heterojunction and its UV detector application

4.1 Introduction 101

4.2 Experimental 102

4.3 Results and Discussions 105

4.4 Conclusions 121

4.5 References 122

Chapter 5: Growth and characterization of vertically aligned ZnO nanorods over GaN:Mg substrate

5.1 Introduction 125
5.2 Experimental 127
5.3 Results and Discussions 130
5.4 Conclusions 151
5.5 References 152

Chapter 6: Study of ZnO nanorod/GaN heterojunction devices for LED and UV photodetector applications

6.1 Introduction 157
6.2 Experimental 166
6.3 Results and Discussions 169
6.3.1 Electrical properties of the heterojunction..... 169
6.3.2 Light emission from the heterojunction 175
6.3.3 UV detection 182
6.4 Conclusions 191
6.5 References 192

Chapter 7: Study of dependence of ZnO nanostructures on the light collection ability of Dye sensitized solar cells

7.1 Introduction 201

7.2 Experimental 204

7.2.1 ZnO nanoparticle preparation (Hydrothermal).. 204

7.2.2 ZnO rod preparation (Hydrothermal) 205

7.2.3 Electrodeposition of ZnO nanorod 205

7.2.4 DSSC fabrication 205

7.3 Results and discussions 208

7.4 Conclusions 212

7.5 References 213

Chapter 8: Summary and scope for future study

8.1 Summary of the present study 215

8.2 Scope for future work 218

Preface

The industrialization and the emergence of consumer electronic industry has been the driving force of the miniaturization of instruments, production of light weigt materials and flexible devices. Optoelectronic devices were also not an exception. Most recent research on optoelectronic devices includes use of nanomaterials, to reduce the size and increase efficiency. One of the major attractions of nanomaterials is the large surface to volume ratio compared to that of bulk. Though zero dimensional(0D) material has the highest surface to volume ratio the grain boundaries present in 0D material can adversely affect the electrical properties. One alternative to solve this problem is by using 1 dimensional (1D) nanostructures, which has lesser number of grain boundaries compared to 0D materials. Growth of 1D nanostructures over a substrate can also improve the charge transfer mechanism. ZnO is one of the widely studied oxide semiconductor. Though the growth of one dimensional nanostructures of ZnO is already reported, its growth over a substrate especially its alignment is rarely studied. Also electrical properties of nanorods grown over a substrate needs to be investigated thoroughly.

In this thesis the growth of nanorods by solution process over various transparent substrates have been investigated. The growth dynamics and aligned growth of nanorods were also investigated. Heterojunction devices were fabricated using these vertically aligned ZnO nanorods. Light emission and detection capabilities of the fabricated devices were also investigated. The possibility of improving the device performance is also investigated in detail.

Chapter 1 gives a brief introduction about the importance of 1D nanostructures as well as the use of 1D ZnO nanostructures. It also gives a brief review on various optoelectronic devices fabricated using ZnO 1D nanostructures.

Chapter 2 describes about various growth and characterization techniques used. Emphasis is given to solution based growth techniques to grow 1D ZnO nanostructures over a substrate. The characterisation tools like X-ray diffraction studies, FESEM, AFM, electrical characterisation etc., briefly described in this chapter. The techniques used to determine the preferred orientation of the sample including texture analysis and pole figure studies were explained here. Also other techniques

including reciprocal space mapping and rocking curve analysis is discussed.

Chapter 3 deals with the growth of ZnO nanorods via electrodeposition over TCO coated glass substrates. A brief introduction on electrodeposition of 1D ZnO nanorods is provided. Four different kind of TCO coated substrates viz., SnO_2:F coated glass substrate, ITO coated glass substrate, ITO coated PET substrate and ZnO:Al substrate were used for the growth of 1D nanostructures. The dependence of surface properties on the 1D nanostructure growth is thoroughly investigated. To study the dependence of seed layer over the substrate, sputter deposited ZnO layer of varying thicknesses of 5 nm, 10 nm, 20 nm, and 30 nm were used. The texture coefficient shows nearly random oriented growth of ZnO on FTO substrate and preferred oriented growth along (0002) orientation over other substrates. Based on the substrate surface studies using AFM, it is concluded that the growth can be classified into two categories, i) growth of nanostructures over a lattice matched substrate, ii) growth of nanostructures over a substrate with lattice mismatch. It is observed that for lattice matched substrate the preferred orientation and nanorod dimensions are independent on surface roughness, whereas for substrate with lattice mismatch, the

surface roughness decreases the preferred orientation. Based on the observations a model for 1D nanostructure growth is proposed.

Chapter 4 describes study on ZnO nanorod/CuO based heterojunction. Since highly crystalline vertically oriented ZnO nanorods were grown over various substrates including ZnO:Al (AZO), a heterojunction based on these nanorods (ZnO nanorod/CuO) were fabricated to investigate the electrical properties of the device. p-type CuO sputter deposited on as grown n-type 1D ZnO nanostructures to obtain a p-n heterojunction. Devices with and without intermediate seed layer over the TCO substrate were fabricated to study the effect of seed layer on the electrical properties of the heterojunction. The device showed good rectification ratio of 50 and a series resistance of 17 kΩ. The seed layer in this case is giving an additional series resistance by acting as an electron blocking layer. The device responded to UV light and the device performance is studied. The device showed a bi exponential dependence on response to UV light. Two rise time constants of 68s and 220 s and two decay time constants of 179 s, and 2986 s were observed for the fabricated device. The heterojunction showed highly selective

response for UV region with virtually no response to visible radiation.

Chapter 5 describes the growth of ZnO nanorods by hydrothermal synthesis. Previous studies concluded that it is possible to grow 1D nanostructures vertically aligned over a substrate. The electrical studies revealed that p-n heterojunction interface can deteriorate the electrical performance of the fabricated device. To solve this issue, 1D ZnO nanostructures were grown directly over a lattice matched c-cut GaN:Mg p-type substrate. Two sets of substrates, one with ZnO seed layer and one without seed layer on GaN:Mg substrate were used to grow the nanorods by hydrothermal synthesis. Highly compact vertically aligned ZnO nanorods are obtained when nanorods are grown directly over the substrate, and hexagonal rods with some tilting is observed when nanorods are grown over seed layer coated substrate. X-ray diffraction studies of the samples including rocking curve, reciprocal space mapping and pole figure analysis were performed. It is found that introduction of seed layer adversely affects the preferred oriented growth of nanorods. A post deposition annealing is improving the crystalline quality. Growth of ZnO nanorods directly over GaN:Mg substrate along

with post deposition annealing, resulted in epitaxial growth of ZnO nanorods with c-axis vertical to substrate surface.

Chapter 6 investigates the fabrication and characterisation of ZnO nanorod/GaN heterojunctions. Since highly oriented growth of n-ZnO nanorods were obtained via hydrothermal synthesis directly over a p-GaN:Mg substrate, its electrical performance is also investigated. The electrical studies of the best device showed a knee voltage of 2.6 V and a series resistance of 12.29 kΩ. Based on the electrical studies a band diagram for the device is proposed. The device emitted light under both forward and reverse bias. Under forward bias the emission from as grown nanorods showed near white emission. On annealing the emission colour shifted to blue region. The samples with highly crystalline ZnO nanorods also gave intense UV emission. It is seen that changing the defect states in the ZnO nanorod changes the emission colour. Devices also showed emission under reverse bias. An increase in junction current is observed on illuminating with UV light. The response parameters extracted from the studies showed a response in microsecond time scale. A response time of around 300 μs was observed for the best heterojunction device. The present report gives similar response time as that of the fastest device reported so far, which used a

much expensive CVD technique to grow ZnO nanorods. The heterojunction fabricated in the present study is the fastest UV detector for a solution grown ZnO nanorod.

Chapter 7 explains the light collection ability of various ZnO based nanostructures. Three types of ZnO based structures, including a hydrothermally synthesized ZnO rod, electrodeposited ZnO rod and a hydrothermally grown ZnO nanoparticle were used to fabricate dye sensitized solar cells. DSSCs fabricated using ZnO nanostructures along with N719 dye showed similar shape of external quantum efficiency (EQE) response as that of a reference DSSC fabricated using TiO_2 nanoparticle. Among various nanostructures of ZnO hydrothermally synthesized rods have maximum external quantum efficiency. Electrodeposited ZnO rod based DSSC showed minimal response in visible region, which may be due to the high transparent nature of the device. The hydrothermally synthesized rod based DSSC had an open circuit voltage of 590 mV and a fill factor of 56.5%, which is comparable with TiO_2 particle based reference solar cell.

Chapter 8 summarizes the main results in the thesis along with the scope for future work.

Abbreviations used in the thesis

Abbreviation	**Expansion**
ϑ	Angle between incident X-ray and surface of sample
Γ	Phonon mode
0D	Zero dimensional
1D	One dimensional
2D	Two dimensional
2ϑ	Angle between diffracted X-ray and incident light
3D	Three dimensional
AFM	Atomic force microscope
Al	Aluminium
Ar^+	Argon ion
Au	Gold
AZO	ZnO:Al
CIE	Commission Internationale d'Eclairage (International Commission on Illumination)
CTAB	Cetyltrimethyl ammonium bromide
CuO	Copper oxide
CVD	Chemical Vapor deposition
DVP	Direct Vapour Phase
E_c	Conduction band minimum
EDA	Ethylene diamine

EDTA	Ethylene diamine tetra acetic acid
E_g	Band gap
EL	Electro luminescence
E_v	Valence band maximum
eV	Electron volt
FESEM	Field emission scanning electron microscope
FTO	Tin oxide doped with Fluorine
GaN	Gallium Nitride
He-Cd	Helium Cadmium laser
I^-/I^{3-}	Iodide triiodide couple
ICSD	Inorganic crystal structure database
I_d	Dark current
I_l	Current in light
ITO	Tin doped Indium oxide
KCl	Potassium Chloride
LO	Longitudinal optical
MBE	Molecular beam epitaxy
MOCVD	Metal oxide chemical vapour deposition
n	Ideality factor
N719	Name of dye used for DSSC
NaOH	Sodium hydroxide
NH_4OH	Ammonium hydroxide
Omega	Angle between incident X-ray and surface of sample + offset
PEG	Polyethylene glycol

PET	Poly ethylene terephthalate
PL	Photoluminescence
Pt	Platinum
PVA	Polyvinyl alcohol
PVP	Polyvinyl propylene
Q_x	Reciprocal axis
Q_y	Reciprocal axis
RMS	Root mean square
R_s	Series resistance
SDS	Sodium dodecyl sulphate
SEM	Scanning electron microscope
t_1, t_2	Decay time constants
TCO	Transparent conducting oxide
T_{hkil}	Texture coefficient for (hkil) plane
TO	Transverse optical
UV	Ultra Violet
V-I or I-V	Voltage-current or Current-voltage
VLS	Vapour liquid solid technique
XRD	X-ray diffraction
$Zn(CH_3COO)_2$	Zinc acetate
ZNA	ZnO nanorod Array
$ZnCl_2$	Zinc Chloride
ZnO	Zinc Oxide

Publications related to the work presented in the thesis

Journal publications

1. Fast UV sensing properties of n-ZnO nanorods/p-GaN heterojunction. **L. S. Vikas**, K A Vanaja, P P Subha, M K Jayaraj, Sensors and Actuators A: Physical 242, 116 (2016).

2. Defect-assisted tuning of electroluminescence from p-GaN/n-ZnO nanorod heterojunction. **L. S. Vikas**, C K Sruthi, M K Jayaraj, Bulletin of Materials Science 38(4), 901 (2015).

3. Vertically aligned ZnO nanorod array/CuO heterojunctions for UV detector application. **L. S. Vikas**, K C Sanal, M K Jayaraj, A Antony, J Puigdollers, Physica status solidi (a) 211(11) 2493 (2014).

4. Substrate surface dependence on electrochemical growth of aligned ZnO nanorods. **L. S. Vikas**, M K Jayaraj (to be communicated)

5. X-ray diffraction studies on epitaxially grown ZnO nanorods over Mg:GaN substrate. **L. S. Vikas**, M K Jayaraj (to be communicated)

Other publications which author has contributed

1. Growth and characterization of p-ZnO: Cu thin film and its homojunction application, AC Saritha, MR Shijeesh, **L. S. Vikas**, Rajeev R Prabhu, and MK Jayaraj, Journal of Physics D: Applied Physics 49, 295105 (2016)
2. Room temperature deposited transparent p-channel CuO thin film transistors , K. C. Sanal, **L. S. Vikas**, and M. K. Jayaraj, Applied surface science 297, 153 (2014).
3. Degradation study and calculation of density-of-states in PTCDI-C8 channel layer from the electrical characteristics of thin-film transistors, Methattel R Shijeesh, **L. S. Vikas**, MK Jayaraj, and J Puigdollers, Journal of Applied Physics 116, 0204507 (2014)
4. Comparative study on degradation and trap density-of-states of p type and n type organic semiconductors, MR Shijeesh, **L. S. Vikas**, MK Jayaraj, and J Puigdollers, SPIE Organic Photonics + Electronics 918519 (2014)
5. Growth of vertically aligned ZnO nanorods on various substrates by hydrothermal method, P. M. Aneesh, P. P. Subha, **L. S. Vikas**, S. Mohan, and M. K. Jayaraj SPIE NanoScience+ Engineering 77606 (2010)

Conference presentations

1. Synthesis and characterization of titanium dioxide nanotube arrays by anodization, **L. S. Vikas**, P P Subha and M. K.Jayaraj, National review and coordination meeting of nano mission council, 2011, New Delhi.

2. Work function measurements of transparent conducting ZITO films by Kelvin Probe Microscopy, César Moreno, Sergi Galindo, Cristobal Voz, Joaquim Puigdollers, Aldrin Antony, Paz Carreras, Joan Bertomeu, **L. S. Vikas**, M.K.jayaraj, Nanosolar 2012, Cochin.

3. Electrodeposited Vertically aligned ZnO nanorods for possible Solar cell applications, **L. S. Vikas**, M K Jayaraj, Nano India 2013, Thiruvananthapuram.

4. Electrochemical Synthesis of Aligned ZnO Nanorods and its application for Dye Sensitized Solar Cells. **L. S. Vikas**, M K Jayaraj, Joaquim Puigdollers, Monica Della Pirriera, Pau Bosch-Jimenez, 2nd International conference on advanced functional materials (ICAFM 2014), Thiruvananthapuram.

5. Double transducing property of n-ZnO nanorod/p-GaN heterojunction. **L. S. Vikas**, C K Sruthi, P P Subha, K A Vanaja, M K Jayaraj (ICEEE 2015), Kochi.

6. Fast UV sensing by vertically aligned ZnO nanorods, **L. S. Vikas**, M K Jayaraj, Nano India 2015, Thanjavur.

7. ZnO nanorod based fast UV detector: Fabrication & Characterization, **L. S. Vikas**, M K Jayaraj, Advances in Scientific and Industrial instrumentation (2016) Kochi.

Chapter 1

An overview of ZnO one dimensional nanostructures and devices

1.1 Introduction

Twenty first century witnessed major breakthrough in consumer electronics. Emerging technologies are looking for smaller, efficient, light weight devices. In the case of electronic devices, a major change was triggered when the concept of integrated circuit was introduced by J. S. Kilby and Robert Noyce in 1959[1–7]. Similarly, studies by Z. I. Alferov in the 1960s gave the idea of heterojunction devices[8]. Kilby, Z. I. Alferov and H. Kroemer were awarded the Nobel prize for Physicsin 2000, for originating compact, faster and efficient optoelectronic devices. Their studies helped to shrink powerful electronic devices like computers to small sizes that can fit into our pockets today. In-order to fabricate such compact electronic devices, thin film growth techniques are being used in its various development stages. The most recent

trend is to use materials with nanoscale dimensions in electronic devices. Intel has developed a series of processors with technology node 32 nm, 22 nm, 14 nm etc. which are available in the market today. Coordinated research is being undertaken to scale down the devices with 10 nm, 7 nm and 5 nm node technology to keep pace with the international technology roadmap for semiconductor(ITRS). The recent size reduction of processors became successful due to the new 3D transistor concept[9–12]. These advancements are pushing material science to search for the possibilities of new materials and their applications.

Materials with reduced size in any or all the three directions in the range 1-100 nm are called nanomaterials. The technology associated with fabrication and application of such nanomaterials is called 'nanotechnology'. One of the major attractions of nanomaterials is that, it has increased surface to volume ratio. Because of this, the properties and capabilities of nanomaterials can differ from those of the bulk. Hence to fabricate an optoelectronic device, which is fast, powerful, inexpensive and compact, these nanomaterials has to be designed for specific properties. All the developments in nanotechnology made possible after the development of scanning tunnelling microscope (STM) by Gerd Binning and Heinrich Rohrer in 1981. Their studies helped to fabricate, characterize and visualize nanomaterials. Later the STM was modified with different probing techniques generally known as scanning probe microscopy (SPM) which includes atomic force microscope (AFM),

Kelvin probe force microscope (KPFM), magnetic force microscope (MFM), lateral force microscope (LFM) etc. These are helpful to monitor different types of nanomaterial interactions and study them. Recent developments on electron microscopes such as field emission scanning electron microscope (FESEM), high resolution transmission electron microscope (HRTEM) and focused ion beam microscope (FIB) are helpful for viewing and studying these nanomaterials in detail. Apart from surface morphology, it is now possible to analyse the chemical properties, crystallinity and electrical properties of these nanomaterials. The techniques like nanoindentation and nanomanipulators offers flexibility in handling with very small dimensional materials and structures. These advances in nanotechnology helped to create materials with desired structure including metamaterials. The possibility offered by nanotechnology is endless, choosing the right material and technique for the synthesis of nanomaterial is the key parameter. Material scientists have been exploring these new properties and functionalities offered by the nanotechnology.

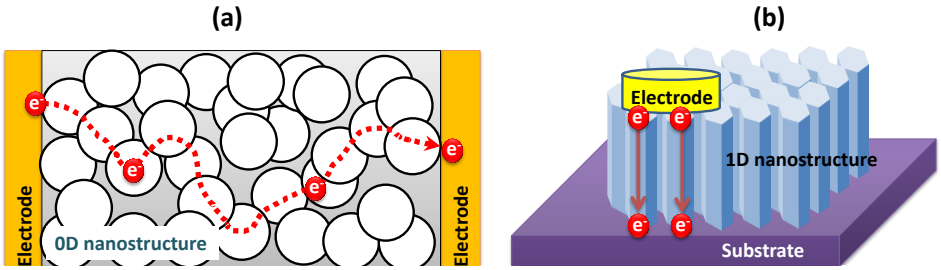

Figure1.1: Schematic representation of electron transport in (a) zero dimensional and (b) one dimensional nanostructures.

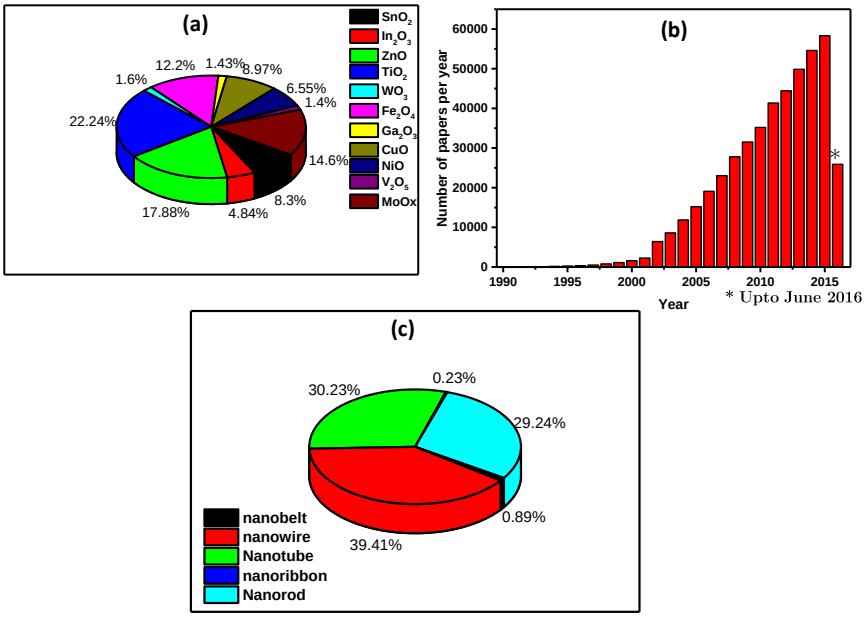

Figure 1.2: (a) Contribution of publications based on various oxide materials in the last 25 years. (b) Number of publications per year for ZnO nanomaterial based devices. (Data collected from webofknowledge.com via keyword search)

The increased surface to volume ratio is the major change associated with nanostructures, compared to their bulk counterpart. The increased surface to volume ratio gives new capabilities like high reaction rate, increased catalytic activity, novel material properties etc. One major drawback of various shapes of nanostructures is its grain boundaries, especially when these nanostructures are used for optoelectronic applications. During

the working of an electronic device, electrons need to pass through the network of nanomaterials, and hence the electrons are confronted with a large number of grain boundaries. In a typical electronic device for each electron transfer between the electrodes, the electron usually passes thousands of grain boundaries, as shown in figure 1.1. The presence of grain boundaries can adversely affect the electrical properties of the device. One way to reduce the number of grain boundaries is to use 1D nanostructures. Since the number of grain boundaries in 1D nanostructures are much lesser compared to 0D nanostructures and practically nill when conduction is along the length of the 1D nanostructure. Hence, 1D nanostructure based devices can show better electrical performance.

When we look at the spectrum of materials used for various optoelectronic applications, the oxide materials are the prominent ones. Metal oxides are formed by the combination of oxygen with suitable metal. Typically oxygen acts as anion and metal acts as cation. Metal oxides possess high chemical and temperature stability. The boiling point of such materials is high of the order of 1000 ℃. Oxide materials especially metal oxides are used in variety of applications including piezo electronic devices, superconducting materials, magnetic materials, electronic circuits, fuel cells, catalysis, solar cells, gas sensors, etc.

Oxide materials are in general insulators. They possess filled valence band and empty conduction band. According to band structure studies, transparency and conductivity are contradicting properties, hence a material cannot possess both. For a material to be metallic the Fermi energy level of the material should lie within a band having a large density of states. Hence to obtain conductivity, we may sacrifice transparency. But certain materials provide a possibility to combine the transparency and conducting properties together. In_2O_3, SnO_2, ZnO, CdO etc. are such transparent conducting oxide materials. Intrinsically these materials are insulators with band gap greater than 3eV. Degenerate doping can be employed in these materials to lift the Fermi energy level near to conduction band. Degenerate doping can increase mobility of carriers without affecting its transparency. Thus observation of increased carrier concentration and transparency in oxide materials created a new class of materials called transparent conducting oxides (TCO). TCO materials helped to create high definition (HD) display devices including liquid crystal display (LCD), plasma and organic light emitting diode (OLED) televisions etc. TCOs are used in photovoltaic devices as window layer which also acts as an electrode. Recent research in consumer electronics mainly focuses on developing all transparent electronic devices which are flexible and wearable too.

Yet another approach in semiconductor industry is to make devices flexible. Poor flexibility and transparency of Si and Si

based devices make it difficult to create flexible devices with existing technology. Oxide materials can be made flexible. The high transparency of oxide materials can make devices like displays, touch screen devices, photovoltaic devices flexible and convenient. In this context study on the above mentioned oxide materials are highly relevant.

The number of publications in the last 25 years on various oxide materials have increased tremendously, out of which the major contribution is on zinc oxide (ZnO). ZnO is a multifunctional material with high thermal, chemical and photostability. The melting point and boiling point of ZnO is nearly 1975 and 2360 °C respectively. It is insoluble in water under normal conditions. Unique physical and chemical properties of zinc oxide allowed it to be used in cosmetic industry, rubber processing, textile manufacturing, pharmaceutical, photovoltaic, electronic applications, etc. It is also used as an additive in numerous places like ceramics, plastics, glass, cement, paints, pigments, food, adhesives, temperature resistant windows etc.

The investigations on nanomaterial based ZnO is increasing over the years. The last 25 years saw gradual growth, and after 2000, a steep increase in the number of publications (figure1.2 (b)). It is mainly due to the technological advancements in the field of nanotechnology. The recent interest is on one dimensional nanostructures of ZnO. Figure 1.2(c) gives the spectrum of 1D

nanostructures already reported (for the past 25 years). Recent reports concentrates on 1D ZnO nanostructured based device applications rather than material synthesis and their characterisation. Increased surface area and lower number of grain boundaries make them a suitable choice.

Zinc oxide is a II-VI binary oxide semiconductor material. It has a wide band gap of 3.3eV and an exciton binding energy of 60 meV. The high exciton binding energy of ZnO makes it suitable for room temperature optoelectronic applications. ZnO also is being used as a transparent conducting material. ZnO has a direct band gap which can be tuned by alloying with other suitable materials. Inherent defects in ZnO usually make it an n-type semiconductor. There are reports on realising p-type conductivity in ZnO. Even though some achieved p-type conductivity in ZnO with extrinsic dopants such as Li, Na, N, P, As etc., the stability and reproducibility is still a challenge. Electron mobility in ZnO ranges up to about ~250 $cm^2/(V\ s)$ and the hole mobility is up to few 10s of $cm^2/(V\ s)$ [13].

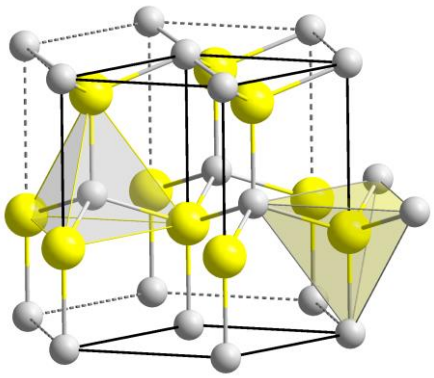

Figure 1.3: Structure of ZnO unit cell. (*Source commons.wikimedia.org*)

ZnO can crystallize in any of the three forms viz. wurtzite, zinc blend or rocksalt. The stable phase of ZnO in ambient conditions is wurtzite ZnO. The schematic representation of hexagonal wurtzite ZnO unit cell is as shown in figure 1.3. The hexagonal structure of ZnO belongs to C_{6v}^{4} space group with two formula units in one primitive cell[14]. The lattice parameters of ZnO are a=b=3.249 Å and c=5.178 Å. The valence band and conduction band of ZnO are formed by the filled 2p level of O^{-} and empty 4s levels of Zn^{++} ions respectively. The energy band structure is created by the mutual interaction of neighbouring molecules. The non-centrosymmetric structure of wurtzite ZnO makes it a piezoelectric material. The piezoelectric nature of ZnO makes it a direct

choice for self-powered systems. Even nanostructured ZnO is recently reported to be used for self-powered device applications.

ZnO is a material which is known for ages and for many applications at present uses ZnO in one or another form. ZnO is a non-toxic material even used as food additive. ZnO is generally insoluble in water. Since ZnO is an amphoteric oxide which reacts with both alkali and acid, it is preferred for many special applications like pH monitors. Thin film form of ZnO was used for many applications including transparent conducting oxides, window/conducting layer in solar cells, thin film transistors, gas sensors, etc. Though processing of ZnO started near the mid of last century, a focussed effort on study of ZnO nanostructure fabrication was started by 1990 only. Nanotechnology offers many unexplored areas for the development of materials to be utilized in practical applications. Earlier studies on ZnO nanostructures concentrates on fabrication of ZnO nanostructures with different shapes such as nanotube, nanorod, nanoribbon, nanoclusters, nanoflowers, etc. Recently serious efforts and thorough investigation on application of these nanostructures for practical uses have been initiated. Some of the major applications of ZnO 1D nanostructures are briefly reviewed in following sections.

1.2 ZnO 1D nanostructure based devices

1.2.1 Heterojunction

Majority of ZnO 1D structure based devices reported so far utilizes a heterojunction device structure. An n-type semiconductor along with a p-type semiconductor is used to fabricate heterojunction devices. In general synthesized ZnO nanostructures show n-type conductivity even without doping due to various defect states. There are several studies on formation of p-type ZnO semiconductors with[15,16] and without[17] doping. The stability, reproducibility, controllability etc. are critical issues in p-type ZnO nanostructure. Hence most of the ZnO based heterojunction devices utilize n-type conductivity of ZnO. A suitable p-type material like CuO[18–20], GaN[21,22], p-Si[23,24], NiO[25,26] etc. is used to fabricate the heterojunction. ZnO 1D nanostructures are also used in hybrid heterojunctions using organic polymer layers[27,28].

1.2.2 Light emitting devices

Light emission from a ZnO 1D nanostructure based devices generally utilizes heterojunction device structure. The emitted light energy usually depends on the various energy levels associated with the materials used for device fabrication. Hence by tuning the material properties the emission colour of the device can be tuned. Apart from heterojunction device structure, white light

emission from a Schottky device is also reported [29]. More detailed review on light emitting diodes is given in chapter 6.

1.2.3 Light sensor

Similar to light emission devices light senor application also utilises the heterojunction device structure. Along with heterojunction structure resistive devices are also reported to be efficient detectors. In any case, the light absorption creates additional charge carriers inside the device, which led to an increased current. The increase in junction current is usually taken as an indicator of the presence of light. Fastest light sensors showed micro seconds response time. As the band gap energy of ZnO matches with UV wavelength region, most of the light sensors show selective UV response. More details on these aspects are discussed in chapter 6.

1.2.4 Gas sensor

Earlier studies on gas sensors utilize thin film form of ZnO for gas sensor applications. ZnO thin film has response to humidity [30,31], CO [32], H_2 [33], H_2S [34] etc. ZnO 1D nanostructure based devices were used for gas sensor applications in 21st century only. Vertically aligned ZnO nanorod array showed good electrical response on exposure to O_2 and NO_2 environment. These devices have very good sensitivity and can even detect gas as low as 4 ppm. The device also showed linear response to both O_2 and NO_2 gases [35]. The presence of UV light enhances the sensing proper-

ties of the device as UV light decreases the amount of adsorbed oxygen on the surface of ZnO and hence the conductivity increases [36], which is also the mechanism in thin films [37]. In general ZnO nanorod based gas sensors can work at high temperature.

Functionalizing the surface of 1D nanostructures with suitable materials enhances the selectivity and response of the gas sensor. Decoration with noble metal like Au [38], Ag, Pd, Pt etc. enhances the sensitivity as well as selectivity of ZnO based gas sensors. The gas sensing characteristics of ZnO can also be improved by forming heterojunctions using metal oxides such as CuO, NiO etc. ZnO 1D structures were coated with organic materials like stearic acid, lysine, dodecanedioic acid, mercaptoacetic acid and perfluorotetradecanoic acid to enhance its sensitivity to oxygen [39]. Similarly, functionalisation with tris(hydroxymethyl)amino methane enhances the sensitivity of the device to NO_2 [40].

1.2.5 Solar cell

ZnO based heterojunctions is also used in solar cell applications. ZnO 1D nanostructure are used in inorganic [19], organic hybrid [41], polymer [42,43], and DSSC solar cell applications. Cu_2O forms heterojunction structure with ZnO nanorods and shows solar cell activity [19]. Use of quantum dots like CdSe in ZnO based solar cells showed promising performance [44]. ZnO nanorods with PEDOT forms an organic hybrid solar cell with increased open circuit voltage of 0.9V [45]. The piezo electric proper-

ty of ZnO has also been investigated in ZnO and P3HT based hybrid solar cell, which shows an increase in open circuit voltage of hundreds of millivolts for tensile or compressive stress levels [41]. ZnO nanorods decorated with Au nanoparticles reported to form a Schottky solar cell [46]. Though heterojunction devices of ZnO are reported to contribute to solar cell activity, majority of ZnO based solar cell studies were concentrated on dye sensitized solar cell (DSSC) applications. Main draw backs of DSSCs include dye agglomeration, dye leakage, low stability etc. Latest development on DSSC is the 3D structured solar cell fabrication [47]. Detailed review of ZnO 1D nanostructure based DSSCs are given in chapter 7.

1.2.6 Photo catalysis.

ZnO nanorod/CuO heterojunction showed photocatalytic activity. The nanorods were grown over steel wire mesh. The device structure shows flexibility and many practical advantages. The device reduced the dye content in a solution to about 10% after an 8 hr treatment [48].

1.2.7 Field effect devices

ZnO nanorod based field effect devices were demonstrated with bottom gate and top gate configurations [49–52]. To fabricate the devices nanorods are distributed over suitable substrates using self-assembly or spin coating. In the next step e-beam lithography

is used to make metallic contacts with the nanorods to form the device structure. The development of 14 nm processor technology utilizing revolutionary 3D transistor design by Intel opens new possibility for 1D nanostructure based transistors.

1.2.8 Antireflection coating

Aligned growth of ZnO nanorods possess antireflection properties. Such structures are used over a metal-insulator-silicon (MIS) photodetector to increase the photodetection capabilities 15 times [53].

1.2.9 pH sensor

ZnO is an amphoteric oxide, which can react to both acids and bases. This property is utilized in pH sensing applications. ZnO react with the environment and its surface potential is changed accordingly. The pH of a solution is the ability of that solution to protonate or deprotonate. Surface of ZnO nanostructures are highly sensitive to H^+, because surface bonding sites easily hydrogenate as ZnO surface makes contact with a solution. Hence because of the property of the solution the protonation or deprotonation occur at the surface of ZnO, which changes its surface potential. If surface potential is monitored, the pH of the solution can be measured effectively. ZnO nanostructures showed ability to detect pH from 1 to 16 [54,55]. Fulati et al. reported the ability of these devices to produce reproducible results even after

several days of operation [54]. The size of ZnO nanorods helps to determine even the intracellular pH variations [55]. Compared to nanorods nanotubes posses large surface area, which gives an increased pH detection [54].

1.2.10 Nanogenerators

Synthesized crystalline ZnO nanostructures possess piezo electric properties and semiconducting properties. Because of the piezo electric property of ZnO, a stress applied on the nanostructure will result in potential variations across the nanostructures. These potential variations can be effectively converted to a source of electricity. In general this technique uses a mechanical force applied over the ZnO nanostructures, which can be considered as an applied stress. On applied stress a Schottky junction is used to convert the voltage variations into current. Such devices successfully demonstrated few millivolts and few nanoampre current [56–59]. The current produced in this technique is alternating current. A. Yu et al. introduced a layer by layer approach which can be help to stack several generators together [58]. The stacking procedure shows similar stacking features as that of batteries. Thus stacking can be utilized to generate current and voltage values as required for a practical application.

1.2.11 Switching memory devices

Novel resistive switches are fabricated using ZnO nanostructures. Such electromechanical devices demonstrated successful read and write operations using binary stress levels. The creation of polarisation charges on variation in applied external force/stress is used for this principle [60].

1.3 Conclusions

Study of the binary oxide materials, on its one dimensional form is highly relevant. Compared to earlier applications of ZnO in bulk form, recent studies explore its potential in nanotechnology. Various applications being demonstrated with 1D nanostructures of ZnO clearly emphasise its potential to replace some of the existing technologies. Deep knowledge of the nanostructure growth mechanism will be helpful for altering the properties of these nanostructures. Available techniques for the growth of one dimensional nanostructures are application specific and have advantages and disadvantages. Choosing the right technique is vital for obtaining good quality nanostructures.

1.4 References

[1] R.N. Noyce, Semiconductor Circuit Complex Having Isolation Means, United States patent 3150299, (1964).

[2] J.S. Kilby, Miniaturized Slef Contained Circuit Modules and Method of Fabrication, United States patent 3138744, (1964).

[3] J.S. Kilby, Miniaturized Electronic Circuits, United States patent 3138743, (1964).

[4] R.N. Noyce, Semicomductor Device And Lead Structure, United States patent 2981877, (1961).

[5] J.S. Kilby, L.R.E. Dilger, Milwaukee, Component Mounting for Printed Circuits, United States patent 2945163, (1960).

[6] R.N. Noyce, Field Effect Transistor, United States patent 2869055, (1959).

[7] J.S. Kilby, IEEE Trans. Electron Devices 23 (1976) 648.

[8] Z.I. Alferov, V.M. Andreev, D.Z. Garbuzov, Y.V. Zhilyaev, E.P. Morozov, E.L. Portnoi, V.G. Trofim, Sov. Phys.-Semicond. 4 (1971) 1573.

[9] R.D. Clark, K.N. Tapily, S.P. Consiglio, T. Hakamata, D. O'Meara, D. Newman, M. Collings, D. Szymanski, C.S. Wajda, G.J. Leusink, ECS Trans. 72 (2016) 319.

[10] E. Karl, Z. Guo, J.W. Conary, J.L. Miller, Y.G. Ng, S.

Nalam, D. Kim, J. Keane, U. Bhattacharya, K. Zhang, A 0.6V 1.5GHz 84Mb SRAM Design in 14nm FinFET CMOS Technology, IEEE Int. Solid-State Circuits Conf., San Francisco (2015) 308.

[11] A. Rahman, P. Bai, G. Curello, J. Hicks, C.H. Jan, M. Jamil, J. Park, K. Phoa, M.S. Rahman, C. Tsai, B. Woolery, J.Y. Yeh, Reliability studies of a 22nm SoC platform technology featuring 3-D tri-gate, optimized for ultra low power, high performance and high density application, IEEE Int. Reliab. Phys. Symp. Proc., California (2013) 1.

[12] C.H. Jan, F. Al-Amoody, H.Y. Chang, T. Chang, Y.W. Chen, N. Dias, W. Hafez, D. Ingerly, M. Jang, E. Karl, S.K.Y. Shi, K. Komeyli, H. Kilambi, A. Kumar, K. Byon, C.G. Lee, J. Lee, T. Leo, P.C. Liu, N. Nidhi, R. Olac-Vaw, C. Petersburg, K. Phoa, C. Prasad, C. Quincy, R. Ramaswamy, T. Rana, L. Rockford, A. Subramaniam, C. Tsai, P. Vandervoorn, L. Yang, A. Zainuddin, P. Bai, A 14 nm SoC platform technology featuring 2nd generation Tri-Gate transistors, 70 nm gate pitch, 52 nm metal pitch, and 0.0499 um^2 SRAM cells, optimized for low power, high performance and high density SoC products, IEEE Symp. VLSI Circuits, Dig. Tech. Pap., Kyoto (2015) T12.

[13] D. Look, D. Reynolds, J. Sizelove, R. Jones, C. Litton, G.Cantwe, Solid State Commun. 105 (1998) 399.

[14] T. Damen, S. Porto, B. Tell, Phys. Rev. 142 (1966) 570.

[15] B. Xiang, P. Wang, X. Zhang, S.A. Dayeh, D.P.R. Aplin, C. Soci, D. Yu, D. Wang, Nano Lett. 7 (2006) 323.

[16] G.D. Yuan, W.J. Zhang, J.S. Jie, X. Fan, J.A. Zapien, Y.H. Leung, L.B. Luo, P.F. Wang, C.S. Lee, S.T. Lee, Nano Lett. 8 (2008) 2591.

[17] J. Luo, C.C. Ling, B. Yuk, F. Hsu, Y.Y. Xi, K.H. Tam, A.B. Djuris, C.K. Cheung, A. Man, C. Ng, W.K. Chan, X. Deng, C.D. Beling, S. Fung, K.W. Cheah, P. Wai, K. Fong, C.C. Surya, Adv. Funct. Mater. 18 (2008) 1020.

[18] L.S. Vikas, K.C. Sanal, M.K. Jayaraj, A. Antony, J. Puigdollers, Phys. Status Solidi A 211 (2014) 2493.

[19] H. Wei, H. Gong, Y. Wang, X. Hu, L. Chen, H. Xu, P. Liu, B. Cao, CrystEngComm 13 (2011) 6065.

[20] J.K. Wu, W.J. Chen, Y.H. Chang, Y.F. Chen, D.R. Hang, C. Liang, J.Y. Lu, Nanoscale Res. Lett. 8 (2013) 387.

[21] Q. Yang, W. Wang, S. Xu, Z.L. Wang, Nano Lett. 11 (2011) 4012.

[22] J.H. Wu, S.Y. Liu, S. Li, Y. long Jiang, G.P. Ru, X.P. Qu, Appl. Phys. A 109 (2012) 489.

[23] J. Bao, M. a Zimmler, F. Capasso, X. Wang, Z.F. Ren, Nano Lett. 6 (2006) 1719.

[24] Y. He, J. Wang, W. Zhang, X. Chen, Z. Huang, Q. Gu, J. Phys. Conf. Ser. 152 (2009) 012054.

[25] J.Y. Wang, C.Y. Lee, Y.T. Chen, C.T. Chen, Y.L. Chen, C.F. Lin, Y.F. Chen, Appl. Phys. Lett. 95 (2009) 131117.

[26] Y.Y. Xi, Y.F. Hsu, A.B. Djurišić, A.M.C. Ng, W.K. Chan, H.L. Tam, K.W. Cheah, Appl. Phys. Lett. 92 (2008) 113505.

[27] R. Könenkamp, R.C. Word, M. Godinez, Nano Lett. 5 (2005) 2005.

[28] M. Willander, O. Nur, J.R. Sadaf, M.I. Qadir, S. Zaman, A. Zainelabdin, N. Bano, I. Hussain, Materials (Basel). 3 (2010) 2643.

[29] H. Guo, Z. Lin, Z. Feng, L. Lin, J. Zhou, J. Phys. Chem. C 113 (2009) 12546.

[30] Y. Toyoshima, M. Miyayama, H. Yanagida, K. Koumoto, Jpn. J. Appl. Phys. 22 (1983) 1933.

[31] Y. Ushio, M. Miyayama, H. Yanagida, Sensors Actuators B 12 (1993) 135.

[32] Y. Nakamura, H. Yoshioka, M. Miyayama, H. Yanagida, J. Electrochem. Soc. 137 (1990) 940.

[33] S. Mridha, D. Basak, Semicond. Sci. Technol. 21 (2006) 928.

[34] Y. Hu, X. Zhou, Q. Han, Q. Cao, Y. Huang, Mater. Sci.

Eng. B 99 (2003) 2002.

[35] J.Y. Park, S.-W. Choi, S.S. Kim, Nanoscale Res. Lett. 5 (2009) 353.

[36] T.S. Van Den Heever, G.L. Hardie, W.J. Perold, Int. J. Nano Stud. Technol. 2(1) (2013) 12.

[37] S.W. Fan, A.K. Srivastava, V.P. Dravid, Appl. Phys. Lett. 95 (2009) 142106.

[38] B.S. Kang, H.-T. Wang, L.-C. Tien, F. Ren, B.P. Gila, D.P. Norton, C.R. Abernathy, J. Lin, S.J. Pearton, Sensors 6 (2006) 643.

[39] C. Lao, Y. Li, C.P. Wong, Z.L. Wang, Nano Lett. 7 (2007) 1323.

[40] E.R. Waclawik, J. Chang, A. Ponzoni, I. Concina, D. Zappa, E. Comini, N. Motta, G. Faglia, G. Sberveglieri, Beilstein J. Nanotechnol. 3 (2012) 368.

[41] Y. Yang, W. Guo, Y. Zhang, Y. Ding, X. Wang, Z.L. Wang, Nano Lett. 11 (2011) 4812.

[42] J.Y. Chen, F.C. Hsu, Y.M. Sung, Y.F. Chen, J. Mater. Chem. 22 (2012) 15726.

[43] W.J.E. Beek, M.M. Wienk, M. Kemerink, X. Yang, R. a J. Janssen, J. Phys. Chem. B 109 (2005) 9505.

[44] Q. Peng, Y. Qin, Nanowires - Implementations Appl.

InTech, Rijeka (2011) 157.

[45] J. Podzemský, W. Schade, Organic solar cells based on ZnO nanowires layer, EEIC, Germany (2006) 1.

[46] Z.H. Chen, Y.B. Tang, C.P. Liu, Y.H. Leung, G.D. Yuan, L.M. Chen, Y.Q. Wang, I. Bello, J.A. Zapien, W.J. Zhang, C.S. Lee, S.T. Lee, J. Phys. Chem. C 113 (2009) 13433.

[47] G. Mariani, Y. Wang, P.S. Wong, A. Lech, C.H. Hung, J. Shapiro, S. Prikhodko, M. El Kady, R.B. Kaner, D.L. Huffaker, Nano Lett. 12 (2012) 3581.

[48] S. Jung, K. Yong, Chem. Commun. 47 (2011) 2643.

[49] H.J. Kim, C.H. Lee, D.W. Kim, G.C. Yi, Nanotechnology 17 (2006) S327.

[50] J.K. Tsai, T.C. Wu, J.H. Shih, T.H. Meen, Y.S. Liu, Y.C. Jheng, Manufacture and characterization of the single ZnO nanorod field effect transistor, 4th IEEE Int. Nanoelectron. Conf., IEEE, Singapore (2011), 1.

[51] W. Il Park, J.S. Kim, G.C. Yi, M.H. Bae, H.J. Lee, Appl. Phys. Lett. 85 (2004) 5052.

[52] B. Sun, H. Sirringhaus, J. Am. Chem. Soc. 128 (2006) 16231.

[53] H. Kim, J. Bae, Phys. Status Solidi 210 (2013) 2510.

[54] A. Fulati, S.M.U. Ali, M. Riaz, G. Amin, O. Nur, M.

Willander, Sensors 9 (2009) 8911.

[55] S.M. Al-Hilli, R.T. Al-Mofarji, M. Willander, Appl. Phys. Lett. 89 (2006) 173119 1.

[56] X. Wang, J. Song, J. Liu, Z.L. Wang, Science 316 (2007) 102.

[57] R. Yang, Y. Qin, C. Li, L. Dai, Z.L. Wang, Appl. Phys. Lett. 94 (2009) 022905.

[58] A. Yu, H. Li, H. Tang, T. Liu, P. Jiang, Z.L. Wang, Phys. Status Solidi - Rapid Res. Lett. 5 (2011) 162.

[59] C.Y. Chen, J.H. Huang, J. Song, Y. Zhou, L. Lin, P.C. Huang, Y. Zhang, C.P. Liu, J.H. He, Z.L. Wang, ACS Nano 5 (2011) 6707.

[60] W. Wu, Z.L. Wang, Nano Lett. 11 (2011) 2779.

Chapter 2

Growth and characterization techniques

2.1 Growth techniques

The scientific world saw extensive growth towards the end of 20th century in research and development for the production of ZnO nanostructures. ZnO is a widely studied material and the techniques for synthesizing various nanostructures have been perfected over the years. Recent studies showed that a uniform growth of ZnO nanostructures in one dimensional form (1D) is essential for optoelectronic device applications. Various vacuum assisted techniques used for it includes chemical vapor deposition (CVD) [1–7], molecular beam epitaxy (MBE)[8,9], vapor liquid solid technique (VLS)[10], pulsed laser deposition[11,12] etc.

Vacuum assisted techniques are sophisticated and expensive compared to much simple solution based techniques. Though earlier reports showed better crystallinity for nanostructures prepared using vacuum assisted techniques, such as chemical vapor deposi-

tion (CVD)[1–7], molecular beam epitaxy (MBE)[8,9], vapor liquid solid technique (VLS)[10], pulsed laser deposition[11,12] etc. recent reports on solution processed ZnO nanostructures show better crystallinity. Flexibility on control of quality of nanostructures makes solution based processes more attractive.

2.1.1 Solution Process

Solution processing is a widely used technique for preparation of ZnO nanostructures. Solution process has several advantages including inexpensive, faster growth rates, doesn't require any special environment[2]. During growth of ZnO in most of the cases a basic solution containing zinc salt hydrolyses to form an unstable zinc complex like zinc hydroxide. Under suitable experimental conditions, these complexes recrystallizes via dehydration to form ZnO. During growth of wurtzite ZnO the terminating atom in [0 0 0 1] direction will be Zn^{2+} or O^{2-}. Due to the high energy of polar surfaces, new atoms are easily attached to the polar axis. In one cycle Zn^{2+} ion attaches and in the next cycle O^{2-} attaches and this cycle continues and crystalline ZnO is formed[13]. The faster growth rate in [0 0 0 1] direction is utilized in the growth of 1D nanorods.

For the growth of ZnO, various zinc containing salts such as $Zn(NO_3)_2$[14–16], $Zn(COOH)_2$[17], Zinc sulfate[14,18] etc. are dissolved in suitable solvents and allowed to react with materials like

NaOH[14], NH_4OH[18], DMSO, HMT[15,16,19] etc. Under suitable pH, spontaneous nucleation occur which in turns acts as seed for further growth of ZnO nanostructure. The growth of ZnO nanorods can be activated by depositing a suitable seed over a substrate. This idea is USED in chemical bath deposition process, where the substrate is immersed inside a suitable precursor solution under desired experimental conditions, various nanostructures can be grown over the substrate. Zinc oxide nanorods were already grown successfully by this technique[17,18,20].

Spin coating is another solution based technique, through which a suitable solution with required consistency is prepared. A small volume of this solution is deposited over a substrate and the substrate is made to spun. Due to the centrifugal force built up by the rotating head, the thickness and uniformity of the deposit can be varied. Suitable baking of the sample promises the formation of ZnO layer. This technique is generally used for depositing ZnO seed layer over any substrate which acts as substrate for further growth of ZnO nanostructures, especially nanorods by other suitable techniques[20].

i) Electrodeposition

Electrodeposition is a process in which a material is deposited over suitable substrate by applying an electric filed. Electrodeposition process in general is performed in a three electrode electrochemical cell. The cell contains a suitable electrode on which the electrodeposition occurs, which is called working electrolyte. A suitable positive potential is applied on the working electrode with respect to a reference electrode, which is used to maintain a constant electrode potential irrespective of solution disturbances. A counter electrode, usually a noble metal like Au, Pt etc., will collect the current in the process. These three electrodes will be immersed in a suitable electrolyte during electrodeposition process. A potentiostat/galvanostat is used to connect the three electrodes in an electrochemical cell. The electrodeposition process is schematically represented in figure 2.1.

To deposit 1D nanostructures of ZnO a negative potential is applied at the substrate with respect to a reference electrode, and the whole setup is immersed inside a Zn ion containing electrolyte.

$$Zn^{2+} + 4OH^{-} \rightarrow Zn(OH)_4^{2-} \quad \text{--(2.1)}$$

$$Zn(OH)_4^{2-} \rightarrow ZnO + 2H_2O \quad \text{--(2.2)}$$

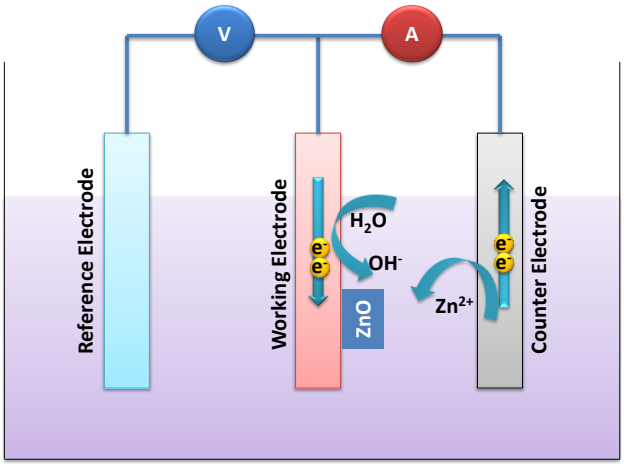

Figure 2.1: Schematic diagram of electrodeposition of ZnO.

Electrodeposition can be performed only on conducting substrate, which acts as the cathode. Usually the deposition is performed in a three terminal electrochemical cell, where the conducting substrate is used as working electrode. A suitable reference electrode and a metallic counter electrode (like Pt, Au etc.) along with working electrode completes the cell structure. If the deposition conditions are tuned, growth of one dimensional nanostructures of ZnO can be achieved over the working electrode. One of the advantages of electrodeposition is that, even if the substrate has different shapes like flat, curved, flexible etc., ZnO nanostructures can be deposited over the entire conductive substrate. In this technique electric potential is driving the growth process. Hence uniform deposition of ZnO nanorods over a large area can be ob-

tained. Therefore, electrodeposition is a promising technique for wafer scale production of nanorods over a substrate.

Changing the experimental conditions can modify the growth rate along various crystal directions, which can result in the formation of nanostructures with different shapes. Growth of different shapes of nanostructures like hexagonal rods, woven nanoneedles, rhombohedral rods etc, from Zinc nitrate based precursor solution with the help of different salts like KCl, NH_4F, etc. [21] has been achieved. Biologic SP300 potentiostat/galvanostat is used, to power the electrochemical cell, in the present study. The details of growth of 1D ZnO structures by electrodeposition are discussed in Chapter 3.

ii) Hydrothermal synthesis

Hydrothermal synthesis is also a solution growth process. In this process, the growth is performed in an elevated temperature and pressure conditions in special containers called autoclaves. The inner side of the autoclave is made of non-reactive materials like Teflon, platinum etc. Suitable precursor solution is prepared and is filled inside an airtight autoclave. On increasing the reaction temperature, the pressure inside autoclave increases of the order of mega Pascal. Autoclaves can withstand enormous amount of pressure generated from within the container.

Bulk form of ZnO crystal s synthesized via hydrothermal technique in 1950 itself by Laudise and Ballman[22]. Synthesis of ZnO rod was first reported in 1990 by Andre et al. from hydrolysis of zinc chloride in the presence of hexa methylene tetra amine (HMT)[23]. Roughly ten years later, Vayssieres et al. reported the formation of ZnO rods over a substrate by hydrothermal synthesis using zinc nitrate and HMT[24]. Later, various combination of precursors like $Zn(NO_3)_2$ & HMT[1,25–27], zinc acetate & ammonium hydroxide[28–30], zinc sulfate & ammonia[31] etc. were used to make ZnO nanorods by hydrothermal technique. Use of zinc acetylacetonate will act as a single source precursor for ZnO nanorod synthesis[32].

According to Aneesh et al. use of NH_4OH with zinc acetate can form ZnO nanorods whereas use of NaOH with zinc acetate can form ZnO nanoparticles[28,33,34]. Hydrothermal synthesis of ZnO uses precursor solution with pH ranging from 7 to 12. A pH of 9 is preferred for Zinc acetate & Ammonium hydroxide based growth of ZnO nanorods. Use of surfactants such as PVA, PEG, sodium dodecyl sulphate, CTAB[35], carbamide, potassium iodide, hydrazine hydrate, etc. can control the morphology of ZnO nanostructures. Similarly anodised alumina, PEO-PPO-PEO amphiphilic block copolymers etc. are generally used as templates for ZnO nanorod growth.

Highly crystalline ZnO nanorods are reported by this technique, even epitaxial growth of nanorods can be achieved by using suitable synthesis conditions[27,36]. Aligned growth of nanorods and even wafer scale production of ZnO nanorods are reported by this technique[37]. Advantages of hydrothermal synthesis includes its simplicity, easiness, low cost, control on nanostructure formation, large yield etc.

2.2 Characterization techniques

The synthesized materials and fabricated devices are characterized using several techniques. Various tools used for the characterization of samples are described below.

2.2.1 Morphological studies

i) Scanning Electron Microscope

Scanning electron microscope can measure the surface morphology of sample. A conventional optical microscope can have resolution upto diffraction limit. One method to improve the imaging resolution beyond diffraction limit is by using electron microscope. In scanning electron microscope electron beam is scanned over sample surface and signal coming out after the interaction of electron with sample surface is taken out and plotted to obtain a 2D SEM image. SEM can give projection of the surface variation onto a plane.

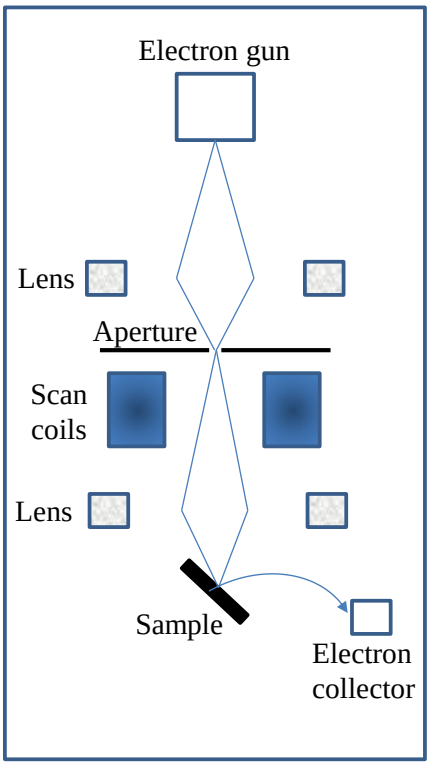

Figure 2.2: Schematic diagram of SEM.

Electron beam in SEM is generated by thermionic emission from an electron gun. Tungsten filament is generally used as thermionic emission source. In latest addition of SEM called field emission scanning electron microscope (FESEM), filed emission gun is used to obtain a fine electron beam. The electron beam is then allowed to pass through several electromagnetic lenses to focus the electron beam. An aperture is used to fine tune the diameter of the electron beam. When electrons interact with sample, electrons may

be elastically scattered/reflected (back scattered electrons), secondary electrons by inelastic scattering may be produced, or even electromagnetic radiation may be generated. Each of these signals captured by special detectors can give different types of SEM images and information. To obtain image of the sample surface the electron beam is scanned over the sample surface using scanning coils. FESEM images of samples under investigation were measured using Carl Zeiss Ultra 55 and Raith 150 field emission scanning electron microscopes.

ii) Atomic Force Microscope

The invention of scanning tunneling microscope (STM) in 1981 by Gerd Binning and Heinrich Rohrer helped to visualize and characterize smaller sized samples, which led to the development of the field called scanning probe microscopy. Atomic force microscopy is one such technique where atomic force is used as the probe.

AFM utilizes a tip attached to a cantilever for probing. When the tip is brought into the proximity of the sample surface (in nm range), the tip experiences a repulsive atomic force. Due to this force, the cantilever is slightly deflected. If the cantilever is moved across the surface the extent of deflection will change from position to position according to the surface features of the sample. Surface roughness can be extracted by mathematical calculations from the cantilever deflection data.

A typical structure of AFM is shown in figure 2.3. The heart of the device is the cantilever along with an atomically sharp tip, which is usually made of Si or SiN. Mechanical movement of the tip is achieved by a XYZ piezo. A laser light is reflected from the back side of the cantilever and is allowed to incident over a quadrant photo diode. The quadrant photo diode tracks the position of laser spot. On decreasing the gap between cantilever and sample, the cantilever deflects, this deflection can now be tracked as a variation of laser spot in the quadrant photo diode. To get the information over an entire surface, a raster scan approach is used. The scanned data is then plotted in 2D or 3D images, where the Z axis is usually plotted in colour scale.

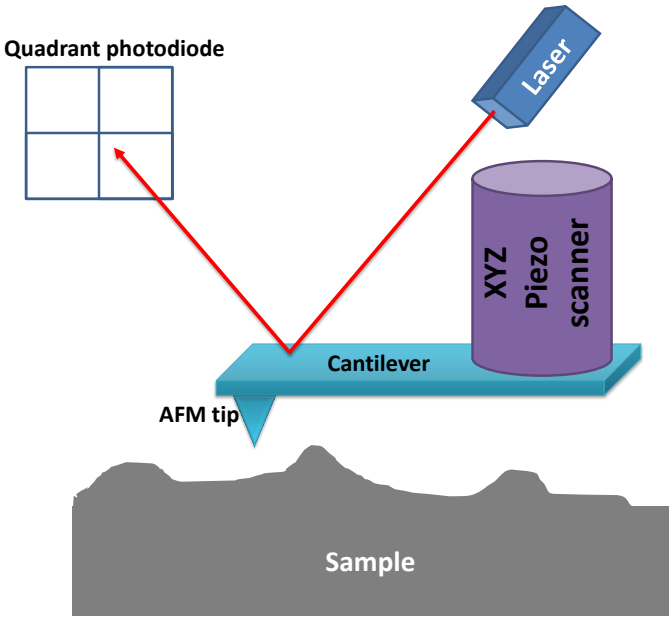

Figure 2.3: Schematic diagram of AFM.

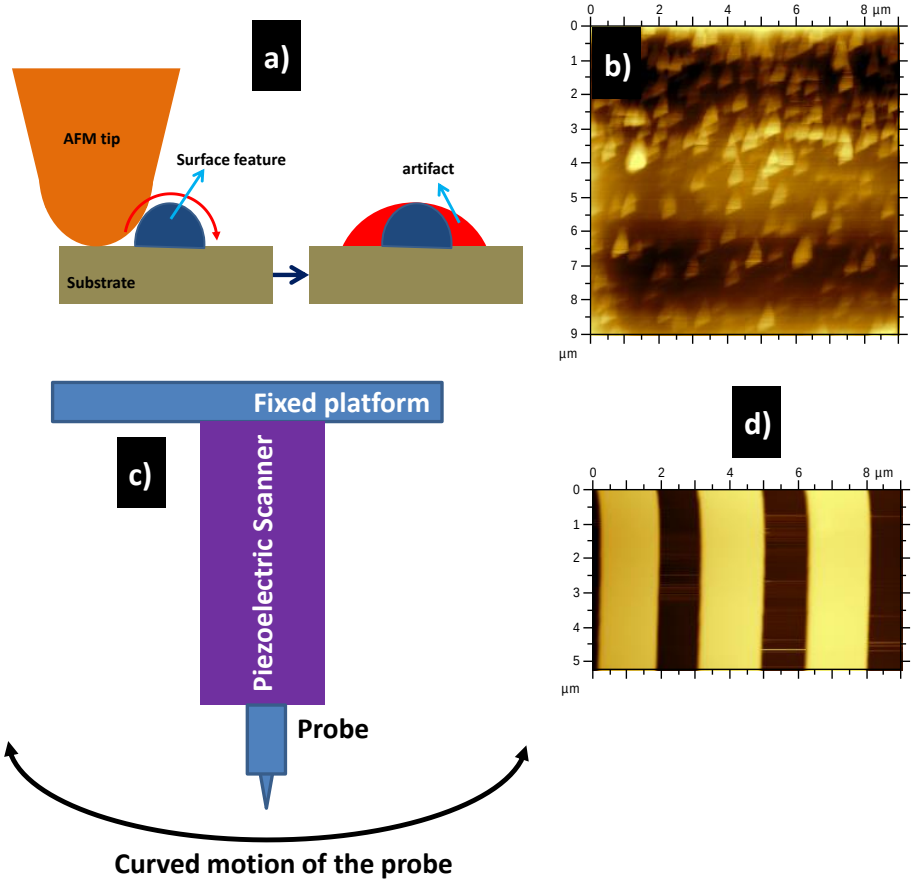

Figure 2.4: Various AFM image artifacts. (a) Schematic representation of artifact due to large size of the tip. (b) AFM image observed, when a broken probe is used for scanning. (c) Schematic representation of curved motion of the probe. (d) AFM image of scanner creep.

AFM is a surface analysis tool, which doesn't require any sample preparation process. It is a non-destructive technique. The actual surface variations in Z axis can be monitored. AFM can replicate a 3 dimensional reconstruction of surface morphology of the sample. It is very difficult to get the 3D information of a sample surface using other techniques. Measurement of nanostructures, cracks, or even thickness of thin layers can be found using this technique.

The probe sample interaction detected by the instrument is being mapped to reconstruct an AFM image of sample surface. Any error in this process can lead to image artifacts. Acquiring correct AFM data is therefore a necessity for obtaining an accurate topography of the sample surface. Four sources of major AFM image artifacts are a) probes, b) scanners, c) image processing and d) vibrations.

AFM probes are fabricated using Si or SiC material via anisotropic wet etching. Typical AFM probe have few atoms in its tip. When imaging is performed using this probe sample feature larger than the tip diameter can only be recorded. As a general convention, to measure a sample feature accurately, the probe tip should be at least 1/10 of the feature size. If the probe tip is larger than the surface feature, instead of imaging the sample features, probe tip will be imaged and cause image artifact, as shown in figure 2.4 (a). The typical shape of the AFM probe also limits the

measurements of narrow well structure, which has a diameter, of the order or shorter than the probe diameter. Due to wear and tear the tip may become blunt or broken. Due to the typical shape of probe formed by anisotropic etching, the broken tip edge will look like a triangle. Hence, images scanned by broken AFM probe will give repeated triangular structure, as shown in figure 2.4 (b). Any observation of double image or repeated image of triangular tip can be considered as probe artifacts. Replacing the tip may be the only option to correct this artifact.

Usual AFM scanners are made of piezoelectric material. Sweeping the applied potential across the piezoelectric material allows the probe to be scanned over the surface. Since one end of the piezoelectric material is fixed, the scan can cause bow and tilt in the AFM image, as shown in figure 2.4 (c). Latest AFM data analysis software can eliminate this artifact during post production state. Scanner creep is yet another artifact associated with the scanner. This type of artifact is generally observed when sudden change in scan area is performed. The first few lines show some offset, which result in the formation of a bended shape as shown in figure 2.4 (d). This is produced due to the hysteresis of the piezoelectric material. This artifact will be cleared after scanning few lines. Providing bad gain values to piezoelectric scanner can also damage the quality of AFM data. If low gain values are given, the scanner cannot account for the surface variations. While, high gain

can result in unwanted oscillations and noise. Proper gain value along with optimized scan speed is necessary for obtaining proper visualization of sample features.

Proper image processing after measurement gives AFM image as close to the original sample surface. Image processing can eliminate bow and tilt. Image processing can reduce noise in the image. But, too much filtering can remove actual feature data.

AFM records sample feature of the order of few nanometers in size. Hence, even small vibration between sample surface and AFM probe can damage the image quality. Even the tip can get damaged, if the vibrations are not being controlled properly. Even loud noise can create artifacts. To cancel external vibrations, AFM instrument is usually arranged in vibration free tables. Acoustic dampers and faraday cages are additional features which can improve the quality of AFM data further. Surface morphology of samples in the present study were measured using Agilent 5500 atomic force microscope

2.2.2 Structural characterization

i) X-ray diffraction studies

X-ray light has a wavelength which is close to the interatomic spacing in a lattice. Hence interaction of X-ray with material can give information on arrangement of atoms or molecules inside a material. Structure analysis using X-ray utilizes its elastic scat-

tering. Upon scattering the X-ray light destructively interfere in most cases and gives maximum intensity via constructive interference only at particular position. The angular positions at which the intensity maxima occurs is explained by the Bragg's law.

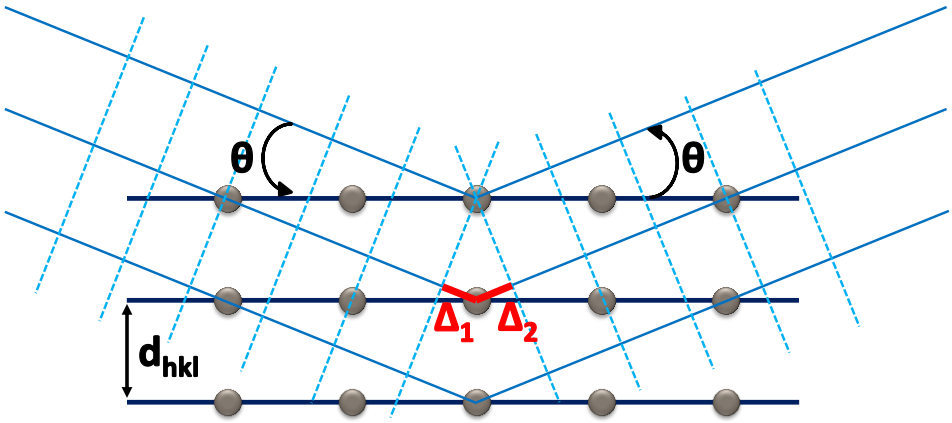

Figure 2.5: Schematic representation of Bragg's law.

From the schematic representation of lattice points with an inter planar spacing of 'd' (figure 2.5), it is clear that for constructive interference to occur, the condition is

$$\Delta_1 + \Delta_1 = 2d\ cos(90^o - \theta) = 2d\ sin\theta \qquad \text{--(2.3)}$$

This condition is the popular form of Bragg's law. If a scan is performed in θ, intensity maxima may be obtained for those θ values which match with the corresponding d_{hkl} values. From the corresponding d_{hkl} values the crystal structure can be studied in

detail. The table 2.1. summaries the relations between the inter-planar spacing and its corresponding miller indices (h k l).

Table 2.1: The dependence of d_{hkl} on miller indices hkl for different crystal structures.

Crystal system	Constrains	$\frac{1}{d_{hkl}^2} =$
Cubic	$a=b=c$ $\alpha=\beta=\gamma=90^0$	$\frac{h^2+k^2+l^2}{a^2}$
Tetragonal	$a=b$ $\alpha=\beta=\gamma=90^0$	$\frac{h^2+k^2}{a^2}+\frac{l^2}{c^2}$
Orthorhombic	$\alpha=\beta=\gamma=90^0$	$\frac{h^2}{a^2}+\frac{k^2}{b^2}+\frac{l^2}{c^2}$
Hexagonal	$a=b$ $\alpha=\beta=90^0$ $\gamma=120^0$	$\frac{4}{3}\frac{h^2+hk+k^2}{a^2}+\frac{l^2}{c^2}$
Trigonal/ Rhombohedral	$a=b=c$ $\alpha=\beta=\gamma$	$\frac{(h^2+k^2+l^2)\sin^2\alpha+2(hk+hl+kl)(\cos^2\alpha-\cos\alpha)}{a^2(1-3\cos^2\alpha+2\cos^3\alpha)}$
Monoclinic	$\alpha=\gamma=90^0$	$\frac{h^2}{a^2\sin^2\beta}+\frac{k^2}{b^2}+\frac{l^2}{c^2\sin^2\beta}-\frac{2hl\cos\beta}{ac\sin^2\beta}$

In general, the powder X-ray diffractions measurements are performed in a Bragg-Brentano geometry (focusing-defocusing) configuration. But for high resolution studies a parallel beam configuration is utilized. The generated X-ray contains K_α and K_β ra-

diations. The K beta radiation can be filtered using a Ni filter. For normal powder X-ray diffraction studies, the K_β stripped X-ray light is used as probe. For powder X-ray diffraction studies, the divergence in the incident beam is corrected using suitable slit arrangement. In the diffracted beam side also using a collimator the diffracted light is allowed to fall over the detector.

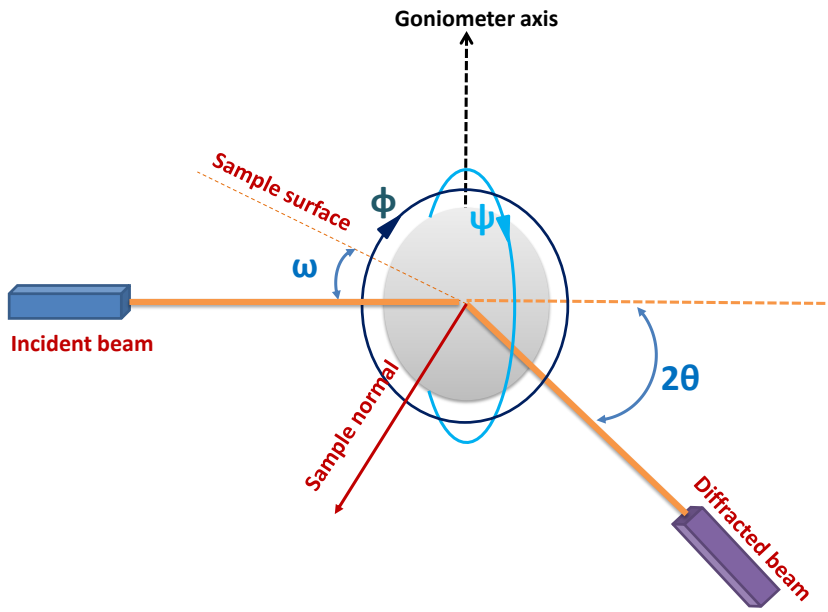

Figure 2.6: The schematic representation of X-ray diffraction goniometer and various axes.

In high resolution studies $K_{\alpha 1}$ wavelength with low divergence is used with the help of suitable optics along with a goniom-

eter having an angular resolution of <0.001°. To select monochromatic X-ray Göbel mirror monochromator or single crystal based monochromator is used. Different slits and masks are used to control the illumination area. Different types of electronic X-ray detectors include scintillation counters, semiconductor detectors, gas detectors etc. Detectors are again classified into point detector, line detector and area detectors. The latest addition of area detectors(2D detector) can improve the speed and accuracy of measurements. Panalytical X'Pert PRO high resolution X-ray diffractometer is used in the present study.

Various studies which can be performed using X-ray diffraction techniques are as follows.

a) Phase analysis

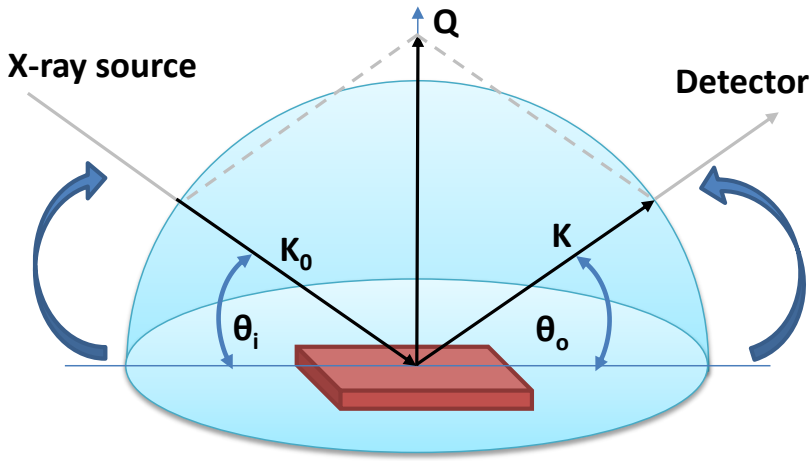

Figure 2.7: Schematic diagram of working of phase analysis.

Phase analysis (θ-2θ) scan are generally used for studying the randomly oriented polycrystalline samples. Compared to high resolution X-ray diffraction techniques one major difference of phase analysis is that the scattered intensity for constant scattering angle is distributed on a circle rather than spots as in high resolution studies. Figure 2.7 represents the schematic diagram of phase analysis measurement.

In this study, the X-ray source is kept at an incident angle θ_i with sample surface, and the detector is kept at θ_o with sample surface. In normal measurements $\theta_i = \theta_o$. Intensity values are measured for each incident/scattered angle to get the whole spectrum of d_{hkl} contributions. From the schematic diagram it is clear that the Q axis is normal to the surface of the sample. Hence θ-2θ scan is essentially a scan over Q axis looking for different d_{hkl} values.

Geometrical constraint in this measurement allows only those lattice planes which are parallel to the surface contribute to the Bragg reflections. For a polycrystalline sample this may not be a problem as similar intensity is expected in all directions. But for preferred oriented samples, especially for thin film samples, contributions from some crystal planes may be absent, which requires high resolution studies to reveal them. Phase analysis usually utilizes Bragg-Brentano geometry of X-ray diffractometer, which is a focusing-defocusing arrangement of X-ray.

GIXRD

A major problem associated with phase analysis, especially for thin film analysis is that for higher scattering angles, the intensity values become weak. For higher scattering angles, when studying thin film samples using phase analysis, the region where X-ray interacts with sample is roughly double the thickness of the thin film. Because of this only few lattice sites contribute to Bragg reflections, which in turn weaken the intensity contribution. One way to solve this problem is by using Gracing Incidence X-ray Diffraction studies, which is usually represented as GIXRD or GAXRD. The idea in this measurement is to keep the incident angle(θ_i) very low. Scan is performed in θ_o axis. In this case the X-ray grace through the surface of the sample and hence more number of lattice sites can interact with X-ray beam.

Preferred orientation

If more number of a particular (h k l) plane interacts with X-ray beam, resulting in increased intensity for that X-ray reflection, we can say that the sample has got preferred orientation. Preferred orientation (texture) is observed for non-random oriented samples. Thin film samples or pressed powder samples can possess texture. Usual texture studies involves high resolution X-ray diffraction measurements. Still θ-2θ scan can also give a qualitative idea on the preferred orientation of the sample. Texture is ana-

lyzed from θ-2θ scan via texture coefficient calculations. The texture coefficient can be calculated from the formula,

$$T_{hkl} = \frac{I_{hkl}/I^0_{hkl}}{\frac{1}{N}\Sigma\left[I_{hkl}/I^0_{hkl}\right]} \quad \text{--(2.4)}$$

Where, T_{hkl} is the texture coefficient, I_{hkl} is the intensity of particular (h k l) peak observed for the preferred oriented sample, I^0_{hkl} is the intensity of the same crystal plane, observed for a randomly oriented reference sample and N is the total number of crystal planes observed in the diffraction spectra. The T_{hkl} value ranges from 0 to N. If T_{hkl} is near N, it means a preferred oriented sample and low T_{hkl} value means a randomly oriented sample.

b) Pole figure analysis

In a conventional θ-2θ scan only planes parallel to sample surface is analyzed. A technique to consider other crystal orientations also under the study is via pole figure analysis. The angles ϕ and ψ represents azimuth of the sample surface plane and tilt of the sample normal respectively. With the help of a Euler cradle, the Bragg reflection intensity variation in tilt and azimuth angles can be measured. Usual goniometer has a range of $0 \leq \psi \leq \pm 90^{o}$ in tilting angle and $0 \leq \phi \leq 360^{o}$ in azimuth angle. During measurement, the sample is rotated in azimuth angle with a suitable tilt with respect

to the sample normal, and intensity variations are measured in each point. The measured intensity of poles are then projected on to the equatorial plane using stereographic projection technique. Generally, the pole figure is represented for a particular crystallographic plane. If a particular crystallographic plane has random orientation, uniform intensity distribution is observed. If the crystal plane has a preferred orientation, poles (intense spots) are observed, which correspond to the family of planes.

Pole figure gives information on how crystal structure of a film is oriented with respect to the substrate. It is a graphical representation of the orientation of objects in space with respect to the substrate orientation.

c) Reciprocal space map

Reciprocal space map (RSM) is a high resolution measurement, where it performs multiple 2θ-ω scans with different offset values. It is a two axis measurement in which one axis represents the 2θ-ω scan, while the other axis represents the offset values (o). The schematic diagram of reciprocal space map is shown in figure 2.8. To obtain good RSM information, step size should be smaller than the reciprocal lattice feature.

The resultant map is usually represented in 2D plots using reciprocal lattice units or diffraction space units (Q_x and Q_z). The third intensity axis is represented by colour bitmap or contour.

The 2θ-ω scans can be converted to reciprocal space units using the following equations[38].

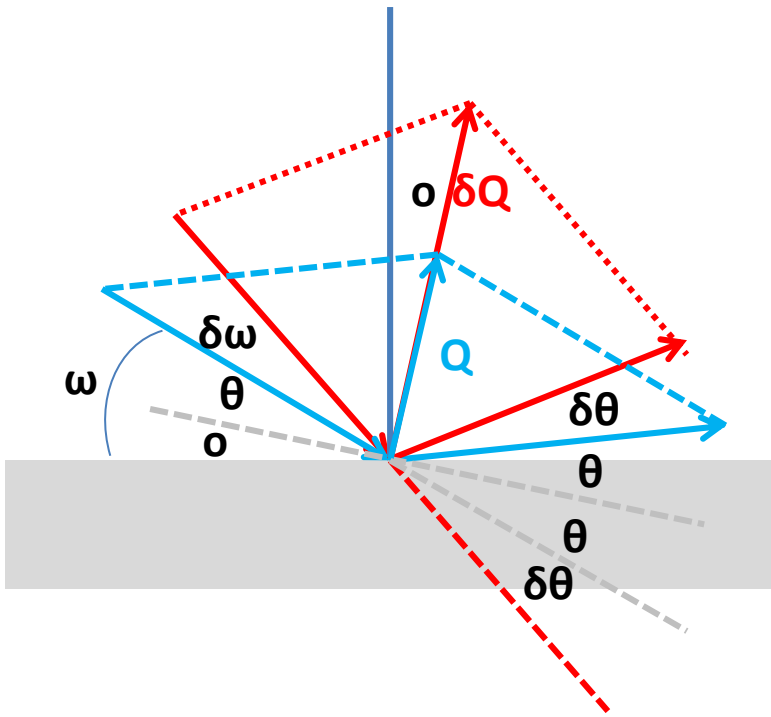

Figure 2.8: Schematic diagram of Q scan with offset.

$$Q_x = \frac{2}{\lambda}\sin\frac{2\theta}{2}\sin\left(\frac{2\theta}{2} - \omega\right) = \frac{1}{\lambda}\{\cos\omega - \cos(2\theta - \omega)\} \qquad \text{--(2.5)}$$

$$Q_z = \frac{2}{\lambda}\sin\frac{2\theta}{2}\cos\left(\frac{2\theta}{2} - \omega\right) = \frac{1}{\lambda}\{\sin\omega - \sin(2\theta - \omega)\} \qquad \text{--(2.6)}$$

Where the Q_z axis usually gives information on d-spacing of the sample, where as the Q_x axis represents the variation in crystalline quality of the film.

d) Rocking curve

Rocking curve analysis of a sample requires high resolution X-ray diffraction optics. After proper alignment of the sample, a θ-2θ measurement is performed at particular peak position. Usually, rocking curve is performed near to a particular crystal reflection peak. Rocking curve performs a scan over relatively smaller region with very small step sizes. Hence the crystal peak under study will get more number of data points. Rocking curve is helpful to obtain actual profile of the diffraction peak, with correct peak maximum position, maximum intensity, FWHM etc. The peak contribution from a single set of parallel planes can be analyzed separately by performing a rocking curve measurement in omega axis while keeping the detector at a fixed 2θ position. This technique is useful for samples having close crystal reflections or even when peaks are overlapping and the peak contributions needs to be distinguished independently.

2.2.3 Optical characterization

i) Raman spectroscopy

The inelastic scattering of light from a material is observed in Raman spectroscopy. The technique helps to identify the vibrational state of the molecule, which helps to identify the chemical and structural information. The inelastically scattered light usually contains lights of wavelength higher or lower than incident light. Scattered light with lower energy is called Stokes radiation and light with higher energy is called anti-Stokes radiation. Stokes lines is usually intense than anti-Stokes lines. In Raman studies the Stokes lines are usually studied. The difference in frequency of excited light and Stokes line is calculated and expressed in terms of wavenumber (cm^{-1}) to obtain Raman spectrum. Thus Raman spectrum gives information on rotational or vibrational levels.

ZnO has hexagonal wurtzite crystal structure. The structure of ZnO belongs to C_{6v}^{4} space group, where each primitive cell contains two formula units[39]. Group theory predicts 8 phonon modes among them one A_1 and one E_1 mode is acoustic modes. Hence the remaining optical modes are

$$\Gamma_{opt} = 1A_1 + 2B_1 + 1E_1 + 2E_2 \quad \text{--(2.7)}$$

Table 2.2: List of theoretically predicted Raman peaks for ZnO.

Symmetry	**Peak position (cm^{-1})**[40–44]
E_2(Low)	101
A_1(TO)	380
E_1(TO)	407
E_2(High)	437
A_1(LO)	574
E_1(LO)	583

The A_1 and E_1 polar modes are both Raman and infrared active. The E_2 non-polar mode is only Raman active. B_1 mode is neither Raman nor infrared active. Due to macroscopic electric fields connected to longitudinal optical phonons, the A_1 and E_1 modes will further split into their longitudinal optical (LO) and transverse optical (TO) modes separately. The TO-LO splitting in ZnO is larger than the A_1-E_1 splitting. Structural characterizations of samples were carried out using Horiba Jobin Yvon Labram HR Micro Raman spectrometer.

ii) Photoluminescence

As the name suggests, photoluminescence uses photons to excite electrons in a material. On excitation, light energy is absorbed by the material, and the energy absorbed causes electrons to be excited to a higher energy state. Electrons can de-excite to ground state by radiative or non-radiative process. In radiative

process, the emitted light should have energy equivalent to the difference in energy of electronic energy levels in the material. Photoluminescence spectrum can reveal various electronic states present in the material. To measure the photoluminescence spectrum, the material is excited with suitable light, and emitted light intensity is monitored, and a plot is made with intensity of emitted light vs wavelength of emission.

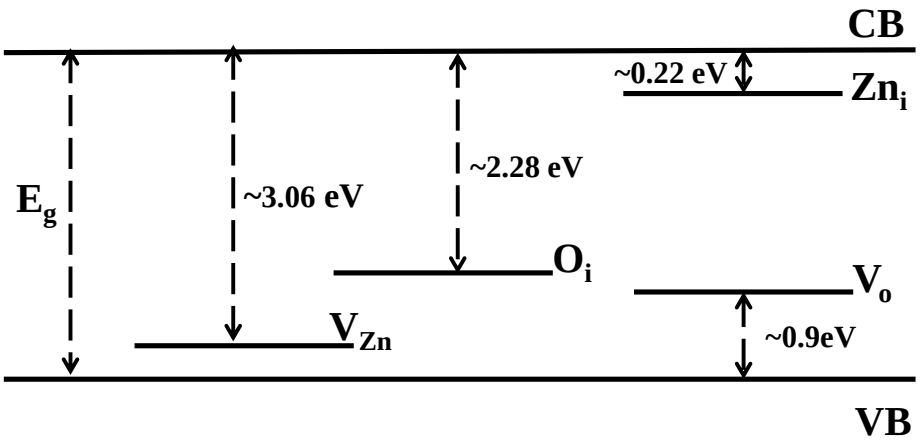

Figure 2.9: The sub band levels in ZnO reported in literature.

In the case of ZnO usually a narrow strong emission in UV region is observed, which corresponds to the transition from conduction band edge to valence band edge, usually denoted as near band edge emission (NBE). Various defects in ZnO material can result in the formation of several sub band gap energy levels. If a

sample has such sub band gaps, according to the nature of those bands, a broad emission can occur. Different defect levels of ZnO, which are already reported include Zn interstitial (Zn_i), Zn vacancy (V_{Zn}), Oxygen vacancy (V_o), Oxygen interstitial (O_i) etc[45–48]. The sub band levels of ZnO from previous reports are shown in figure 2.9.

2.2.4 Electrical characterization

When n-type semiconductor and p-type semiconductor are made into contact a junction is formed at the interface. If both p and n type semiconductors are of same material it is called homojunction and if both semiconductors are of different material, it is called heterojunction. For an n-type semiconductor, the fermi energy level is near the conduction band and for p-type semiconductor it is near valence band. Hence as n-type and p-type semiconductors are made into contact, the band structure bends near the interface so as to flatten the fermi energy level. Depending on band alignment heterojunction can be classified into three types as shown in figure 2.10.

The heterojunction devices fabricated and discussed in this thesis are type II heterojunction devices. Ideally, all heterojunctions are assumed to show a step junction behavior. But, the step junction assumption may not be applicable in most cases, where the junction is considered as a graded junction interface.

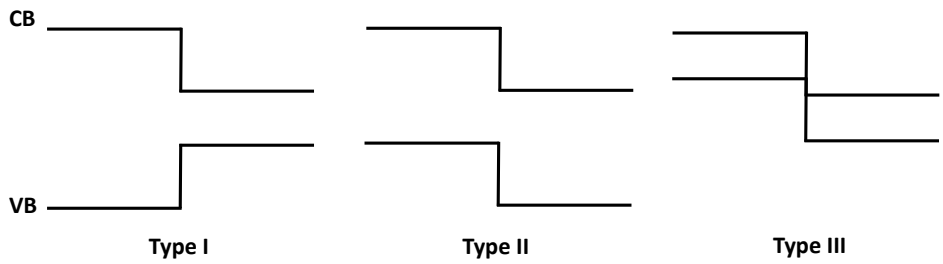

Figure 2.10: Three types of heterojunctions.

On applying suitable bias, the device can conduct current. The junction current and bias voltage are ideally related by the ideal diode equation

$$I = I_0(e^{\frac{V_D}{nV_T}} - 1) \qquad \text{--(2.8)}$$

Where, I_0 is the reverse saturation current, V_D is the bias applied across the device, n is the ideality factor and $V_T = \frac{kT}{q}$ is the thermal voltage. At room temperature, V_T is calculated as 25.85 mV. The V-I characteristics of the heterojunction can be expressed as figure 2.11(a).

For higher forward bias voltages, the ideal diode equation can be approximated as

$$I = I_0 e^{\frac{V_D}{nV_T}} \quad \text{--(2.9)}$$

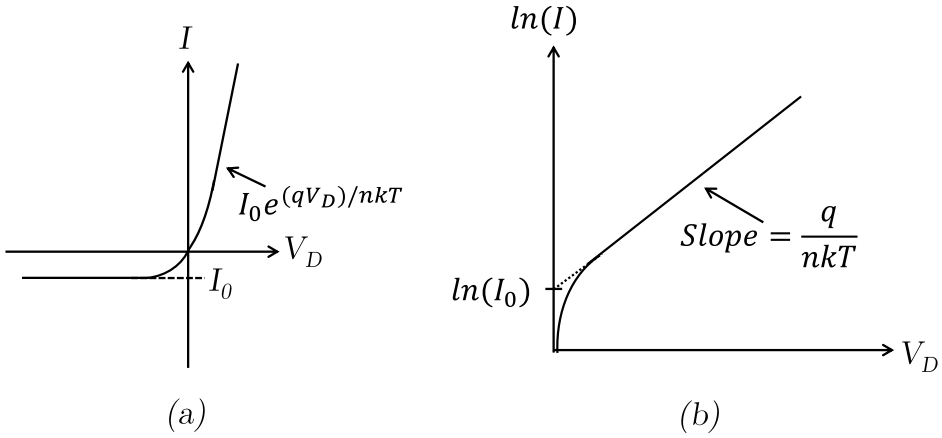

Figure 2.11: Ideal diode (a) V-I characteristics and (b) ln(I) vs V_D plot.

Taking natural logarithm on both sides

$$\ln(I) = \ln(I_0) + \frac{V_D}{nV_T} \quad \text{--(2.10)}$$

Hence, the plot of ln(I) vs V_D will give straight line for bias voltage $V_D > V_k$ (figure 2.11(b)). From the slope (slope = $\frac{q}{nkT}$) of the linear region of the ln(I) vs V_D plot ideality factor 'n' of the heterojunction can be extracted using the equation $n = \frac{1}{slope \times V_T}$. Ideality factor reveals the quality of fabricated heterojunction.

The device interfaces along with the semiconductor itself offers a resistance to the junction current, called series resistance, R_s. Hence, under suitable forward bias, as a junction current I flows through the device, a potential drop IR_s is dropped across R_s due to the series resistance. Moreover, the junction also drops a voltage V_k at the junction. Hence, the applied voltage V can be expressed as

$$V = V_k + IR_s \qquad \text{--(2.11)}$$

Hence, if we plot $\Delta V = V - V_k$ against junction current I, a straight line should be observed (for forward bias higher than V_k). The slope of this straight line plot should give the series resistance of the heterojunction device.

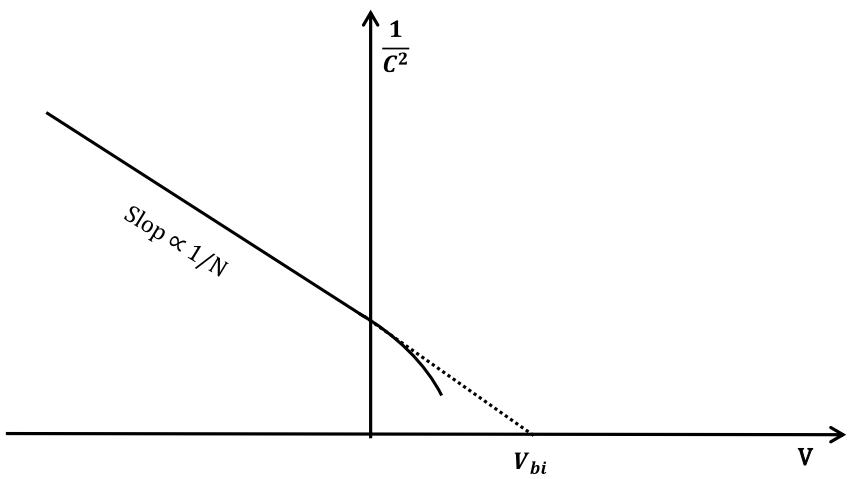

Figure 2.12: The $1/C^2$ vs V graph.

Under reverse bias, the heterojunction device can be considered as a dielectric sandwiched between two electrodes. Hence, under reverse bias it is possible to calculate the heterojunction capacitance. For an ideal abrupt junction device, the junction capacitance can be expressed as[49–51]

$$C_j = \frac{K_s \varepsilon_0 A}{\left[\frac{2K_s\varepsilon_0}{qN_D}(V_{bi}-V)\right]^{1/2}} \quad \text{--(2.12)}$$

or

$$\frac{1}{C_j^2} = \frac{2}{qN_D K_s \varepsilon_0 A^2}(V_{bi} - V) \quad \text{--(2.13)}$$

Which suggests that after measuring the junction capacitance C_j for different reverse bias voltages V, the plot of $\frac{1}{C_j^2}$ vs V will give a straight line, as shown in figure 2.12. By rearranging the equation, the carrier concentration of lightly doped semiconductor region (N_D) can be calculated from the equation

$$N_D = \frac{2}{qK_s\mathcal{E}_0 A^2 \left| \frac{d\left(\frac{1}{C_j^2}\right)}{dV} \right|} \quad \text{--(2.14)}$$

Where $\frac{d\left(\frac{1}{C_j^2}\right)}{dV}$ represents the slope of $\frac{1}{C_j^2}$ vs V plot.

On extrapolating the linear region of the graph, the x intercept will give the knee voltage (V_{bi}) of the heterojunction device.

Photodetector

If junction current changes on illumination with a light source, the heterojunction can be used as a photo detector. A photodetector usually work in two modes, (i) photoconductive, (ii) photovoltaic. In the case of photoconductive detectors, biasing is applied to the junction and change in current to incident light is monitored. On illumination the junction current varies, thus measurement of junction current gives an idea of the quantity of incident light. In the case of photovoltaic detector, zero bias is applied across the junction and variation of junction current with light illumination is monitored. This mode utilizes photovoltaic effect, which is the basis of solar cells. Since zero bias is applied the amount of dark current in this mode will be lesser, while photoconductive mode gives more dark current as biasing leads to junction current (though it is minor). Thus photovoltaic mode of operation gives higher signal to noise ratio compared to photoconductive mode of operation.

A photodetector is analysed by its properties. Some of the commonly used performance parameters are

a) *Dark current:* It is the current passing through the junction in dark condition i.e., in the absence of light. Lower dark

current is usually preferred as increased dark current leads to noise.

b) *Responsivity:* Photoresponsivity (R_λ) is the ratio of generated photocurrent I_D to the incident light power (P). It is usually represented in A/W.

$$R_\lambda = \frac{I_D}{P} \quad \text{--(2.15)}$$

c) *Junction capacitance:* Junction capacitance (C_j) is an important parameter of a photodetector, as it has an impact on the band width and response on the detector. Photodetector under reverse bias operation increases the depletion region, which results in decrease in junction capacitance and improves the response speed.

d) *Junction resistances:* Photodetector offers series resistance and shunt resistance. Series resistance can be measured directly from the V-I characteristics of the junction. Series resistance usually arises from contact resistance, semiconductor resistivity, interface effects etc. Shunt resistance represents the resistance of the photodetector under zero biasing. Though an ideal shunt resistance has ∞ resistance, practical detectors have kΩ to MΩ resistance. Shunt resistance has direct impact on noise of the detector signal. During most operations, high shunt resistance offers little or no effects and thus it can be ignored.

e) *Response time:* Response time is a measure of time which tells how fast the heterojunction device can respond to

light. By giving suitable bias to the device the light source is switched on and off at regular intervals of time and the variation of junction current as a function of time is recorded. From the measured data, the rise and decay parameters can be fitted using the exponential decay equation $J = J_0 + A_1 \exp\left(-\frac{t}{t_1}\right)$, where t_1 represents the decay time constant. If more than one growth or decay mechanism is involved the equation is extended by adding more exponential term like $J = J_0 + A_1 \exp\left(-\frac{t}{t_1}\right) + A_2 \exp(-\frac{t}{t_2})$. Here, t_1 and t_2 represents the two time constants due to the two different growth/decay processes.

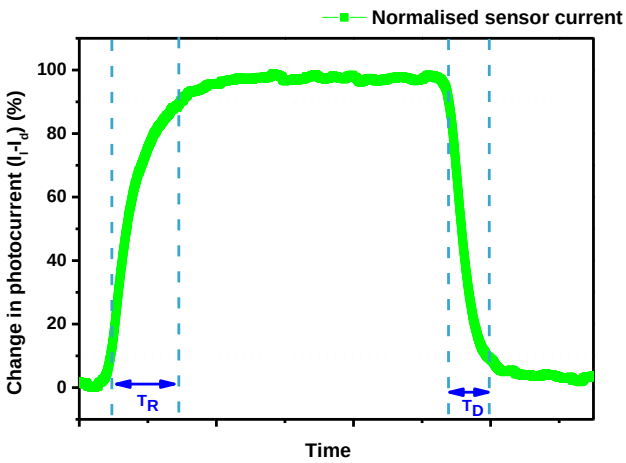

Figure 2.13: Schematic representation of sensor response.

When the device is illuminated with a light pulse, if the sensor shows stable saturation current levels for light on and off conditions, the response time can be calculated as the time difference between 10% and 90% of its maximum response levels as shown in figure 2.13. Here the rise time is taken as the time taken for the device to change the photocurrent from its 10% of maximum value to 90% value [52,53]. Similarly, the decay time is the time taken for the device to change its response from 90% level to 10% level. Usually, this is measured by illuminating the device with an extreme short laser pulse and monitoring its temporal variation of junction current. In our experiment, we monitored the variation of junction current for chopped laser light. The chopped laser light is assumed to be step function like variation. On either side of the step function there is the variation of junction current. On the left side of the step function (light on), where the junction current increases, and the time between 10% and 90% of maximum photocurrent, is taken as rise time. Similarly on the right side of the step function (light off), where junction current decreases, the time between 90% and 10% of maximum photocurrent, is taken as the fall time.

The photo responsivity curve gives the response of the device for different illumination light. Some devices show selective response to particular wavelengths only.

f) *Bandwidth (-3dB):* Band width is the frequency at which output electrical power of the photodetector changes to 50% of its response. Band width of a photodetector tells us the maximum frequency at which the photodetector can operate. If R_L is a load resistance connected across a photodiode having a junction capacitance C_j, the band width (f_{BW}) can be expressed as,

$$f_{BW} = \frac{1}{2\pi R_L C_j} \quad \text{--(2.16)}$$

Similarly, the rise time t_r and band width can be related as,

$$t_r = \frac{0.35}{f_{BW}}$$

LED

Light emitting diodes (LED) are basically a p-n heterojunction device. Hence, apart from the basic heterojunction analysis, more detailed study on emission properties is needed. Spectral quality of the emission light is usually measured using a spectrometer and the intensity for each spectral line is plotted. From the emission spectrum the CIE color coordinates are calculated. The CIE coordinates of x=0.33 and y=0.33 usually indicate white light. Similarly, all colors are represented in this scale. Yet another study is the emission threshold where, the lowest voltage on which the emission starts.

Kiethley 4200 semiconductor analyzer was used to characterize the electrical properties of samples under the present study. More details on the characterization of the heterojunction devices can be found in the literature[49–51].

2.3 References

[1] L. V. Podrezova, S. Porro, V. Cauda, M. Fontana, G. Cicero, Appl. Phys. A 113 (2013) 623.

[2] X. Zhang, X. Han, J. Su, Q. Zhang, Y. Gao, Appl. Phys. A 107 (2012) 255.

[3] C.H. Chen, S.J. Chang, S.P. Chang, M.J. Li, I.C. Chen, T.J. Hsueh, A. Di Hsu, C.L. Hsu, J. Phys. Chem. C 114 (2010) 12422.

[4] K. Kitamura, T. Yatsui, M. Ohtsu, G.C. Yi, Nanotechnology 19 (2008) 175305.

[5] H.L. Zhou, S.J. Chua, H. Pan, Y.W. Zhu, T. Osipowicz, W. Liu, K.Y. Zang, Y.P. Feng, C.H. Sow, J. Phys. Chem. C 111 (2007) 6405.

[6] J. Chen, L. Ding, X. Zhang, L. Chu, N. Liu, Opt. Express 22 (2014) 7090.

[7] M. Willander, O. Nur, Q.X. Zhao, L.L. Yang, M. Lorenz, B.Q. Cao, J. Zúñiga Pérez, C. Czekalla, G. Zimmermann, M. Grundmann, A. Bakin, A. Behrends, M. Al Suleiman, A. El Shaer, A. Che Mofor, B. Postels, A. Waag, N. Boukos, A.

Travlos, H.S. Kwack, J. Guinard, D. Le Si Dang, Nanotechnology 20 (2009) 332001.

[8] E. Przeździecka, K. Gościński, M. Stachowicz, D. Dobosz, E. Zielony, J.M. Sajkowski, M.A. Pietrzyk, E. Płaczek-Popko, A. Kozanecki, Sensors Actuators A Phys. 195 (2013) 27.

[9] A. Ohtomo, M. Kawasaki, Y. Sakurai, Y. Yoshida, H. Koinuma, P. Yu, Z.K. Tang, G.K.L. Wong, Y. Segawa, Mater. Sci. Eng. B 54 (1998) 24.

[10] J. Podzemský, W. Schade, Organic solar cells based on ZnO nanowires layer, EEIC, Germany (2006) 1.

[11] Z.W. Liu, C.K. Ong, T. Yu, Z.X. Shen, Appl. Phys. Lett. 88 (2006) 1.

[12] R.S. Ajimsha, R. Manoj, P.M. Aneesh, M.K. Jayaraj, Curr. Appl. Phys. 10 (2010) 693.

[13] S. Xu, Z.L. Wang, Nano Res. 4 (2011) 1013.

[14] R.B. Peterson, C.L. Fields, B.A. Gregg, Langmuir 20 (2004) 5114.

[15] L. Vayssieres, Adv. Mater. 15 (2003) 464.

[16] J. Volk, T. Nagata, R. Erdélyi, I. Bársony, a. L. Tóth, I.E. Lukács, Z. Czigány, H. Tomimoto, Y. Shingaya, T. Chikyow, Nanoscale Res. Lett. 4 (2009) 699.

[17] S. Yamabi, H. Imai, J. Mater. Chem. 12 (2002) 3773.

[18] A. Ghosh, Y.G. Gudage, R. Sharma, R.S. Mane, S.-H. Han, Sensors & Transducers 98 (2008) 1.

[19] V. Consonni, E. Sarigiannidou, E. Appert, A. Bocheux, S. Guillemin, F. Donatini, I.C. Robin, J. Kioseoglou, F. Robaut, ACS Nano 8 (2014) 4761.

[20] T. Morita, S. Ueno, T. Tokunaga, E. Hosono, Y. Oaki, H. Imai, H. Matsuda, H. Zhou, M. Hagiwara, S. Fujihara, Cryst. Growth Des. 15 (2015) 3150.

[21] L. Xu, Y. Guo, Q. Liao, J. Zhang, D. Xu, J. Phys. Chem. B 109 (2005) 13519.

[22] R.A. Laudise, A.A. Ballman, J. Phys. Chem. 64 (1960) 688.

[23] M.A. Verges, A. Mifsud, C.J. Serna, J. Chem. Soc. Faraday Trans. 86 (1990) 959.

[24] L. Vayssieres, K. Keis, S.-E. Lindquist, A. Hagfeldt, J. Phys. Chem. B 105 (2001) 3350.

[25] F. Solís-Pomar, E. Martínez, M.F. Meléndrez, E. Pérez-Tijerina, Nanoscale Res. Lett. 6 (2011) 524.

[26] A.M.C. Ng, Y.Y. Xi, Y.F. Hsu, a B. Djurisić, W.K. Chan, S. Gwo, H.L. Tam, K.W. Cheah, P.W.K. Fong, H.F. Lui, C. Surya, Nanotechnology 20 (2009) 445201.

[27] W. Wu, G. Hu, S. Cui, Y. Zhou, H. Wu, Cryst. Growth

Des. 8 (2008) 4014.

[28] P.M. Aneesh, P.P. Subha, L.S. Vikas, S. Mohan, M.K. Jayaraj, Proc. SPIE 7766 (2010) 776606.

[29] C.H. Process, H. Zhang, D. Yang, D. Li, X. Ma, S. Li, Growth (Lakeland) (2005) 3.

[30] J.H. Wu, S.Y. Liu, S. Li, Y. long Jiang, G.P. Ru, X.P. Qu, Appl. Phys. A 109 (2012) 489.

[31] O. Lupan, T. Pauporté, L. Chow, G. Chai, B. Viana, V.V. Ursaki, E. Monaico, I.M. Tiginyanu, Appl. Surf. Sci. 259 (2012) 399.

[32] L. Tang, X.-B. Bao, H. Zhou, A.-H. Yuan, Phys. E Low-Dimensional Syst. Nanostructures 40 (2008) 924.

[33] P.M. Aneesh, K.A. Vanaja, M.K. Jayaraj, Semiconductors 6639 (2007) 66390J 1.

[34] P.M. Aneesh, C.T. Cherian, M.K. Jayaraj, T. Endo, J. Ceram. Soc. Japan 118 (2010) 333.

[35] F. Li, L. Hu, Z. Li, X. Huang, J. Alloys Compd. 465 (2008) L14.

[36] L.L. Liew, H.Q. Le, G.K.L. Goh, Mater. Res. Innov. 15 (2011) 357.

[37] L.E. Greene, M. Law, J. Goldberger, F. Kim, J.C. Johnson, Y. Zhang, R.J. Saykally, P. Yang, Angew. Chem. Int. Ed.

Engl. 42 (2003) 3031.

[38] T. Konya, Rigaku J. 25 (2009) 1.

[39] T. Damen, S. Porto, B. Tell, Phys. Rev. 142 (1966) 570.

[40] A. Khan, J. Pakistan Mater. Soc. 4 (2010) 5.

[41] Y.M. Hu, C.Y. Wang, S.S. Lee, T.C. Han, W.Y. Chou, G.J. Chen, J. Raman Spectrosc. 42 (2011) 434.

[42] Z.W. Dong, C.F. Zhang, H. Deng, G.J. You, S.X. Qian, Mater. Chem. Phys. 99 (2006) 160.

[43] Y.W. Chen, Y.C. Liu, S.X. Lu, C.S. Xu, C.L. Shao, C. Wang, J.Y. Zhang, Y.M. Lu, D.Z. Shen, X.W. Fan, J. Chem. Phys. 123 (2005) 134701.

[44] H. Zhu, J. Iqbal, H. Xu, D. Yu, J. Chem. Phys. 129 (2008) 124713.

[45] P.A. Rodnyi, I. V. Khodyuk, Opt. Spectrosc. 111 (2011) 776.

[46] C.H. Ahn, Y.Y. Kim, D.C. Kim, S.K. Mohanta, H.K. Cho, J. Appl. Phys. 105 (2009) 013502.

[47] M. Gomi, N. Oohira, K. Ozaki, M. Koyano, Jpn. J. Appl. Phys. 42 (2003) 481.

[48] M. Wang, Y. Zhou, Y. Zhang, E. Jung Kim, S. Hong Hahn, S. Gie Seong, Appl. Phys. Lett. 100 (2012) 101906.

[49] P.F. Robert, Semiconductor Device Fundamentals,

Addison-Wesley Pblishing Company, New York (1996).

[50] S M Sze, Physics of Semiconductor Devices, John Wiley & Sons, New Jersey (2007).

[51] D.K. Schroder, Semiconductor Material and Device Characterization, John Wiley & Sons Inc., New York (2007).

[52] X. Liu, L. Gu, Q. Zhang, J. Wu, Y. Long, Z. Fan, Nat. Commun. 5 (2014) 4007.

[53] Y. Kim, S.J. Kim, S. Cho, B.H. Hong, D. Jang, Sci. Rep. 5 (2015) 12345.

Chapter 3

Study of dependence of substrate surface on the electrochemical growth of ZnO nanorods

3.1 Introduction

The wide band gap metal oxide semiconductor ZnO attracts scientific attention because of its mechanical, electrical and optical properties. High surface area to volume ratio of ZnO nanostructures makes them even more attractive. Various nanostructures including nanoparticles[1,2], nanowires[3,4], nanorods[5,6], nanotubes [3,7,8], nanoplates[6,9], nanoflower[10], nanoribbons[11], etc. have been successfully fabricated using various techniques like vapor liquid solid deposition[12], chemical vapor deposition[13,14], pulsed laser deposition[15,16], molecular beam epitaxy[17], hydrothermal synthesis[18,19], electrodeposition[20], solution processing

[21–23] etc. Most of these techniques are expensive and require high temperature processing. Among the above mentioned techniques electrodeposition has many advantages. Electrodeposition is an environment friendly technique with high yield and requires only low temperature processing. The control of size and shape is easy compared to other techniques. ZnO nanorod electrodeposition can be generally classified into template assisted technique [24,25] and template free growth technique. Template assisted technique utilizes some kind of porous or patterned scaffold to selectively deposit ZnO into the available voids to form 1D nanostructures. In template free growth process ZnO nanorods are anisotropically grown over suitable substrate.

Electrodeposition uses an applied potential to force ZnO formation over a working electrode. The process is generally performed in a three electrode system, where the conducting substrate on which ZnO to be grown is kept as working electrode (WE). The potential is applied with respect to a reference electrode (RE) and another counter electrode (CE) is used to collect the current in the electrochemical cell. Whether the shape of substrate is flat, curved or even flexible, nanorods can be grown over the conducting substrate. ZnO nanorods can be grown by electrodeposition uniformly over large area, which helps to achieve even wafer scale production of ZnO nanorods. One major disadvantage of electrodeposition is that the substrate, where the deposition needs to be performed, should be conducting.

In general, electrodeposition of ZnO involves two steps. Formation of Zinc hydroxide complex due to the hydroxylation of Zn is the first step. The second step involves decomposition of the formed Zinc complex to form crystalline or amorphous ZnO.

$$Zn^{2+} + 4OH^- \rightarrow Zn(OH)_4^{2-}$$

$$Zn(OH)_4^{2-} \rightarrow ZnO + 2H_2O$$

During solution growth process of ZnO nanorods, the growth rate is not equal in all crystal directions. The fastest growth direction is along [0 0 0 1]. Hence the longer dimension of the formed nanorod will be usually along [0 0 0 1]. By suitably altering the growth conditions growth rate along various crystal planes can be altered, which can lead to the formation of different shaped nanostructures. M. Izaki et. al.[20], and S Peulon[26] et al. separately reported the electrochemical synthesis of ZnO for the first time in 1996. Later, various ZnO nanostructures such as hexagonal rods, woven nanoneedles, rhombohedral rods etc, have been synthesized. Xu et al. demonstrated the formation of hierarchical ZnO nanostructures by two step electrodeposition process[27]. Zinc nitrate based electrolyte along with various salts such as KCl, NH_4F, ethylene diamine(EDA), CH_3COONH_4, etc[28] are generally used for the synthesis of ZnO nanostructures. There are several reports on the use of various electrolytes for electrodeposition such as $ZnCl_2$ & KCl solution[5,29], Zinc acetate and dimethyl sulfox-

ide(DMSO) solution[30], $ZnSO_4$ and Na_2SO_4 along with H_2O_2 solution[24] etc., which can form wurtzite crystalline ZnO nanorods.

Cyclic voltammetric studies indicate the need to apply a potential of -1.2 V at working electrode with respect to the reference electrode to form good quality crystalline ZnO nanorods. Even Cui et al. reported that application of -1.2 V can yield high growth rate and nucleation density for $ZnCl_2$ based electrolyte[31]. Use of ZnO based seed layer also can affect the density of nanorods. Temperature of precursor solution during electrodeposition process also influences the morphology of nanorods formed. Formation of ZnO in electrodeposition follows a nucleation and growth process. Hence, nanorod growth during initial stages of electrodeposition is critical. It is already reported that the relative faster growth rate along c-axis yields ZnO nanorods. But, there are only a few reports on the effect of seed layer on the orientation and crystallinity of nanorods. Nanorod growth over four different types of substrates was investigated. The dependence of substrate surface and use of seed layer on the orientation and other structural and optical properties of nanorods were investigated in the present study.

3.2 Experimental

ZnO nanorods were grown over four commonly used TCO coated substrates. The substrates include ITO coated glass substrate(ITO), FTO coated glass substrate(FTO), ITO coated PET

substrate(PET), ZnO:Al coated glass substrate(AZO). The AZO film was deposited using sputtering over corning 1737F glass substrate. ZnO nanorods were grown over these substrate by electrodeposition techniques.

Prior to ZnO nanorod growth all substrates were cleaned using, soap solution, Acetone, isopropyl alcohol (IPA) and water in ultrasonicator. ZnO seed layer was deposited over the cleaned substrates by sputtering. A compacted powder target of ZnO was used to deposit ZnO seed layers of thickness 5 nm, 10 nm, 20 nm & 30 nm. The base pressure of sputtering chamber was 2 X 10^{-5} mbar and then Ar was introduced as the sputtering gas to get a working pressure of 2.5 X 10^{-5} mbar. Serene IPC RF power supply was used to deliver 25W RF power to the sputtering target. Sputtering time was varied to obtain suitable seed layer thicknesses.

Seed layer coated substrates was used as working electrode for electrodeposition process. Platinum (Pt) was counter electrode and saturated calomel electrode was used as the reference electrode. A precursor solution of 0.05 mM $ZnCl_2$ along with 0.1 M KCl was used as the electrolyte for the electrodeposition process. The solution was kept at 80°C throughout the experiment. Biologic SP300 potentiostat/galvanostat was used to apply -1.2 V potential at working electrode with respect to the counter electrode. The potential was applied for 2000 s for all the samples. Constant stirring and Oxygen bubbling were performed during the electrodepo-

sition process. After electrodeposition the working electrode was thoroughly cleaned in water and dried in nitrogen. A post deposition annealing was performed at 350°C for 6 hours.

Carl Zeiss Ultra 55 FESEM was used to study the morphology of the grown ZnO nanorods. PANAlytical X'Pert PRO high resolution X-ray diffractometer was used to study the structural properties of the nanorods. Raman spectrum and photoluminescence measurements of the nanorods were performed in HORIBA JOBIN YVON Labram HR Raman spectrometer, coupled with He-Ne, Ar ion, and He-Cd laser. The He-Cd laser (325 nm) was the excitation UV light for photoluminescence measurements. Ar ion laser is generally used for Raman measurements. Transmission spectra of the samples were taken in Jasco V370 UV-Vis-NIR spectrophotometer.

3.3 Results and Discussions

3.3.1 Structural Studies

The electrodeposition is performed on 4 different kind of TCO substrates. ITO coated glass(ITO) is widely used in optoelectronic applications. SnO_2:F (FTO) coated glass substrate is a textured substrate generally used for solar cell applications. ITO coated PET substrate (PET) is a flexible substrate and ZnO:Al (AZO) coated glass substrate has lower mismatch for growing ZnO. On each TCOs, a sets of 5 substrates were used which con-

tains 0 nm, 5 nm, 10 nm, 20 nm and 30 nm ZnO seed layers. The 0 nm seed layer substrate indicates that the substrate is used without any seed layer.

To study the crystallinity of the electrochemically grown samples, glancing angle X-ray diffraction studies were performed. The X-ray diffraction pattern for nanorods on FTO (figure 3.1(a)), ITO (figure 3.1(b)), PET (figure 3.1(c)) and AZO (figure 3.1(d)) substrates are shown in figure 3.1. The dependence of seed layer on the crystallinity of nanorods are also investigated. All samples showed crystalline wurtzite crystal structure, and preferred orientation is seen for some samples. The peaks matches well with the X-ray pattern of ZnO (ICSD 98-000-9341). For nanorods grown over FTO and ITO substrates, peaks corresponding to numerous crystal planes are visible. For nanorods grown over PET and AZO few crystalline peaks are visible.

To get an idea of the crystallinity of nanorods, the texture coefficients were calculated. The texture coefficient is a mathematical tool which calculates the preferred orientation of the sample among various crystal planes available.

The texture coefficient is calculated from the equation,

$$T_{hkil} = \frac{I_{hkil}/I_0}{\frac{1}{N}\sum_{n=1}^{N}\left[I_{hkil}/I_0\right]}$$

Where, I_{hkil} is the intensity obtained from XRD measurement corresponding to (hkil) crystal plane. I_0 is the relative intensity obtained from the reference data, ICSD 98-000-9341. N is the total number of the crystal planes observed. In the present study N is taken as 11. For a highly preferred oriented sample the texture coefficient T_{hkil} for a particular crystal plane (hkil) will be close to 11.

The texture coefficients were calculated and plotted for nanorods grown over FTO, ITO, AZO and PET substrates after postdeposition annealing at 350°C for 6 hour in air is shown in figure 3.2 (a), (b), (d) respectively. Post deposition annealing is not performed for nanorods over PET substrate as the flexible substrate cannot withstand high temperature processing (figure 3.2 (c)).

For nanorods grown over FTO substrate, the texture coefficients showed no clear preferred orientation. Still the (0002) crystal plane orientation is better than rest of the planes. As seed layer thickness increases, the (0002) preferred orientation show a decreasing trend. Even after the post deposition annealing the trend is more or less the same with slight improvement for (0002) crystal plane orientation.

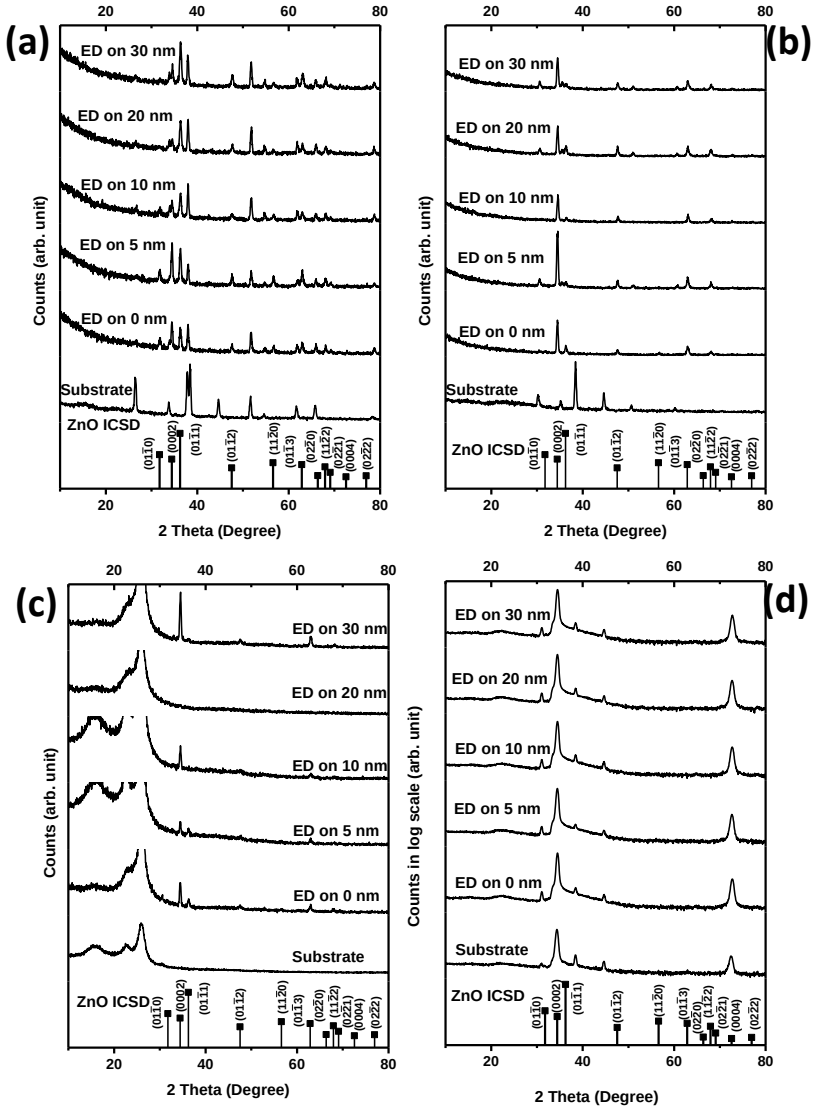

Figure 3.1: The xrd spectrum of nanorods grown over (a) FTO coated glass, (b) ITO coated glass, (c) ITO coated PET substrate and (d) AZO coated glass plate and its variation with seed layer thickness.

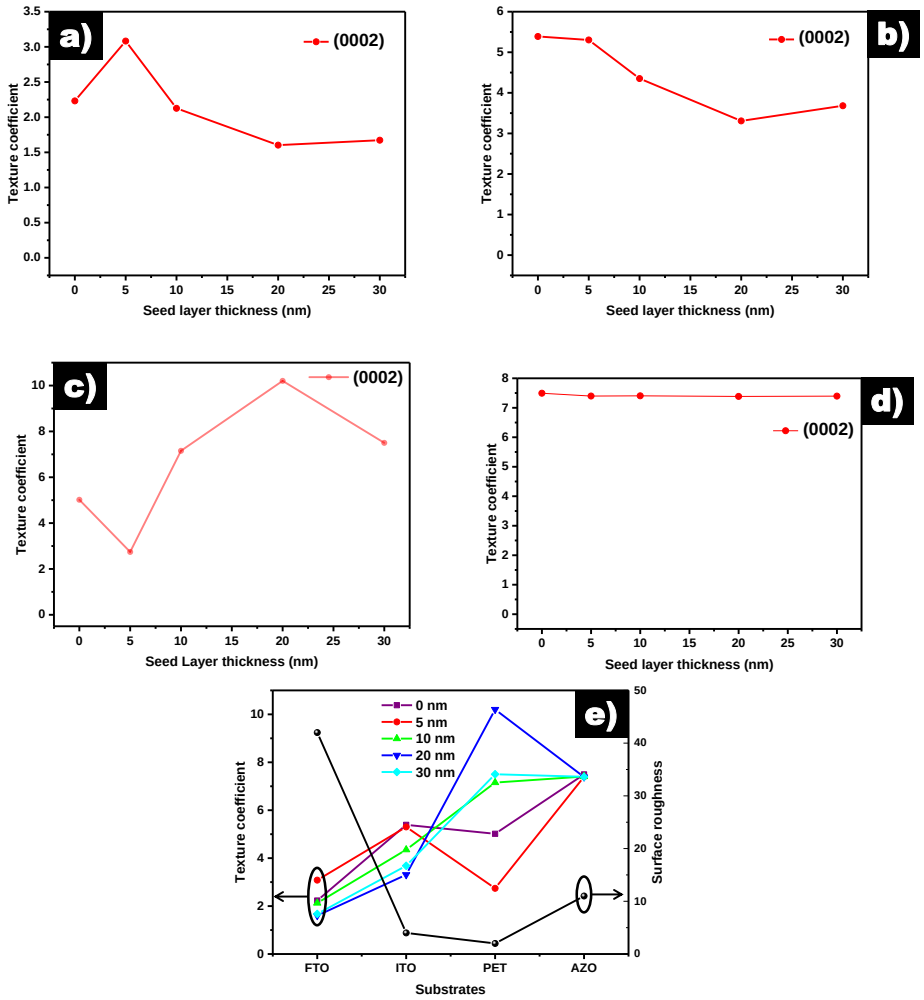

Figure 3.2: The variation of texture coefficients of (0002) crystal planes of ZnO with seed layer thickness, grown on (a) FTO, (b) ITO and (d) AZO after post deposition annealing in air. (c) The texture coefficients of (0002) crystal plane of as grown ZnO with different seed layer thickness over PET substrate. (e) The dependence of seed layer thickness and surface roughness of substrates on texture coefficient.

For nanorods over ITO substrate, the T_{0002} values are high compared to other planes indicating preferred orientation for (0002) crystal planes. As seed layer thickness increases the (0002) crystal plane showed decreasing preferred orientation with decreasing T_{0002} values. While the trend is reverse for (0004) crystal plane, where the T_{0004} values showed an increasing trend. All other crystal planes showed more random orientation. The trend is the same for as deposited samples and for samples after post deposition annealing.

Nanorods over AZO substrate showed only (0002) and (0004) planes. Hence these planes had high texture coefficients, with (0002) showing high preferential orientation. Seed layer thickness and post deposition annealing have no significant effect on the preferred orientation of crystal planes in these samples.

Since PET substrate cannot withstand high temperature processing, texture coefficient only for the as deposited sample is calculated. Here also (0002) plane shows high texture coefficient indicating preferred orientation in this direction. As seed layer thickness increases the general trend is that the (0002) texture coefficient is increasing. This shows that seed layer thickness has some dependence on the preferred orientation of (0002) crystal plane.

Since (0002) crystal plane showed preferred orientation in most samples, its dependence on seed layer thickness and surface

roughness of the substrate, for all the four substrates are plotted(figure 3.2 (e)). Here FTO and ITO shows slightly decreasing texture coefficient with increasing seed layer thickness. At the same time PET sample showed an increasing texture coefficient on increasing seed layer thickness. AZO didn't show any notable change of texture coefficient on changing the seed layer thickness.

FESEM image of ZnO nanorods grown over FTO substrate with seed layers 0 nm, 5 nm, 10nm, 20 nm and 30 nm are shown in figure 3.3 (a), (b), (c), (d) and (e) respectively. It is seen that the density of nanorods are increasing for samples with higher seed layer thickness. As seed layer thickness increases the density of nanorods increases as more and more nanorods with lesser diameter are seen along with bigger nanorods. The orientation of the nanorods tends to vertical on increasing the seed layer thickness. Roughness of the substrate surface is evident from the FESEM image (figure 3.3(f)).

The properties of nanorods over ITO substrate is also similar to that in FTO. Figure 3.4 (a), (b), (c), (d) and (e) shows the FESEM images of ZnO nanorods grown over ITO substrate with 0 nm, 5 nm, 10 nm, 20 nm and 30 nm seed layer thickness respectively. The tendency of vertical growth and density of nanorods are increasing with seed layer thickness. Similarly along with longer nanorods more and more smaller nanorods are seen for samples with thick seed layer.

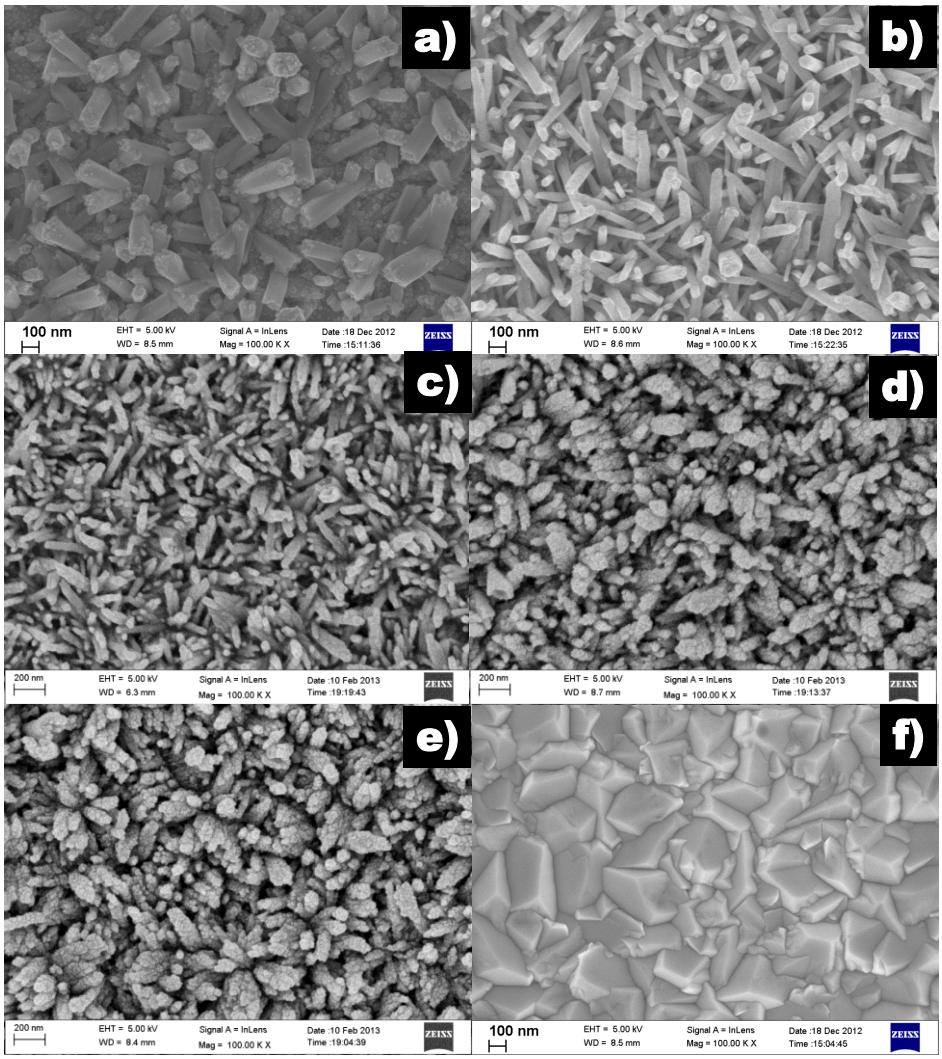

Figure 3.3: FESEM micrographs of ZnO nanorods grown over FTO coated glass substrate with seed layers of thickness (a) 0nm, (b) 5nm, (c) 10nm, (d) 20 nm and (e) 30nm. (f) is the FESEM micrographs of bare FTO substrate surface.

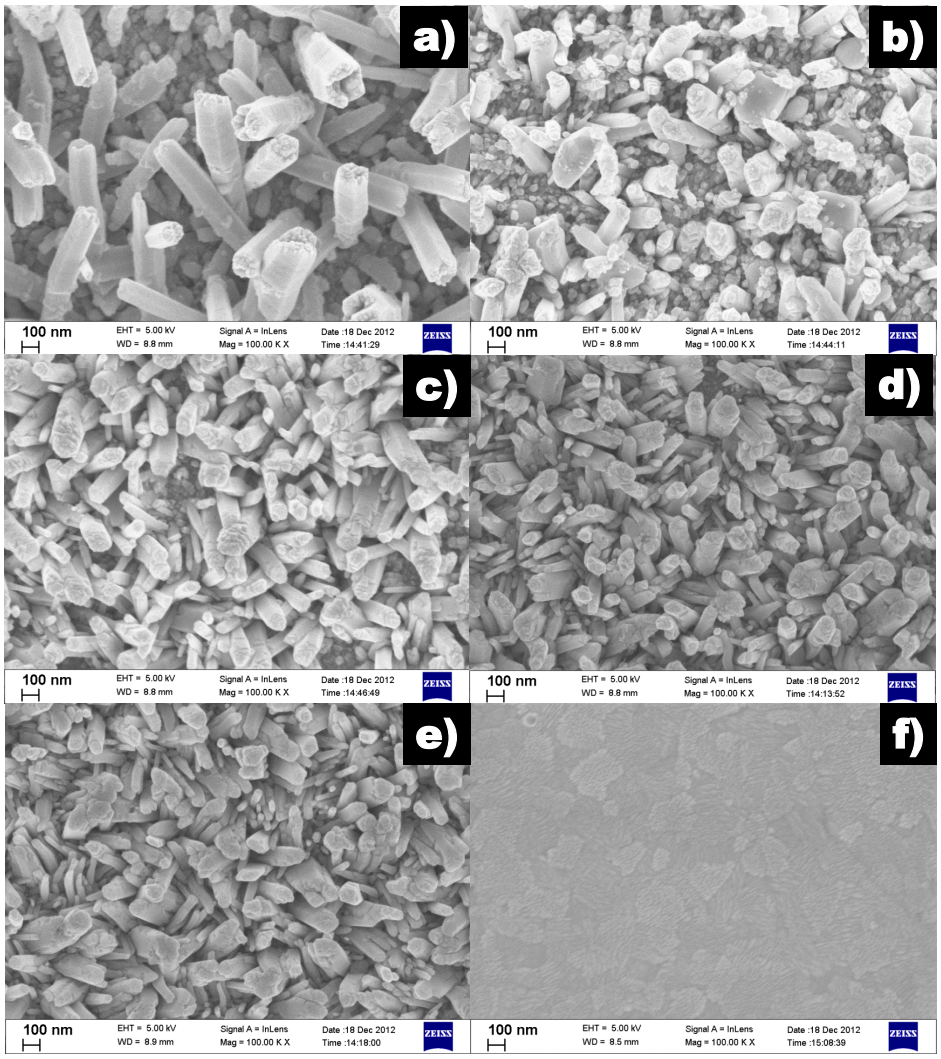

Figure 3.4: FESEM micrographs of ZnO nanorods grown over ITO coated glass substrate with seed layers of thickness (a) 0nm, (b) 5nm, (c) 10nm, (d) 20 nm and (e) 30nm. (f) is the FESEM micrographs of bare ITO substrate surface.

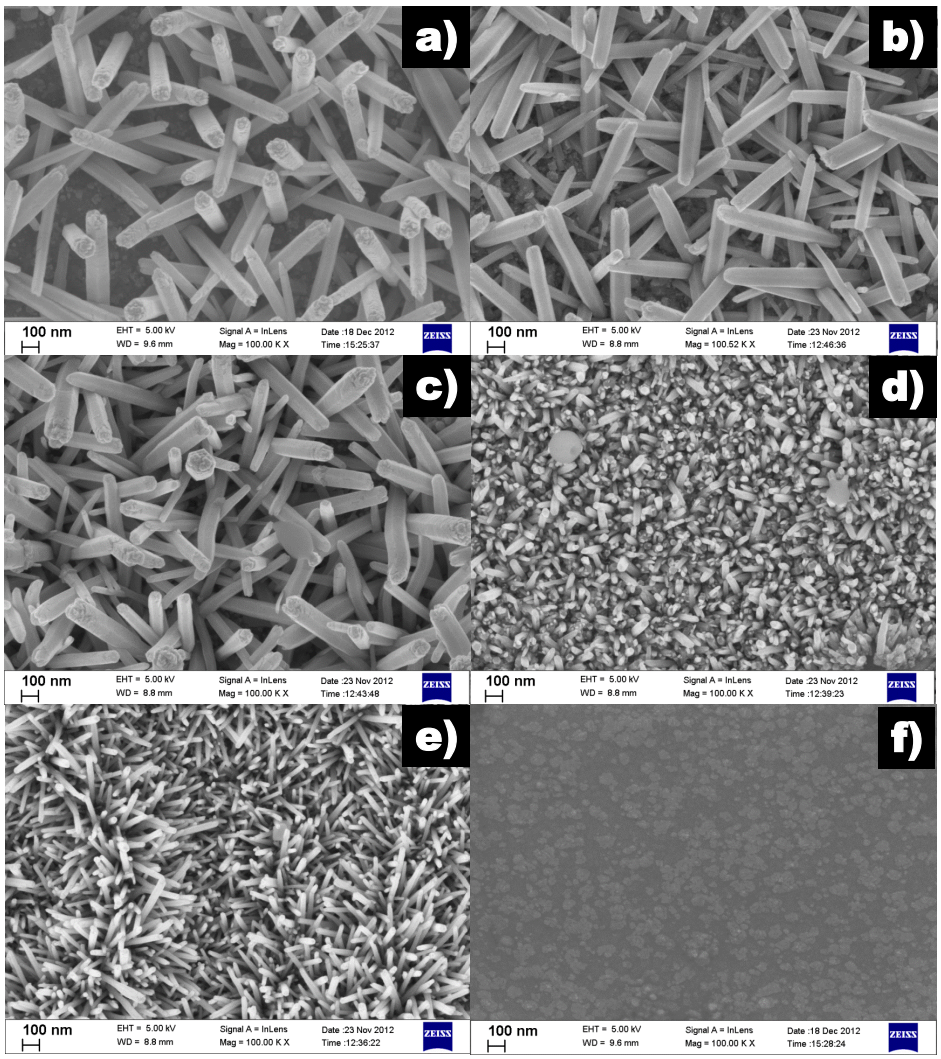

Figure 3.5: FESEM micrographs of ZnO nanorods grown over ITO coated PET substrate with seed layers of thickness (a) 0nm, (b) 5nm, (c) 10nm, (d) 20 nm and (e) 30nm. (f) is the FESEM micrographs of bare ITO coated PET substrate.

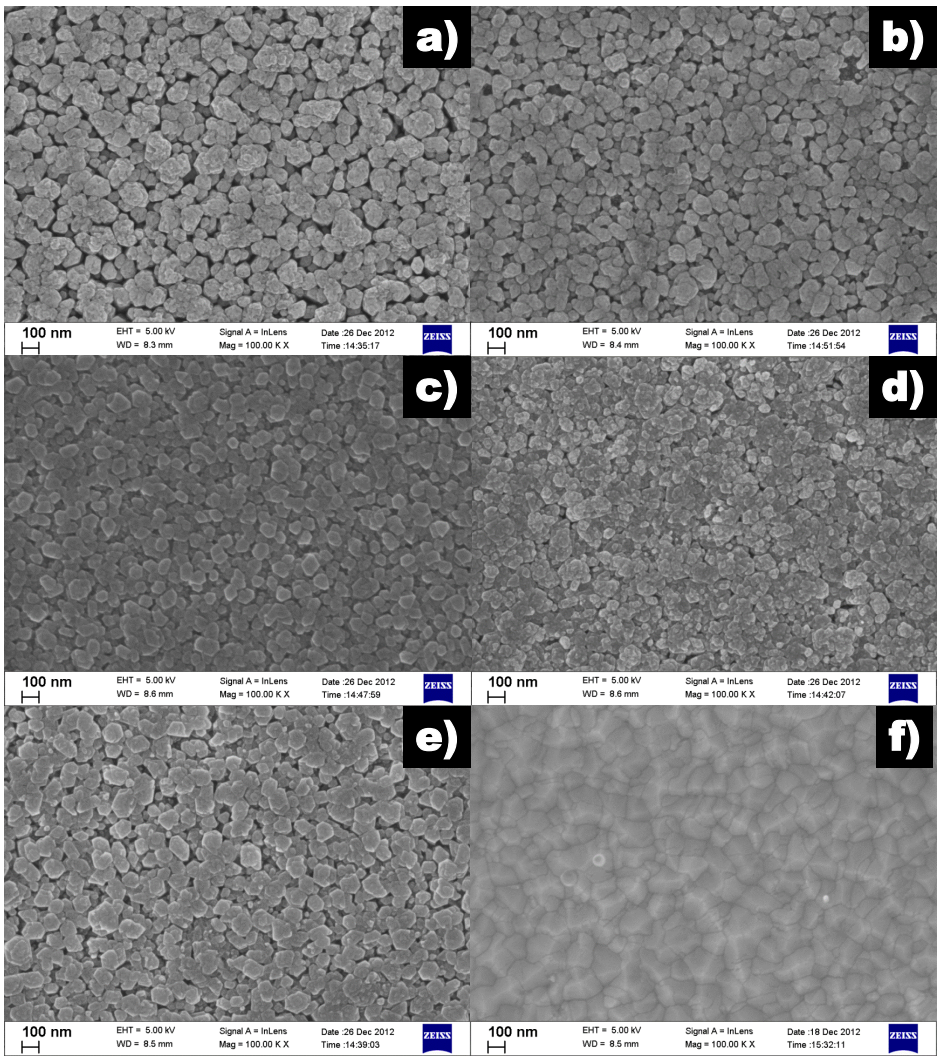

Figure 3.6: FESEM micrographs of ZnO nanorods grown over AZO coated glass substrate with seed layers of thickness (a) 0nm, (b) 5nm, (c) 10nm, (d) 20 nm and (e) 30nm. (f) is the FESEM micrographs of bare AZO coated glass substrate.

Top view of FESEM image of ZnO nanorods over PET substrate with 0 nm, 5 nm, 10 nm, 20 nm and 30 nm ZnO seed layer is seen in figure 3.5(a), (b), (c), (d) and (e) respectively. The tendency to grow nanorods vertically is increasing in this sample along with the increase in seed layer thickness. Though smaller nanorods are seen for samples with thicker seed layer, the overall variation of width of nanorods in a particular sample is small compared to FTO and ITO substrates. Density of nanorods is increasing with seed layer thickness. The FESEM image of ITO coated PET substrate surface is shown in figure 3.5 (f).

The top view of FESEM images of ZnO nanorods grown over AZO substrate with seed layers of thickness 0 nm, 5 nm, 10 nm, 20 nm and 30 nm are shown in figure 3.6 (a), (b), (c), (d) and (e) respectively. For AZO samples the nanorods seems more compact compared to samples on other substrates. The adjacent sides of the nanorods are touching together. Hence, it seems that the grown nanorods constitute a thick film structure. All AZO samples showed almost the same vertical orientation for the nanorods irrespective of the seed layer thickness. The FESEM image of AZO substrate surface is seen in figure 3.6 (f).

To get an idea about the changes in the size of nanorods, cross sectional FESEM images were also taken and the size of the nanorods are measured. The changes in the height and width of nanorods with seed layer thickness are plotted in figure 3.7(a) and

(b) respectively. Except for AZO substrate all other substrate showed that both nanorod height and width decreases with the thickness of seed layer. For AZO substrate, since the changes in dimensions are within the error bar, it can be concluded that the dimensions of nanorods over AZO is almost a constant.

The observed changes of vertical nature of ZnO nanorods as seen in FESEM images, and they matches well with texture coefficients extracted from the X-ray diffraction studies.

The AFM images (figure 3.8) show the surface roughness the substrates. The RMS roughness calculated from the AFM analysis is tabulated in table 3.1. Thus FTO substrate surface has very high roughness whereas PET surface is the smoothest among the substrates used in the present study.

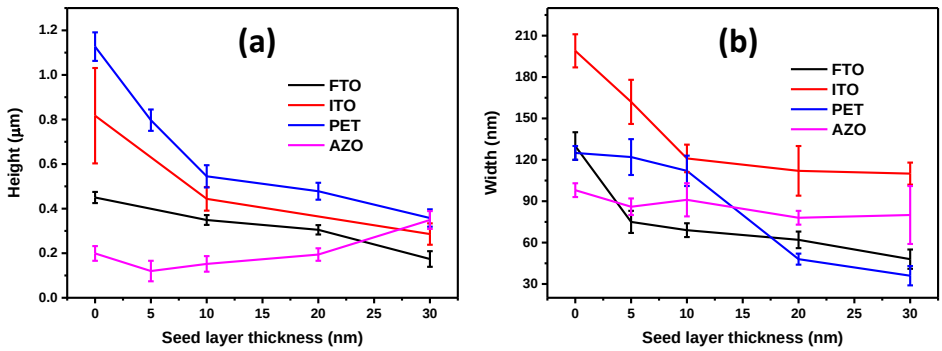

Figure 3.7: The ZnO nanorod (a) height and (b) width variation on various substrate for different seed layer thicknesses.

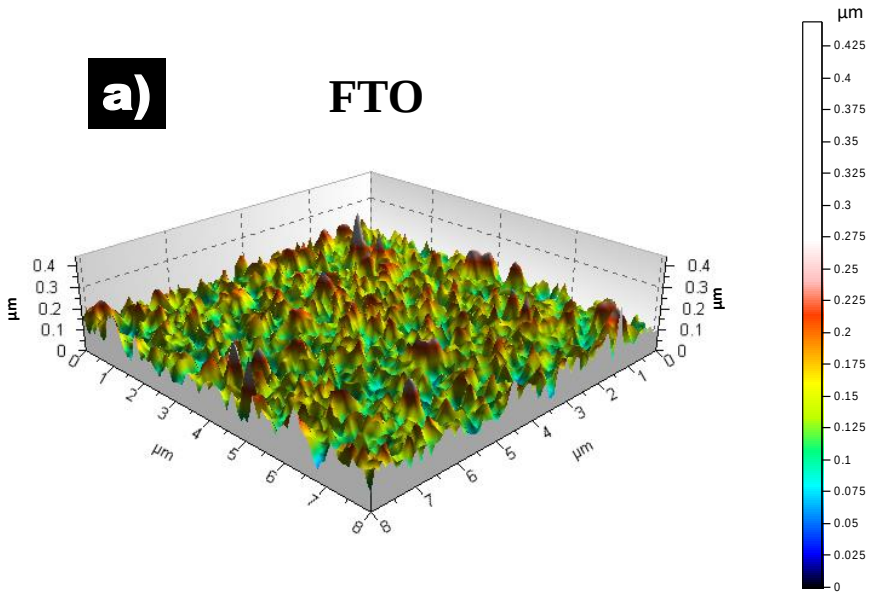
a)
FTO
µm
0.4
0.3
0.2
0.1
0
µm
0 1 2 3 4 5 6 7 8
µm
0 1 2 3 4 5 6 7 8
µm
0.425
0.4
0.375
0.35
0.325
0.3
0.275
0.25
0.225
0.2
0.175
0.15
0.125
0.1
0.075
0.05
0.025
0

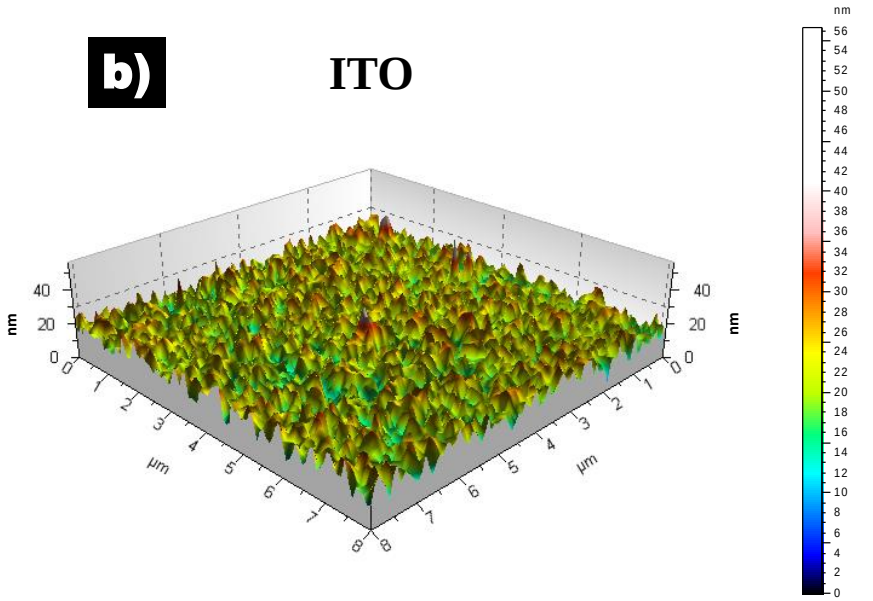
b)
ITO
nm
40
20
0
nm
0 1 2 3 4 5 6 7 8
µm
0 1 2 3 4 5 6 7 8
µm
nm
56
54
52
50
48
46
44
42
40
38
36
34
32
30
28
26
24
22
20
18
16
14
12
10
8
6
4
2
0

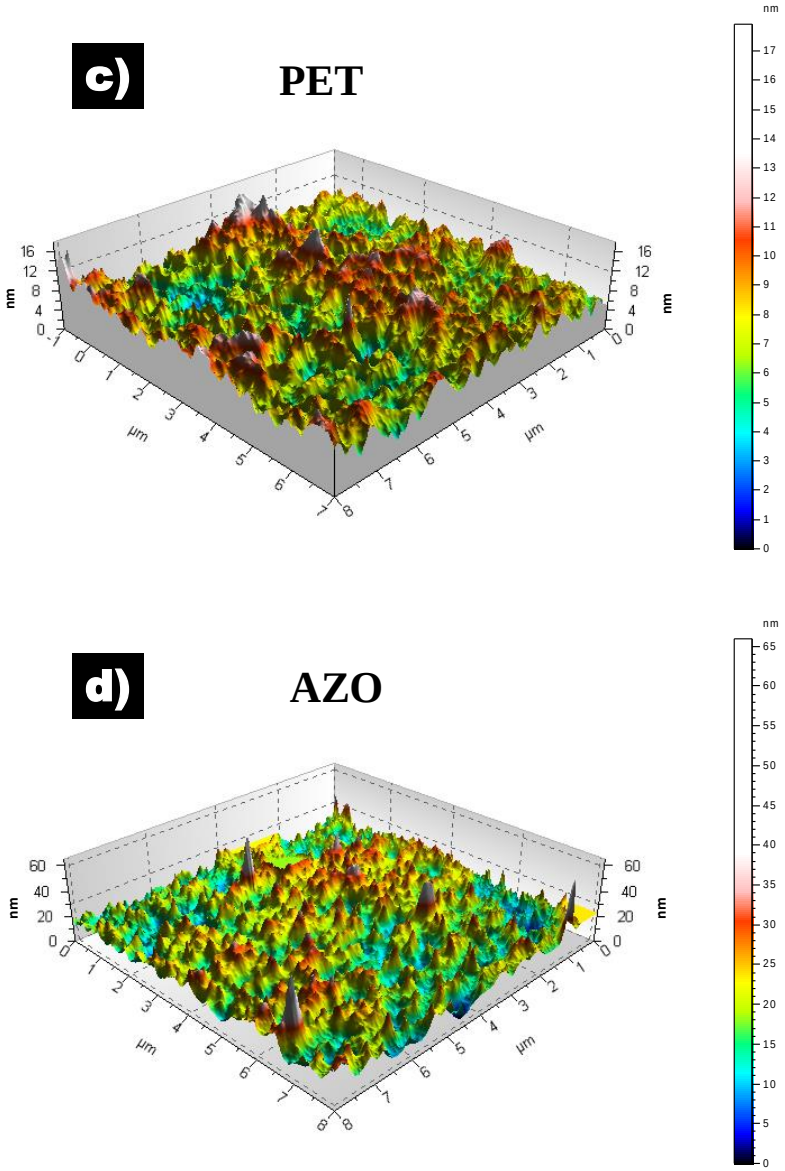

Figure 3.8: The AFM image of the surface of (a) FTO, (b) ITO, (c) PET and (d) AZO substrates.

Table 3.1: The RMS roughness of sample surfaces calculated from AFM analysis.

Substrate	**RMS roughness (nm)**
FTO	40.1
ITO	4.73
PET	2.01
AZO	11.4

Comparing the results, we could say that the growth properties of ZnO nanorods indeed depend on the surface properties, which is clear from figure 3.2. For the growth of ZnO nanorods over rougher substrates the texture coefficient is low compared to smooth substrates. This points out the fact that for rougher samples the c-axis orientation is poor compared to smooth surfaces. Yet, for AZO substrate, though the RMS roughness is higher than ITO and PET, the texture coefficient in AZO substrate is higher. Since the surface of AZO substrate is doped ZnO, the nanorods have lesser lattice mismatch with AZO substrate. Due to good lattice match the nanorods grow easily over AZO compared to other substrates. Hence, providing additional seed layer over AZO substrate didn't make any difference. This result is consistent with texture coefficient for samples with various seed layer thicknesses.

During the initial phase of ZnO nanorod growth via electrodeposition process, the nucleation starts from a seed. Hence, providing a rougher substrate surface leaves a number of potential seed points, where the nanorod starts to nucleate and grow larger. As the ZnO seed layer thickness increases, more and more nucleation sites are created which offers more number of nanorod growth resulting in increased density of nanorods.

For a potential applied between electrodes in an electrolyte with particular electrolyte concentration, the ionic density will be constant. Hence, during nanorod growth each nucleation site will try to acquire maximum of available ions in order to deposit ZnO. Because of this competition, bigger nanorods start to grow bigger and bigger, as the rate of acquisition will be large here, leaving smaller nanorods with shortage of available ions. This may be the reason for the observation of wide range of nanorods with various sizes as the seed layer thickness increases. Again as the total ionic density is constant, larger number of nucleation sites means the available charge will be distributed among all active nucleation sites. This is why the mean size (height and width) of the nanorods decreases as seed layer thickness increases.

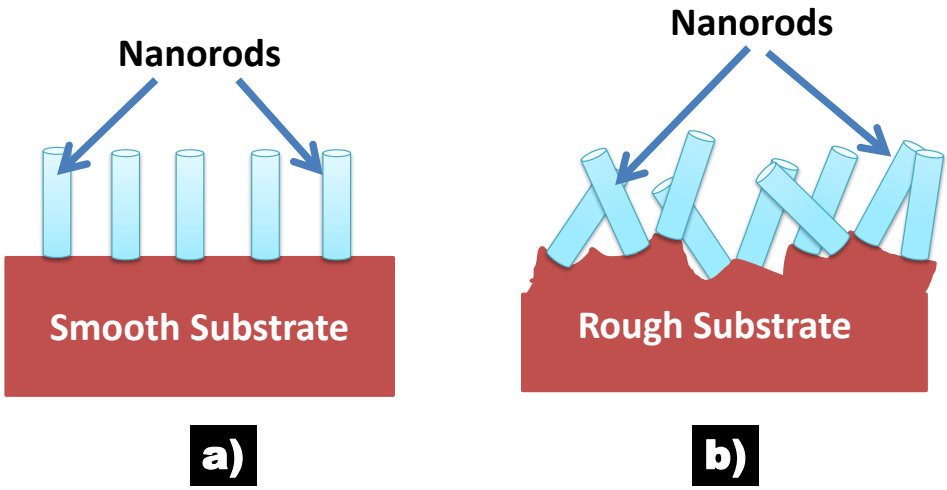

Figure 3.9: Diagram showing the growth of nanorods over (a) smooth and (b) rough substrates.

A critical factor which decides the orientation of nanorod growth is the surface roughness. The FESEM images indicate that nanorods always try to grow vertical to substrate surfaces. Any substrate can have a large number of surface irregularities like hills and valleys structure. If these surface variations are smaller compared to the nanorod dimensions these surface irregularities will be treated as seed or potential nucleation sites. Hence, for smoother surfaces, the nanorods grow vertical to the surface. It is seen in the figure 3.9(a). For rough surfaces, which usually possess large hills and valleys structures, the surface irregularities may be larger than the nanorod dimensions. In this case the hills and valley may not be considered as seeds, rather each hill structure possess a number

of seed points. Here also each nanorod will start to grow vertical to its base surface. But, the overall effect of the nanorod growth will be tilted rather than vertical, because of the surface roughness.

Because of this, for rough samples like FTO and ITO the thickness of seed layer thickness cannot improve vertical nature, rather it worsen the preferred vertical growth. For the smoother substrate, PET, the lattice misfit affects the preferred orientation of nanorods. But the thicker seed layer improve the surface roughness of already smooth surface leaving a lattice matched surface for nanorod growth, which in turn improves the preferred orientation.

3.3.2 Optical Studies

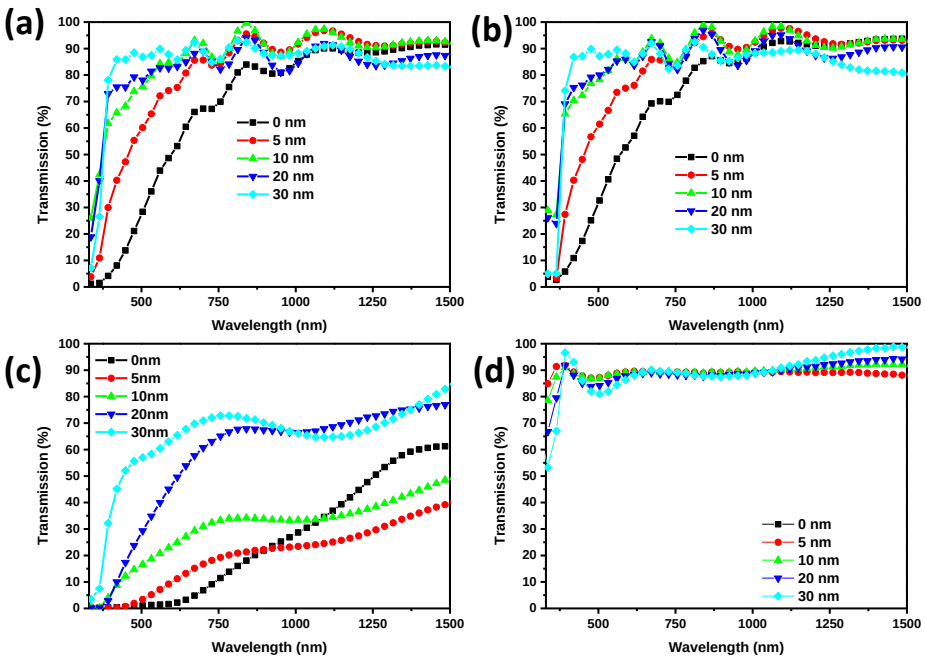

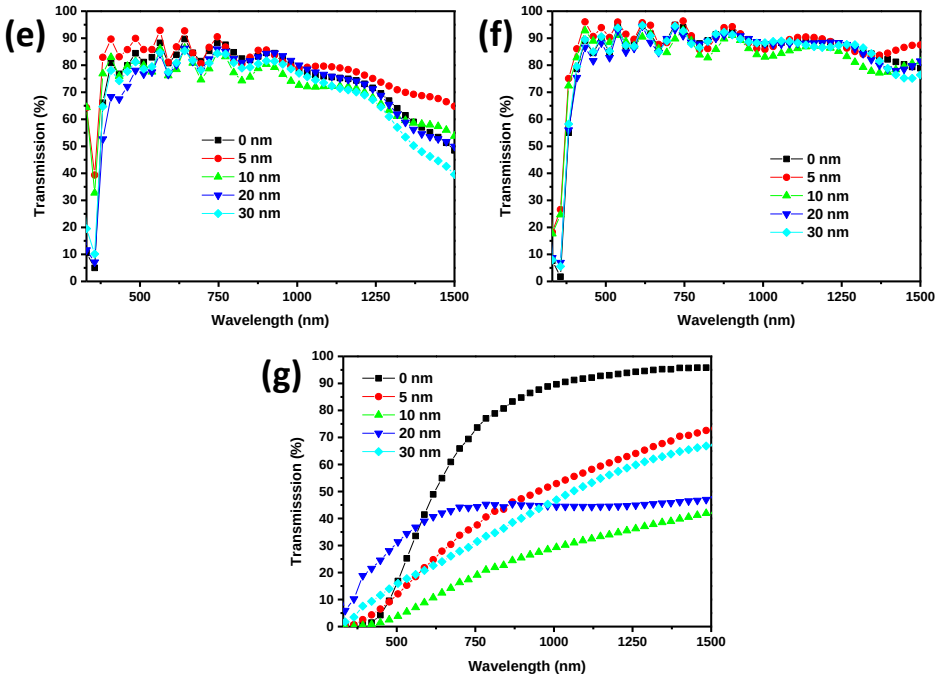

Figure 3.10: The transmission spectra of ZnO nanorods grown on different substrates with various seed layer thicknesses. (a) FTO before annealing. (b) FTO after annealing. (c) ITO before annealing. (d) ITO after annealing. (e) AZO before annealing. (f) AZO after annealing. (g) PET before annealing.

The transmission spectrum of ZnO nanorods grown over FTO, ITO, AZO and PET substrate before annealing (figure 3.10(a, c, e, g) respectively) and after post deposition annealing (figure 3.10(b, d, f) are shown. Since PET substrate cannot withstand the high temperature processing the studies are limited to as

prepared samples over PET substrate. As deposited samples shows slightly poor transmission especially in the visible region, this may be due to the presence of various defects in the sample. The transmission percentage increases on post deposition annealing, which may be due to the improved crystallinity of sample as indicated by X-ray diffraction studies. The annealed samples showed above 80% transparency in visible light and in near infra-red region.

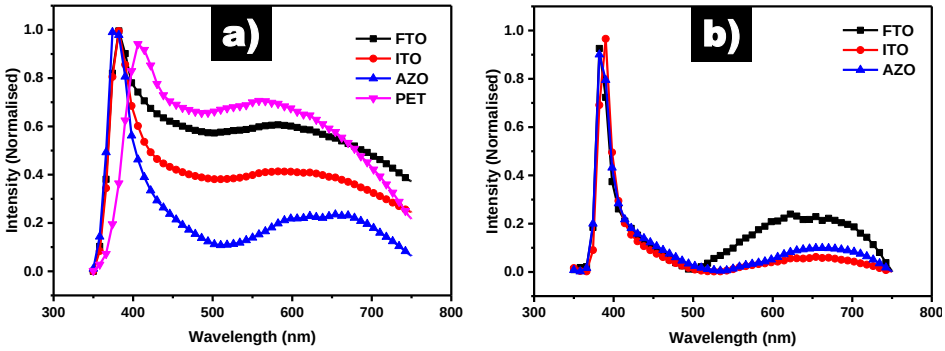

Figure 3.11: The photoluminescence spectrum of ZnO nanorods grown over different substrates (a) before and (b) after post deposition annealing.

The photoluminescence spectrum of ZnO nanorods are shown in figure 3.11. The spectrum consists of two regions. The sharp emission around 380 nm is the near band edge (NBE) emission. The broad deep level emission (DLE) ranging from 500 nm to around 750 nm is due to the presence of various defects in the ma-

terial. The presence of impurities and crystalline defects creates additional energy levels in the sub bandgap region. Transition of electrons through these energy levels leads to the presence of broad emission. On annealing the DLE emission intensity is decreased, indicating the improvement on the crystalline property of the nanorods.

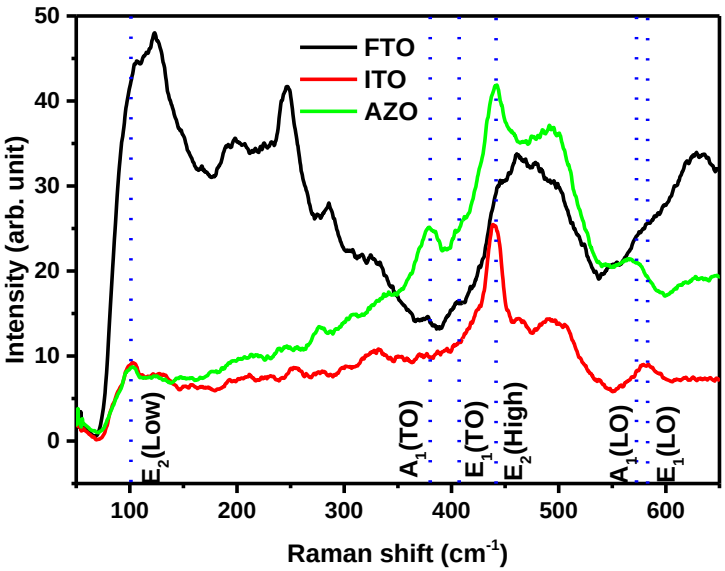

Figure 3.12: Raman spectrum of ZnO nanorods over various substrates after post deposition annealing.

Raman spectrum is a confirmation for the formation of crystalline ZnO nanorods. The presence of prominent Raman

peaks corresponding to the Raman modes E_2(Low), A_1(TO), E_2(High), A_1(LO) and E_1(LO) as suggested from theoretical calculations matches with the observed data as shown in the figure 3.12 [32–35]. Presence of intense E_2(High) mode at 437cm^{-1} is a signature of c-axis oriented growth[33]. A_1(TO) mode is formed by the polarized phonons parallel to c-axis, and E_1(TO) modes is formed by the polarized phonons perpendicular to c-axis. Hence their presence shows the strength of polar bonds in respective directions inside ZnO nanorod lattice. Very feeble presence of E_1(TO) mode confirms that crystallinity along c-axis is stronger. Since the dimensions of present nanorods are so large compared to the exciton Bohr radius of ZnO, any contribution from confinement effects can be ruled out[36–39].

3.4 Conclusions

Using three terminal electrodeposition process, ZnO nanorods were grown over 4 different TCO substrates. The dependence of ZnO seed layer on the formation of ZnO nanorods was also investigated. The nanorods showed crystalline wurtzite structure. Depending on growth conditions, most samples showed preferred orientation in (0 0 0 2) direction, which was calculated using texture coefficient. Density of nanorods over a substrate increases with seed layer thickness, while nanorod height and width decreases. For nanorod growth over a surface with large lattice mismatch, the preferred orientation of nanorods depends on surface rough-

ness. In such cases as surface roughness increases the preferred orientation decreases. The nanorod growth over a surface with low lattice mismatch showed highly preferred oriented growth of nanorods even if the surface roughness is high. After post deposition annealing samples showed above 80% transparency in visible-IR region. Photoluminescence studies showed a sharp NBE and broad DLE emission. The DLE emission suppresses on annealing. Raman studies also confirm the formation of wurtzite ZnO nanorod formation.

3.5 References

[1] X. Ma, H. Zhang, Y. Ji, J. Xu, D. Yang, Mater. Lett. 59 (2005) 3393.

[2] P.M. Aneesh, M.K. Jayaraj, Bull. Mater. Sci. 33 (2010) 227.

[3] S. Xu, Z.L. Wang, Nano Res. 4 (2011) 1013.

[4] J.B. Cui, U.J. Gibson, Appl. Phys. Lett. 87 (2005) 133108.

[5] H. El Belghiti, T. Pauporté, D. Lincot, Phys. Status Solidi 205 (2008) 2360.

[6] F. Fang, H. Wang, A.B. Djurisic, A.M.C. Ng, W.K. Chan, Growth of ZnO nanostructures by electrodeposition, 3rd Int. Nanoelectron. Conf., IEEE, Hong Kong (2010) 539.

[7] L. Li, S. Pan, X. Dou, Y. Zhu, X. Huang, Y. Yang, J. Phys. Chem. C 111 (2007) 7288.

[8] Y. Tang, L. Luo, Z. Chen, Y. Jiang, B. Li, Z. Jia, L. Xu, Electrochem. Commun. 9 (2007) 289.

[9] D. Pradhan, K.T. Leung, J. Phys. Chem. C 112 (2008) 1357.

[10] C.Y. Jiang, X.W. Sun, G.Q. Lo, D.L. Kwong, J.X. Wang, Appl. Phys. Lett. 90 (2007) 263501 1.

[11] S. Dhara, P.K. Giri, Funct. Mater. Lett. 04 (2011) 25.

[12] J. Podzemský, W. Schade, Organic solar cells based on ZnO nanowires layer, EEIC, Germany (2006) 1.

[13] L. V. Podrezova, S. Porro, V. Cauda, M. Fontana, G. Cicero, Appl. Phys. A 113 (2013) 623.

[14] X. Zhang, X. Han, J. Su, Q. Zhang, Y. Gao, Appl. Phys. A 107 (2012) 255.

[15] Z.W. Liu, C.K. Ong, T. Yu, Z.X. Shen, Appl. Phys. Lett. 88 (2006) 1.

[16] R.S. Ajimsha, R. Manoj, P.M. Aneesh, M.K. Jayaraj, Curr. Appl. Phys. 10 (2010) 693.

[17] E. Przeździecka, K. Gościński, M. Stachowicz, D. Dobosz, E. Zielony, J.M. Sajkowski, M.A. Pietrzyk, E. Płaczek-Popko, A. Kozanecki, Sensors Actuators A Phys. 195 (2013) 27.

[18] L.L. Liew, H.Q. Le, G.K.L. Goh, Mater. Res. Innov. 15

(2011) 357.

[19] W. Wu, G. Hu, S. Cui, Y. Zhou, H. Wu, Cryst. Growth Des. 8 (2008) 4014.

[20] M. Izaki, T. Omi, Appl. Phys. Lett. 68 (1996) 2439.

[21] S. Yamabi, H. Imai, J. Mater. Chem. 12 (2002) 3773.

[22] A. Ghosh, Y.G. Gudage, R. Sharma, R.S. Mane, S.-H. Han, Sensors & Transducers 98 (2008) 1.

[23] T. Morita, S. Ueno, T. Tokunaga, E. Hosono, Y. Oaki, H. Imai, H. Matsuda, H. Zhou, M. Hagiwara, S. Fujihara, Cryst. Growth Des. 15 (2015) 3150.

[24] M. Lai, D.J. Riley, Chem. Mater. 18 (2006) 2233.

[25] Y. Li, G.W. Meng, L.D. Zhang, F. Phillipp, Appl. Phys. Lett. 76 (2000) 2011.

[26] S. Peulon, D. Lincot, Adv. Mater. 05 (1996) 166.

[27] L. Xu, Q. Chen, D. Xu, J. Phys. Chem. C 111 (2007) 11560.

[28] L. Xu, Y. Guo, Q. Liao, J. Zhang, D. Xu, J. Phys. Chem. B 109 (2005) 13519.

[29] L.S. Vikas, K.C. Sanal, M.K. Jayaraj, A. Antony, J. Puigdollers, Phys. Status Solidi A 211 (2014) 2493.

[30] X. Lu, D. Wang, G. Li, C. Su, D. Kuang, Y. Tong, J. Phys. Chem. C 2 (2009) 13574.

[31] J. Cui, U.J. Gibson, J. Phys. Chem. B 109 (2005) 22074.

[32] T. Damen, S. Porto, B. Tell, Phys. Rev. 142 (1966) 570.

[33] H. Zhu, J. Iqbal, H. Xu, D. Yu, J. Chem. Phys. 129 (2008) 124713.

[34] Y.W. Chen, Y.C. Liu, S.X. Lu, C.S. Xu, C.L. Shao, C. Wang, J.Y. Zhang, Y.M. Lu, D.Z. Shen, X.W. Fan, J. Chem. Phys. 123 (2005) 134701.

[35] K. Saravanan, B.K. Panigrahi, R. Krishnan, K.G.M. Nair, J. Appl. Phys. 113 (2013) 033512.

[36] V.A. Fonoberov, A.A. Balandin, 195410 (2004) 1.

[37] Y. Gu, I.L. Kuskovsky, M. Yin, S. O'Brien, G.F. Neumark, Appl. Phys. Lett. 85 (2004) 3833.

[38] V.A. Fonoberov, A.A. Balandin, Appl. Phys. Lett. 85 (2004) 5971.

[39] T. Makino, Y. Segawa, M. Kawasaki, H. Koinuma, Semicond. Sci. Technol. 78 (2004) 20.

Chapter 4

Vertically aligned ZnO nanorod array/CuO heterojunction and its UV detector application

4.1 Introduction

Majority of 1D ZnO nanostructure based devices utilize heterojunction structure. The inherently n-type ZnO is coupled with a suitable p-type conductor to obtain a p-n structure. Prior to nanorod based devices, thin film ZnO was used for fabricating p-n heterojunction devices. Fabrication of undoped[1] and doped[2,3] p-type ZnO nanorod is already reported in literature. Low stability and reproducibility of p-type ZnO in general limits the study on n-ZnO based p-n heterojunction devices. Recent studies used CuO[4–6], GaN[7,8], p-Si[9,10], NiO[11,12], etc. as p-type layer for fabricating p-n heterojunction using n-type 1D ZnO nanostructures.

In the solution growth of ZnO nanorods, seed layer expected to improve the nanorod growth over a substrate. Yet, the effects of seed layer on the electrical properties of these nanorod based devices were not well studied. In the previous chapter, the preferred oriented growth of ZnO nanorods over different substrate was investigated. Solution processed ZnO was reported to possess a large number of defect states. Detailed analysis on the electrical properties of the nanorods and the effect of seed layer on the electrical properties of the nanorods also were to be performed. Fabrication of a heterojunction using these nanorods and performing its characterization can effectively deduce more meaningful information.

4.2 Experimental

ZnO nanorods were grown over Al:ZnO (AZO) coated glass substrates by DC magnetron sputtering. The thickness of AZO over glass substrates (Corning 1737F) was 900 nm. In one set of samples, a seed layer of ZnO was deposited over AZO prior to electrodeposition of ZnO nanorods. The 5 nm thick ZnO seed layer was deposited by sputtering using a 2" powder compacted target. Prior to seed layer deposition, the substrates were ultrasonically cleaned with Acetone, Isopropyl alcohol, and water. 0.05 mM $ZnCl_2$ and 0.1 M KCl were dissolved in water to produce an aqueous solution electrolyte. The solution was taken in a special container and kept at 80 °C throughout the experiment. AZO coated glass plate was used as working electrode. Saturated calomel elec-

trode was used as reference electrode and Pt was used as the counter electrode. Throughout the experiment, the electrolyte was kept under constant stirring and oxygen was bubbled into the solution to make it saturate with oxygen. Zinc oxide nanorod array (ZNA) growth was initiated over the working electrode by applying -1.2 V at working electrode with respect to reference electrode using Biologic SP-300 potentiostat/galvanostat. After the deposition process, samples were washed well in water and dried in nitrogen. Post deposition annealing in air was performed on all the samples at 350 °C for 6 h. The electrodeposited ZNA constitutes the n-type layer of the device. On top of the ZNA a 70 nm thick p-type CuO layer was deposited by RF-magnetron reactive sputtering using metallic Cu target(99.99% pure)[13]. After attaining a base vacuum of $7x10^{-6}$ mbar, argon and oxygen gas was fed to the system at an oxygen partial pressure of 13.7%. The deposition was done at room temperature by giving 60 W sputtering power. Au metallic contact (60 nm) was selectively deposited over the CuO layer through a shadow mask by thermal evaporation technique. The fabricated final device had structure AZO/ZNA/CuO/Au, as shown in the schematic diagram, figure 4.1.

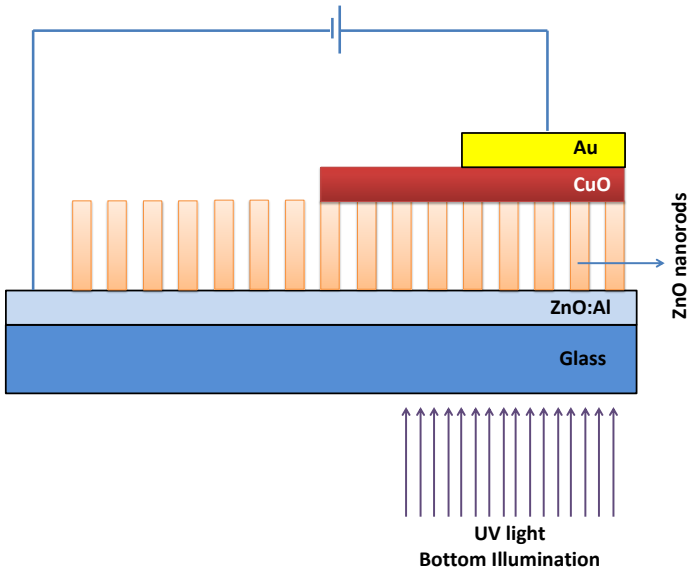

Figure 4.1: Schematic representation of ZNA heterojunction device.

The crystallinity of each layer was separately analysed using PANAlytical X'Pert PRO HRXRD. The morphological properties of as grown ZNA were studied in Carl Zeiss Ultra 55 field emission scanning electron microscope (FESEM). Raman spectrum and photoluminescence (PL) spectrum of ZNA were measured in Horiba Jobin Yvon LabRAM HR micro Raman spectrometer equipped with two laser sources. The 514.5 nm Ar^+ laser was used to record Raman spectrum, while PL was measured using 325 nm He-Cd laser as excitation source. Kiethley 4200 semiconductor analyzer along with SussMicroTec microprobe station was used for electrical characterization of the fabricated heterojunction. A Xe lamp along with a monochromator in Fluromax-3 spectrophotometer was used

to illuminate the heterojunction with selected wavelength, and corresponding electrical response was monitored using Biologic SP-300 potentiostat and galvanostat and the data was then used to plot, the photoresponse of the device. The sensor response to UV light was measured using a 11 W/m^2 UV lamp with its peak emission around 344 nm.

4.3 Results and Discussions

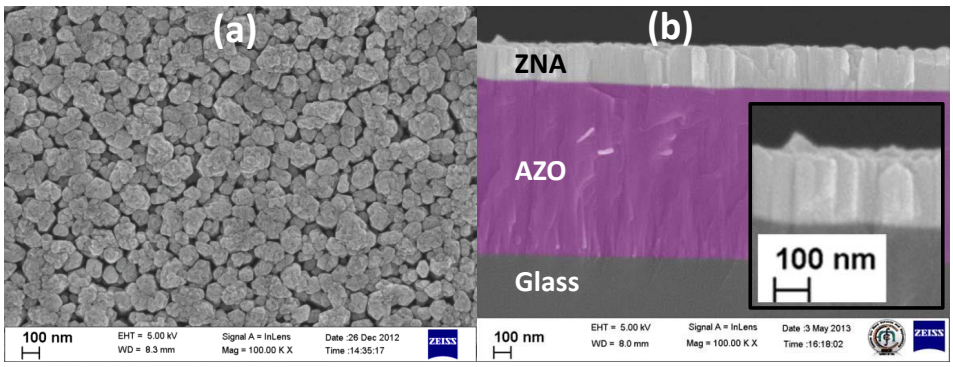

Figure 4.2: FESEM image of ZNA over AZO without seed layer, (a) top view, (b) cross sectional view and (inset of (b)) magnified cross sectional view of ZNA.

The FESEM images of zinc oxide nanorod array (ZNA) are shown in figure 4.2. The cross sectional view of the spectrum clearly confirms the growth of vertically aligned ZnO nanorods. From the inset of figure 4.2(b) the dimensions of ZNA are measured.

ZNA had an average diameter ≈100 nm and an average length of ≈220 nm.

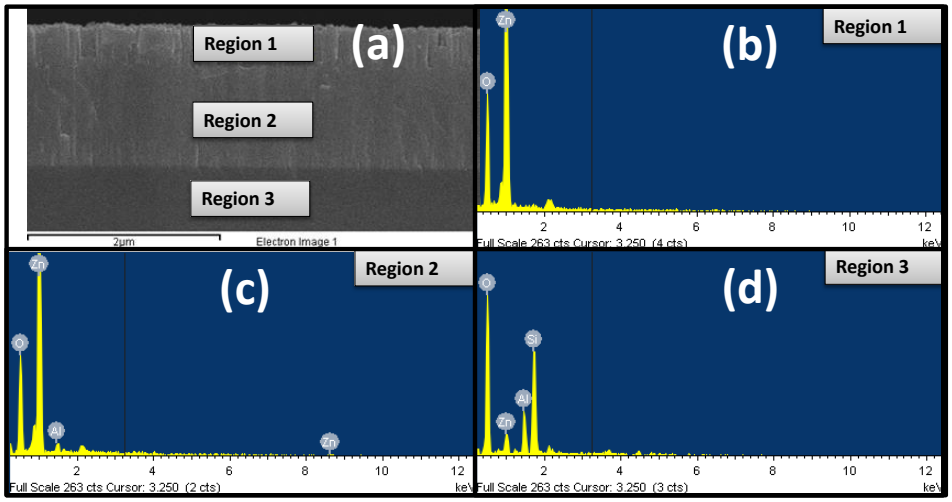

Figure 4.3: (a) The cross sectional SEM image of ZNA over AZO showing different regions, where EDAX is taken. The EDAX spectrum of (b) region I(ZNA), (c) region II(AZO) and (d) region III (glass).

A cross sectional SEM image of ZnO nanorod array grown over AZO coated glass plate and EDAX spectrum of three different regions of this sample were taken. The atomic percentage of elemental contributions in the analyzed region is tabulated in Table 1. In region I, the contributions from Zinc and Oxygen were seen with almost equal atomic percentage, indicating only the presence of ZnO. In region II, apart from Zn and O, presence of Al was also seen. The atomic percentage of Al is too low (2.81%) compared to

Zn and O, showing that region II is Al:ZnO. In region III, the contributions from Zn, O, Si and Al were seen. Here, the contributions from Si and O were higher and hence it could be concluded that region III is made of glass (silica)

Table 4.1: The atomic percentage of different elements obtained by EDAX analysis.

Elements	**Region I**	**Region II**	**Region III**
O	57.35	50.07	69.46
Zn	42.65	47.12	2.54
Al	--	2.81	6.58
Si	--	--	21.42

The X-ray diffraction (XRD) pattern of individual layers are shown in figure 4.4(a). ZnO XRD showed only two peaks. The peaks correspond to (0002) and (0004) crystal planes of hexagonal wurtzite crystal structure and match well with the ICSD 98-000-9341 reference data. ZNA showed a high texture coefficient for (0002) plane, indicating a highly preferred oriented growth along c-axis (as discussed in chapter 3). The XRD of CuO matches with polycrystalline monoclinic CuO (JCPDS 80-1916).

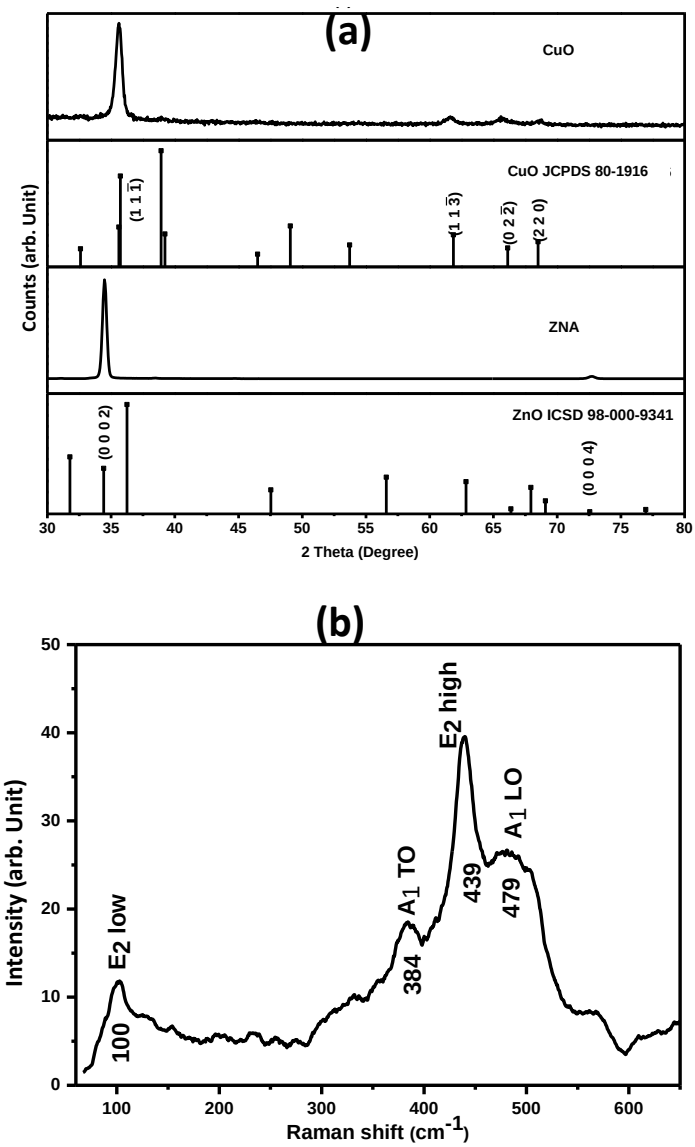

Figure 4.4: (a) The XRD pattern of ZNA and CuO layers. (b) Raman spectrum of ZNA.

ZNA Raman spectrum is shown in figure 4.4(b). Hexagonal wurtzite crystalline ZnO belongs to the C_{6v}^{4} space group. In the basic unit cell of ZnO, there are 4 atoms per unit cell with each ZnO occupying C_{3v} sites. Among the available phonon modes for this structure, six of them are optical as[14,15],

$$\Gamma_{\text{opt}} = 1A_1 + 2B_1 + 1E_1 + 2E_2 \qquad \text{--4.1}$$

While A_1 and E_1 modes are both Raman and infrared active, E_2 mode is only Raman active and B_1 mode is inactive silent mode. Raman spectrum of ZNA consists of 4 peaks at 100 cm^{-1}, 384 cm^{-1}, 439 cm^{-1} and 479 cm^{-1}. The observed Raman peaks matches with E_2(Low), A_1 transverse optical (A_1(TO)), E_2(High) and A_1 longitudinal optical (A_1(LO)) modes respectively, which again confirms that ZNA has wurtzite crystalline structure. In general, the A_1 and B_1 modes give information on displacement along the direction of c-axis, where as E_1 and E_2 modes give information about displacement perpendicular to the direction of c-axis. The A_1 and E_1 phonon modes signify the strength of polar lattice bonds. The transverse optical modes of A_1 and E_1 are formed by phonons polarized parallel and perpendicular to c-axis respectively. Thus the observed Raman peaks, especially the intense E_2(High) mode, confirm the c-axis oriented growth of ZnO nanorods in ZNA[16]. The presence of defects in ZNA may be a reason for observing slight broadening of A_1(LO) mode. The exciton Bohr radius of ZnO in bulk is ≈18Å, which is too low com-

pared to the dimensions of nanorods in ZNA[17]. Hence it can be confirmed that, the optical or electrical properties of ZnO will not depend on the confinement effects.

Both the samples showed very high transparency of about 90% in visible range as shown in figure 4.5(a). The band gap of ZNA with and without seed layer was calculated from the Tauc plot (figure 4.5(b)). It was found that both the samples had same band gap of 3.28 eV, which matches with previous reports. The optical band gap of CuO layer was determined as 1.4 eV.

Photoluminescence spectrum of both samples are shown in figure 4.5(c). The spectrum shows an emission peak at 385 nm and a broad emission in the range from 550 nm to 750 nm. The 385 nm emission matches with the near band edge emission (NBE) of ZnO. Various defects in the system can lead to the observed broad deep level emission (DLE) at 550 nm to 750 nm range. The DLE showed decrease in intensity for seed layered growth of ZNA. The relative intensity of DLE for ZNA without seed layer is 14.2% and that for ZNA with seed layer is 5.8%. Previous reports on ZnO PL suggest that the probability of oxygen vacancies (V_o) in ZnO samples are higher than those of zinc interstitials (Zn_i), because, V_o has lower formation energy compared to Zn_i. In Zn rich ZnO samples, V_o luminescent energy level is found at 0.9 eV above valance band maximum[18]. Whereas Zn_i can be observed at 0.22 eV below conduction band minimum. The oxygen interstitial defect level can

be observed at ≈2.28 eV below conduction band minimum. To get a detailed understanding on the defect emission, the DLE of ZNA over AZO without seed layer is resolved.

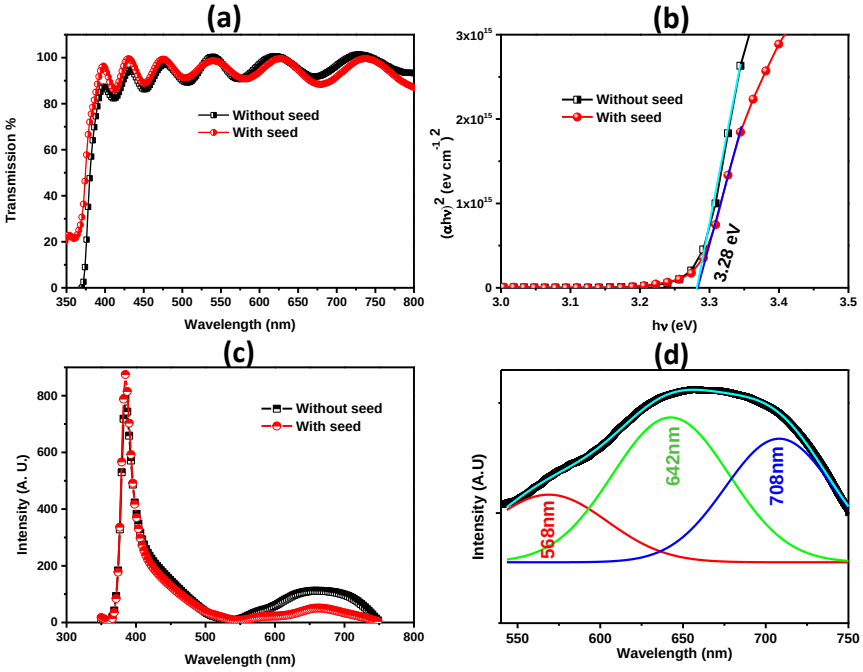

Figure 4.5: (a) The transmission spectrum of ZNA grown over AZO with and without seed layer. (b) The band gap variations of ZNA over AZO with and without seed layer. (c) The PL spectrum of ZNA. (d) The resolved DLE of ZNA over AZO without seed layer.

On resolving the DLE, three peaks were obtained at 568 nm, 642 nm and 708 nm as shown in figure 4.5(d). Comparing the energy levels, 568 nm emissions can be considered as electronic

transition from conduction band minimum or Zn_i to oxygen vacancy (V_o). Previous reports also suggest that emission at 642 nm can be observed due to transition from Zn_i to O_i[19,20]. According to Wang *et al.*, near infra-red emissions can be created due to the radiative recombination of shallowly trapped electrons with deeply trapped holes at O_i[21]. There are several reports on orange-red and NIR PL emissions due to various defect states in ZnO. Many reports are conflicting also, and hence it is hard to reach an agreement on the exact mechanism behind these emissions.

The electrical studies on CuO thin film shows a carrier mobility of 2.97 cm^2Vs^{-1} and a carrier concentration of 8.44 X 10^{17} cm^{-3}, which are typical values for p-type TCO thin films. After electrode deposition over the thin films, the fabricated heterojunction had a structure AZO/ZNA/CuO/Au, where AZO and Au served as contacts for the heterojunction. The V-I characteristics of the heterojunction is shown in 4.6.

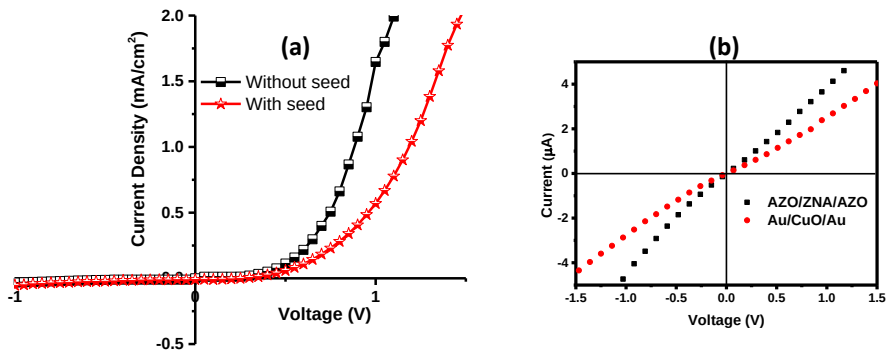

Figure 4.6: (a) The V-I characteristics of ZNA/CuO heterojunction. (b) The V-I characteristics of AZO/ZNA/AZO and Au/CuO/Au interface.

Both the heterojunctions showed rectifying behavior (figure 4.6(a)). The V-I characteristics of ZNA/AZO interface and CuO/Au interface showed ohmic behavior (figure 4.6(b)), which confirm that the heterojunction is formed between ZNA and CuO layers. Heterojunction formed by ZNA grown without seed layer offered a knee voltage of 0.65 V and a rectification ratio of 50 at 1 V. At the same time the heterojunction formed by ZNA grown over 5 nm seed layer offered a knee voltage of 0.9V and a rectification ratio of 17 at 1.25 V. The series resistance after turn on for heterojunction without seed layer is 17 kΩ and that for heterojunction with seed layer is 24 kΩ. Heterojunction without seed layer showed an ideality factor of 1.88 for lower voltages range (0 V - 0.25 V) and 6.77 for high voltage range (0.4 V – 1 V). Similarly, the ideality factors obtained for heterojunction with seed layer are 2.75 and 12 respectively. Thus the V-I characteristics of the two heterojunctions showed that seed layer is acting as a blocking layer for the flow of charge carriers. This may be a reason for the increase in series resistance obtained for seed layered heterojunction.

The higher ideality factor obtained for these heterojunctions also suggests the same idea. Since the heterojunction without seed layer showed better performance, compared to the heterojunction with seed layer, further studies were restricted to the heterojunction without seed layer only.

The dependence of junction capacitance with reverse biasing voltage will give us information about the quality of the junction. Figure 4.7(a) represents the $1/C^2$ vs V graph of heterojunction without seed layer. The capacitance variation of the heterojunction was measured for 1 MHz and 100 kHz frequencies. Under both frequencies the heterojunction followed a linear relationship of $1/C^2$ with V, but for lower reverse biasing voltages, a deviation from straight line behavior is evident. During the deposition of CuO layer over ZNA, diffusion of oxygen can occur across the interface resulting in the formation of thin intrinsic interface; hence the step junction assumption is not valid here. This may be a reason for the observed high ideality factor and deviation in $1/C^2$ vs V graph. From the variation of capacitance with voltage graph (figure 4.7(a)) the carrier concentration of lightly doped semiconductor has been calculated as 8.75 X $10^{14}cm^{-3}$ (at 1 MHz) and 15.3 X $10^{14}cm^{-3}$ (at 100 kHz).

Based on the inferences from the optical and electrical characterization of the heterojunction and individual semiconductor layers, a band structure of the heterojunction, formed by ZNA without seed layer, is proposed (figure 4.7(b)). In the figure, E_{g1} and E_{g2} represents the band gaps of CuO and ZnO semiconductors respectively. ΔE_c corresponds to knee voltage 0.65 (in eV) and ΔE_v is calculated from the equation $\Delta E_v = E_{g2} - E_{g1} + \Delta E_c$ as 2.33 eV. From the band diagram, since $\Delta E_c < \Delta E_v$, carriers can cross the junction with ease on UV excitation. The alignment of the bands

also suggests the possibility of constructing a detector with good UV response over visible light.

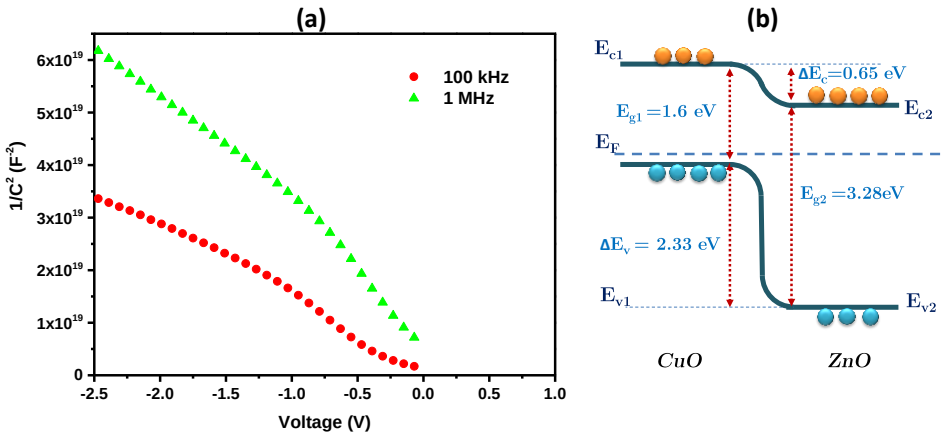

Figure 4.7: (a) The $1/C^2$ vs V graph of heterojunction without seed layer. (b) Band diagram of the heterojunction.

The response of the heterojunction detector to UV light is shown in figure 4.8(a). Increased junction current is observed on UV illumination. On UV illumination, absorption of UV light in the semiconductor causes electron to excite and reach conduction band. This may be a reason for the observed increase in junction current on UV illumination. The device is illuminated with UV light from Au electrode side (top illumination) and from the glass substrate (bottom illumination) side. The bottom illumination showed larger response than top illumination. On illumination from CuO side, absorption in CuO layer and reflection from Au layer reduces the number of available UV photons to be ab-

sorbed by the heterojunction. This may be the reason for the reduced response of the heterojunction, as observed in figure 4.8(a). On doing successive forward and reverse voltage sweep, a hysteresis like behavior is observed, as shown in figure 4.8(b). Observed hysteresis behavior is a clear indication of trap states in semiconductors. As trap states increases, the carrier life time decreases. On forward voltage sweep, the excited charge carriers get trapped in the available defect related trap states present in the sample. On reverse sweep, these trapped charge carriers can also contribute to the junction current, which may be the reason for increased response observed on reverse sweep. Previous reports suggest that hysteresis phenomenon will get less significant on UV illumination[22]. But, present heterojunction showed clear hysteresis behavior for both dark and UV excitation.

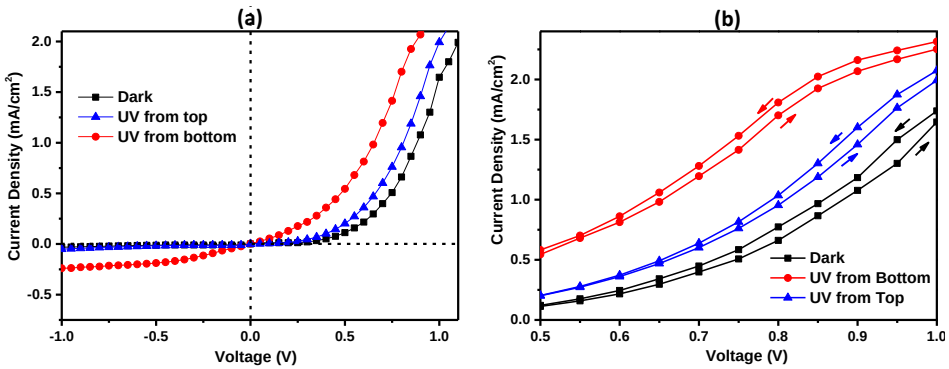

Figure 4.8: (a) Response of the heterojunction to UV illumination from top (from CuO side) and bottom (through glass substrate). (b) Hysteresis behavior observed in the forward bias region of V-I characteristics.

The heterojunction device was given a forward bias of 0.65 V (the knee voltage) and the detector response to UV light illumination ON and OFF states in regular interval was noted. The heterojunction current variation with time is plotted in figure 4.9(a). UV light ON OFF time was kept at ≈350 s throughout the experiment. For each UV light pulse, the obtained photoresponse data are asymmetric. The UV light was illuminated from the back side (glass substrate side) of the heterojunction device. On UV light turn OFF, the junction current in the device decayed exponentially. On UV light illumination, the device quickly reaches saturation level. But, on decay UV light OFF state, the device is taking longer time to come back to original state, which may be due to the presence of trap levels inside the heterojunction. Charge carriers take longer time to de-excite from trap states as carrier life time in trap states is higher. Hence, the longer decay time can be attributed to the carrier holding nature of trap states. The reproducibility and stability of the present device was checked and verified by repetitive UV measurements.

To quantitatively analyze the sensor's rise and decay processes, exponential curve fitting was employed. On analysis, the experimental data didn't fit well with single component exponential decay function, especially in UV light OFF region. But, a double component exponential decay function fitted well as shown in figure 4.9(b) and the equation is given below.

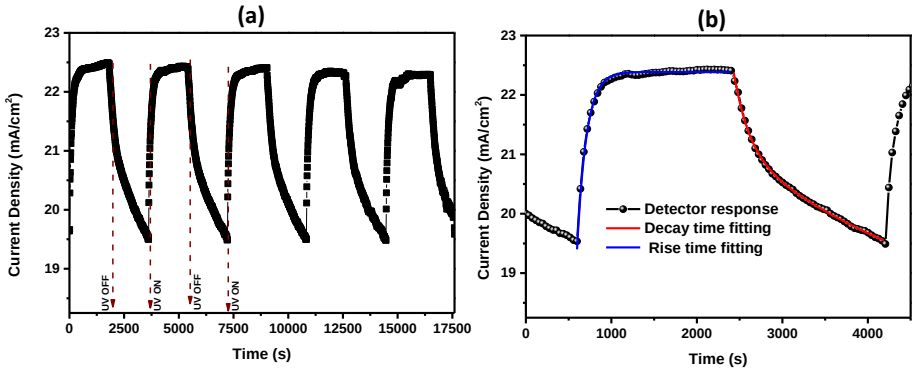

Figure 4.9: (a) Heterojunction response to UV light over time. (b) Rise and decay time of heterojunction detector fitted with exponential decay function.

$$J = J_0 + A_1 \exp\left(-\frac{t}{t_1}\right) + A_2 \exp\left(-\frac{t}{t_2}\right) \qquad \text{--4.3}$$

Where J and t represents the current density and time (in seconds) respectively. The fitted data gave two average life time for rise and decay regions. The time constants obtained from fitting are 68 s and 220 s where as for decay process they are 2986 s and 179s. The observation of two time constants suggests that there are two operative mechanisms each, for rise and decay regions. Also the time constant for decay process is too large compared to that for rise time, which explains why the heterojunction response seems asymmetric. For rising region, photo-generated carrier creation and carrier transport mechanisms may exist. The carrier generation by absorption process is usually faster. While charge carri-

ers transport through the semiconductor, it is confronted with grain boundaries and other material related defects. Hence the rise time constants can be attributed to the combined effects of photo generation and transport of charge carriers. On decay, as already mentioned, the presence of trap states may be the prime reason for observing larger time constants under decay process. Similar to rise process, in decay process also, the charge carriers are confronted with material defects and grain boundaries. Hence, the large value of decay time constants may be due to the combined effects trap states and material defects such as grain boundaries etc.

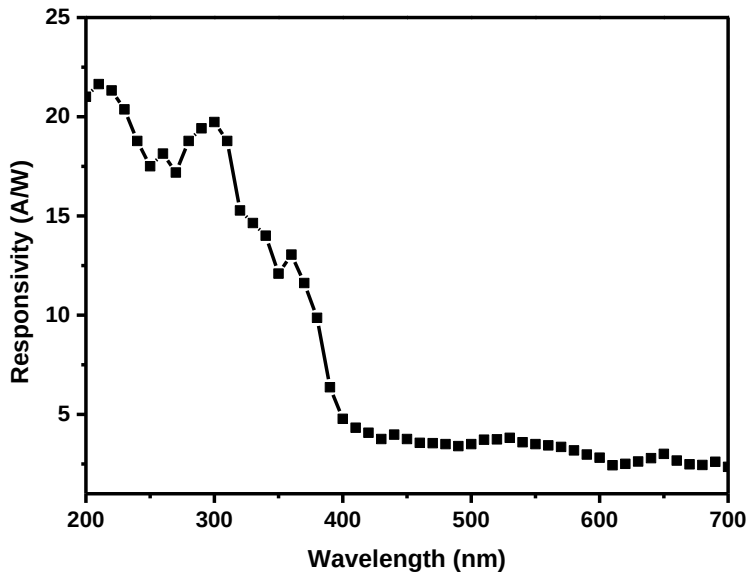

Figure 4.10: Responsivity curve of the heterojunction from 200 nm to 700 nm region.

The ability of a photodetector to selectively respond to a particular range of wavelengths can be explained by its responsivity. Throughout the analyzed spectral range, the present device showed better responsivity than previous reports. The device's responsivity showed low response to visible light and an increasing trend below 400 nm. The response is the highest in the UV region, which shows the selective response of the detector to UV light. The observed saturation behavior of the photo-detector for a specific input UV light can help in calibrating and deploying the present detector for practical applications. Though a constant level of junction current under dark condition has not been achieved, the junction current switched its levels for UV and dark states repeatedly, which demonstrated the reproducibility of the device. Layer by layer fabrication process will help in fabricating the device from an industrial point of view. During the fabrication process of present heterojunction photodetector, no intermediate seed layer or buffer layer was used for the growth of ZNA. In the present heterojunction photodetector design, the two ends of the heterojunction were well connected to electrodes, which helped easy charge transport to and from the heterojunction. All the above mentioned factors might have contributed together to obtain a better performing photodetector compared to previous reports. The device showed no sign of degradation in performance even after several months of exposure to atmospheric conditions. No special care or encapsulation methods were used during this period. The selective response to UV wavelength and its stable and rugged performance

may help the present device to serve practical application requirements.

4.4 Conclusions

Electrodeposition process was used to successfully grow highly oriented, crystalline and transparent ZnO nanorod array over Al:ZnO coated glass plate. Structural and morphological studies using FESEM and XRD confirmed vertical aligned c-axis preferred oriented growth of ZNA. Optical studies using Raman, PL and transmission spectrum showed various defect states related to Zn_i, O_i and V_o. Transparent growth of ZNA looks promising even for transparent electronic applications.

The AZO/ZNA/CuO/Au heterojunction showed rectifying behavior. The V-I characteristics suggests that the use of seed layer is deteriorating the heterojunction performance with an added series resistance and increased knee voltage. The heterojunction showed good response to UV light. The responsivity studies of the detector showed selective response to UV light over visible light. Photoresponse measurements over time showed an asymmetric rise-fall behavior. Mathematical fitting of the actual response data suggested faster rise mechanism and defect assisted semiconductor trap related defect assisted slower decay mechanism.

Present device showed stable and reproducible detector response even after few months of exposure to atmospheric condi-

tions. The industry friendly layer by layer growth approach of device fabrication is extremely useful for practical deployment. The device showed highly selective response to UV light compared to visible light. The responsivity values are higher compared to previous reports. Though the response time of the present device is too slow, the reproducible and highly stable UV saturation level observed is extremely useful in areas where constant UV monitoring is necessary. The visible light rejection property is extremely helpful, as these devices can be used in day light without any mask or filter.

4.5 References

[1] J. Luo, C.C. Ling, B. Yuk, F. Hsu, Y.Y. Xi, K.H. Tam, A.B. Djuris, C.K. Cheung, A. Man, C. Ng, W.K. Chan, X. Deng, C.D. Beling, S. Fung, K.W. Cheah, P. Wai, K. Fong, C.C. Surya, Adv. Funct. Mater. 18 (2008) 1020.

[2] B. Xiang, P. Wang, X. Zhang, S.A. Dayeh, D.P.R. Aplin, C. Soci, D. Yu, D. Wang, Nano Lett. 7 (2006) 323.

[3] G.D. Yuan, W.J. Zhang, J.S. Jie, X. Fan, J.A. Zapien, Y.H. Leung, L.B. Luo, P.F. Wang, C.S. Lee, S.T. Lee, Nano Lett. 8 (2008) 2591.

[4] L.S. Vikas, K.C. Sanal, M.K. Jayaraj, A. Antony, J. Puigdollers, Phys. Status Solidi A 211 (2014) 2493.

[5] H. Wei, H. Gong, Y. Wang, X. Hu, L. Chen, H. Xu, P. Liu,

B. Cao, CrystEngComm 13 (2011) 6065.

[6] J.K. Wu, W.J. Chen, Y.H. Chang, Y.F. Chen, D.R. Hang, C. Liang, J.Y. Lu, Nanoscale Res. Lett. 8 (2013) 387.

[7] Q. Yang, W. Wang, S. Xu, Z.L. Wang, Nano Lett. 11 (2011) 4012.

[8] J.H. Wu, S.Y. Liu, S. Li, Y. long Jiang, G.P. Ru, X.P. Qu, Appl. Phys. A 109 (2012) 489.

[9] J. Bao, M. a Zimmler, F. Capasso, X. Wang, Z.F. Ren, Nano Lett. 6 (2006) 1719.

[10] Y. He, J. Wang, W. Zhang, X. Chen, Z. Huang, Q. Gu, J. Phys. Conf. Ser. 152 (2009) 012054.

[11] J.Y. Wang, C.Y. Lee, Y.T. Chen, C.T. Chen, Y.L. Chen, C.F. Lin, Y.F. Chen, Appl. Phys. Lett. 95 (2009) 131117.

[12] Y.Y. Xi, Y.F. Hsu, A.B. Djurišić, A.M.C. Ng, W.K. Chan, H.L. Tam, K.W. Cheah, Appl. Phys. Lett. 92 (2008) 113505.

[13] K.C. Sanal, L.S. Vikas, M.K. Jayaraj, Appl. Surf. Sci. 297 (2014) 153.

[14] H. Morkoç, Ü. Özgür, Zinc Oxide: Fundamentals, Materials and Device Technology, WILEY-VCH, Darmstadt (2008).

[15] T. Damen, S. Porto, B. Tell, Phys. Rev. 142 (1966) 570.

[16] H. Zhu, J. Iqbal, H. Xu, D. Yu, J. Chem. Phys. 129 (2008) 124713.

[17] S. Hong, T. Joo, W. Il Park, Y.H. Jun, G.C. Yi, Appl. Phys. Lett. 83 (2003) 4157.

[18] P.A. Rodnyi, I. V. Khodyuk, Opt. Spectrosc. 111 (2011) 776.

[19] C.H. Ahn, Y.Y. Kim, D.C. Kim, S.K. Mohanta, H.K. Cho, J. Appl. Phys. 105 (2009) 013502.

[20] M. Gomi, N. Oohira, K. Ozaki, M. Koyano, Jpn. J. Appl. Phys. 42 (2003) 481.

[21] M. Wang, Y. Zhou, Y. Zhang, E. Jung Kim, S. Hong Hahn, S. Gie Seong, Appl. Phys. Lett. 100 (2012) 101906.

[22] S. Wang, C. Hsiao, S. Chang, S. Member, Z.Y. Jiao, S. Young, IEEE Trans. Nanotechnol. 12 (2013) 263.

Chapter 5

Growth and characterization of vertically aligned ZnO nanorods over GaN:Mg substrate

5.1 Introduction

The substrate used for the growth of a thin layer has a direct influence on the properties of the grown layer. Hence, in order to grow a material over a substrate, proper knowledge about the substrate and its surface is necessary. If the substrate and layer has large lattice mismatch, the stress experienced at the substrate-layer interface will be large. These strain related defects alter its optoelectric properties also. Hence in the present study, in order to grow a ZnO layer with minimal defects and with good interface, the chosen substrate should possess a lattice parameter very close to ZnO.

GaN is a suitable choice, as the lattice mismatch between ZnO and GaN is too small. Moreover, stable p-type conductivity can be easily induced by doping with suitable metals. This property is a boon especially when a ZnO based p-n heterojunction is fabricated.

In the previous study, ZnO nanorods were grown by electrodeposition process. Electrodeposition requires a conducting substrate for nanorod growth. Since nanorod growth by electrodeposition is difficult over non-conducting substrates, alternate techniques are needed. A number of techniques like MBE[1], CVD[2,3], MOCVD, hydrothermal synthesis[4,5], electrodeposition[5–7] etc. are already reported, for the growth of ZnO nanorods over GaN substrate. Studies by Lupan et al. revealed that ZnO nanorods grown by hydrothermal synthesis offers better device performance compared to nanorods grown by electrodeposition[5]. Hydrothermal synthesis is a low cost technique with high yield. Present studies suggests the growth of highly crystalline ZnO by hydrothermal technique under suitable conditions. The crystalline quality of nanorods grown by this technique, matches with those samples grown by expensive and sophisticated techniques such as MOCVD, MBE, etc.

Low temperature solution growth of nanorods over a substrate usually requires seed layer.[8] Recent studies on ZnO nanorod based perovskite solar cells suggest that seed layer and growth

plays a crucial role on the final performance of the nanorods. By tuning the seed layer deposition conditions and surface modification of ZnO nanorod over FTO substrate, the photo conversion efficiency (PCE) was increased to 14%[9]. Hence, the present study also investigate the effect of seed layer on the growth of ZnO over GaN substrate.

In this chapter, we report the growth of ZnO nanorods over GaN:Mg substrate. The substrate has c-axis orientation. ZnO nanorods are grown by hydrothermal synthesis. The effect of seed layer on the orientation of ZnO nanorods and its crystallinity is studied in detail. The crystallinity is evaluated using X-ray diffraction studies.

5.2 Experimental

C-plane cut GaN:Mg substrate purchased from MTI corporations was used for the growth of ZnO nanorods. The substrate had an internal structure Al_2O_3/GaN:nid/GaN:Mg. The c-plane prime grade two side polished 2" Al_2O_3 substrate has a thickness of 350 μm. On top of that 1.5 μm non-intentionally doped (nid) buffer GaN layer is grown and above the buffer layer, a 2 μm thick Mg doped GaN layer was grown. MTI Corporation used MOCVD technique to grow both GaN layers. Prior to use all GaN substrates are cleaned in a 3 step ultra-sonication process using isopropyl alcohol, ethanol and distilled water and later dried in flow of nitrogen.

In some samples seed layer is deposited before hydrothermal synthesis. The seed layer was prepared by a dip coating process. 25 mM $Zn(CH_3COO)_2$ and 0.05 M NaOH are dissolved in ethanol and stirred for 1 hour. The cleaned GaN substrates are dipped in this solution and kept it there for 5 minutes and then dried in a hot plate. This process was repeated for a few number of times to get uniform seed layer. Annealing the dip coated substrate at 100 °C for 1 hour gives ZnO islands with (0002) plane parallel to the substrate surface. Since dip coating technique is used, seed layer will be formed on both faces of the substrate.

Vertical growth of ZnO nanorods over the substrate was achieved by hydrothermal synthesis. 0.1 M zinc acetate solution in water was prepared and NH_4OH solution was added to the $Zn(CH_3COO)_2$ solution to obtain pH above 9. The solution was stirred for 30 minutes and was taken into a Teflon lined autoclave. Cleaned substrate is kept horizontally inside the solution in the autoclave. The autoclave is later kept at a temperature of 180 °C for 1 hour under indigenously developed pressure. After the specific time it was allowed to cool to room temperature naturally. The substrate is then taken out and cleaned in distilled water and then dried in N_2. After hydrothermal synthesis one sample from each set is taken and post deposition annealing is performed at 350 °C for 6 hour.

Based on the experimental conditions, four different types of samples were fabricated. The details of sample name and specific descriptions are given in table 5.1.

Table 5.1. List of sample name and its details.

Sample name	**Details**
GZn	ZnO nanorods grown over GaN:Mg substrate, without seed layer and without post deposition annealing
GZnA	ZnO nanorods grown over GaN:Mg substrate without seed layer and with post deposition annealing
GZnS	ZnO nanorods grown over GaN:Mg substrate with seed layer and without post deposition annealing
GZnSA	ZnO nanorods grown over GaN:Mg substrate with seed layer and with post deposition annealing

The morphology of ZnO nanorods were studied in Raith 150 field emission scanning electron microscope (FESEM). The X-ray studies were conducted in PANalytical XPert Pro MRD HRXRD. High resolution X-ray studies, rocking curve, pole figure analysis and reciprocal space mapping (RSM) are performed to get a deep understanding of the crystallinity of the samples. Horiba Jobin Yvon Labram HR Micro Raman spectrometer is used for measur-

ing the Raman spectrum and photoluminescence (PL) spectrum of the samples. 514.5 nm Ar^+ laser is used for Raman studies, while 325 nm He-Cd laser from Melles Griot is used for PL studies. Transmission spectrum is measured in Jasco V570 UV-VIS-NIR spectrophotometer.

5.3 Results and Discussions

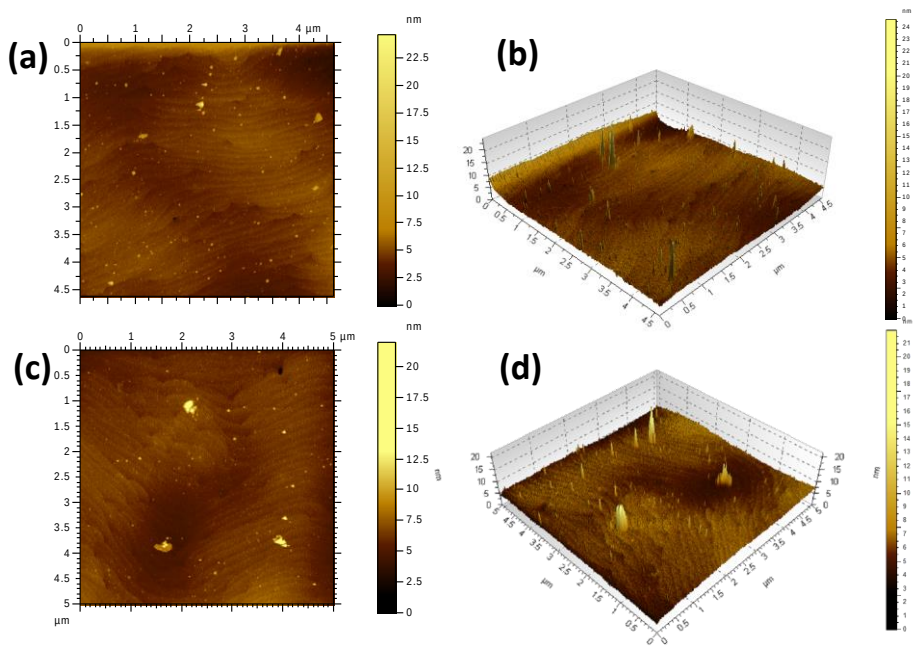

Figure 5.1: The AFM image of GaN:Mg substrate before etching in KOH (a) 2D view & (b) 3D view and after etching in KOH (c) 2D view & (d) 3D view.

During the growth of GaN, the terminating element influence its electrical properties, which is critical for device applications. There are several techniques to determine the terminating element in GaN. Reflection high energy electron diffraction (RHEED) is a powerful technique to determine the structure of such materials[10]. Etching experiment is rather simple yet, powerful tool, which also gives similar idea. GaN films showed selective etching to KOH solution in <0001> direction. A 10% KOH etches the surface and makes the surface rougher if there is N termination. If there is Ga termination, there won't be any chemical etching [11]. The etch rate study showed that most of the etching occur within 10 minutes[12]. Hence, to study the termination element of current sample, an etching experiment was conducted on GaN:Mg substrate using 10% KOH solution in water for 10 minutes. AFM analysis was performed before and after etching. Figure 5.1 (a) and (b) reprecents the 2D and 3D view of AFM images for GaN substrate, while Figure 5.1 (c) and (d) represents 2D and 3D views of AFM images for GaN substrate after etching. AFM analysis confirmed smooth substrate surface with rms roughness of ~0.9 nm. Several grains of few nm are also seen on the substrate. There is not much difference between the surface topographies before and after etching, as obtained from AFM, which confirms no significant etching was taken place. This revealed that the surface is terminated with Ga atom which is resistant to KOH etching. Observation of smooth substrate surface

without point defects can help to achieve uniform growth of material over the substrate. The uniform growth of GaN layer with surface Ga ions without point defects is suitable for achieving defect free interface for device applications.

FESEM images of nanorods are shown in figure 5.2. The analysis confirms the formation of vertically aligned ZnO nanorods. Hexagonal faces of nanorods as seen in the images are typical characteristic of wurtzite crystalline nature of ZnO. For samples grown with seed layer, the nanorods had a diameter of ~200 nm and a length of ~940 nm. While for samples grown on seed layer, the nanorod diameter was ~135 nm and length was ~2100nm. The nanorods over seed layered samples are longer but with lower diameter. It is also clear that the packing density of nanorods is more for seed layered samples.

Nanorods are grown over the entire substrate uniformly for samples grown without any seed layer (GZn and GZnA). While taking lower magnification FESEM images, a non-uniform growth of nanorods were observed for samples grown on ZnO seed layered samples (GZnS & GZnSA). Patches of ZnO nanorods observed were not covering the entire substrate, as shown in figure 5.3(a). Several flower like structures were also observed in these samples. It is also observed that the vertical nature of nanorods is more prominent for samples grown without seed layer, while for rods

grown with seed layer, the nanorods are grown slightly tilted from its vertical axis.

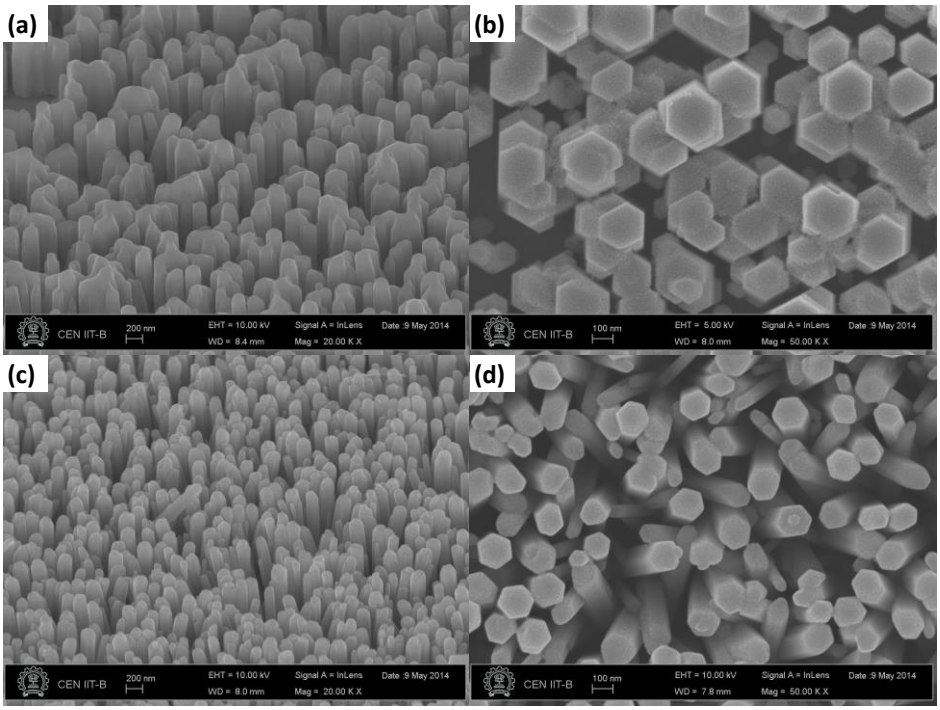

Figure 5.2: The FESEM images of ZnO nanorods over GaN:Mg substrate without seed layer, (a) 45° tilted view and (b) top view, and with seed layer (c) 45° tilted view and (d) top view.

In the case of solution growth of nanorods, it is already reported that seed layered growth improves the nanorod growth[4,13]. Contrary to this, we observed that ZnO nanorods

had poor vertical orientation on samples, where nanorods are grown on substrate with seed layer. We observed that seed layer formation was not uniform. The seed layer, grown by solution process, had cluster formation over the substrate. These patches of seed layer may be a reason for poor vertical growth of ZnO nanorods. During the initial stages of nanorod growth, ZnO seed particles created, acts as nucleation centers and nanorods started to grow from these nucleation sites. In certain situations more than one nanorod starts to grow from a single nucleation site. As number of nanorods starts to grow from a single nucleation site, the nanorods span around the upper hemisphere of the spherical seed particle by keeping the nucleation site (seed) as origin. This kind of growth results in the growth of various structures like nanoflowers.

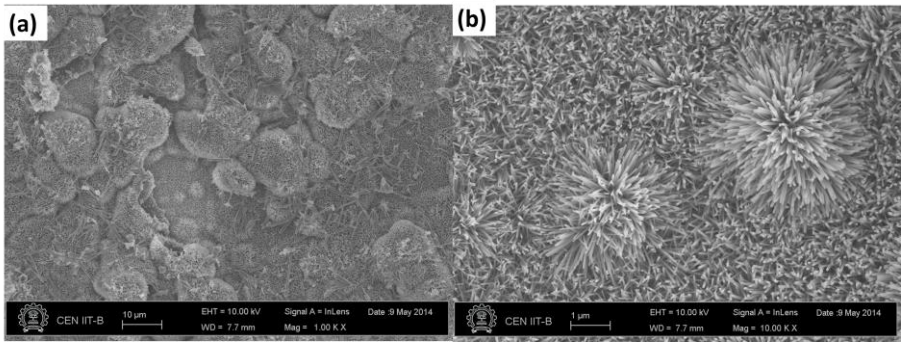

Figure 5.3: Low magnification FESEM images of seed layered growth of ZnO nanorods showing (a) non-uniform growth and (b) flower like structures.

Compared to non-seed layered substrates, the seed layered substrates will offer more nucleation sites for the growth of nanorods, and hence seed layered substrates will get packed with a number of nanorods, i.e., the density increases. At the same time, increased density of nanorods will offer resistance to enlargement of nanorods along its diameter, which again results in thinner nanorods.

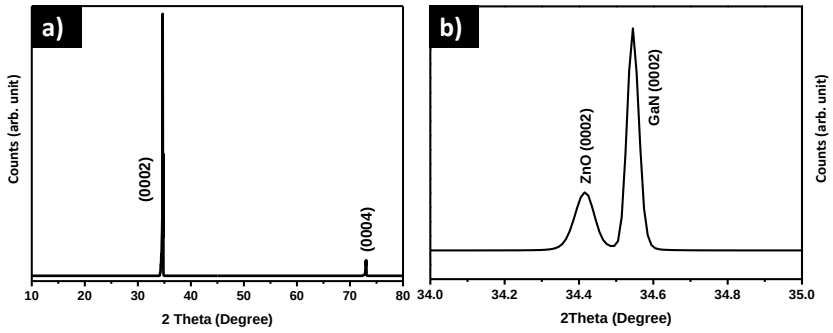

Figure 5.4: (a) The phase analysis spectrum of ZnO nanorods grown over GaN:Mg substrate. (b) Rocking curve of (0002) crystal planes of ZnO and GaN

The phase analysis of ZnO nanorods grown over GaN:Mg substrate is as shown in figure 5.4(a). Only two peaks were seen which corresponds to (0002) and (0004) planes. High resolution rocking curve X-ray diffraction studies were performed at reflections from (0002) planes and the single peak was resolved into two peaks as shown in figure 5.4(b). The two peaks correspond to

(0002) crystal reflections from ZnO and GaN. Since the crystal structure of both ZnO and GaN are the same and the lattice parameters are so close, the (0002) crystal reflections are also observed very close.

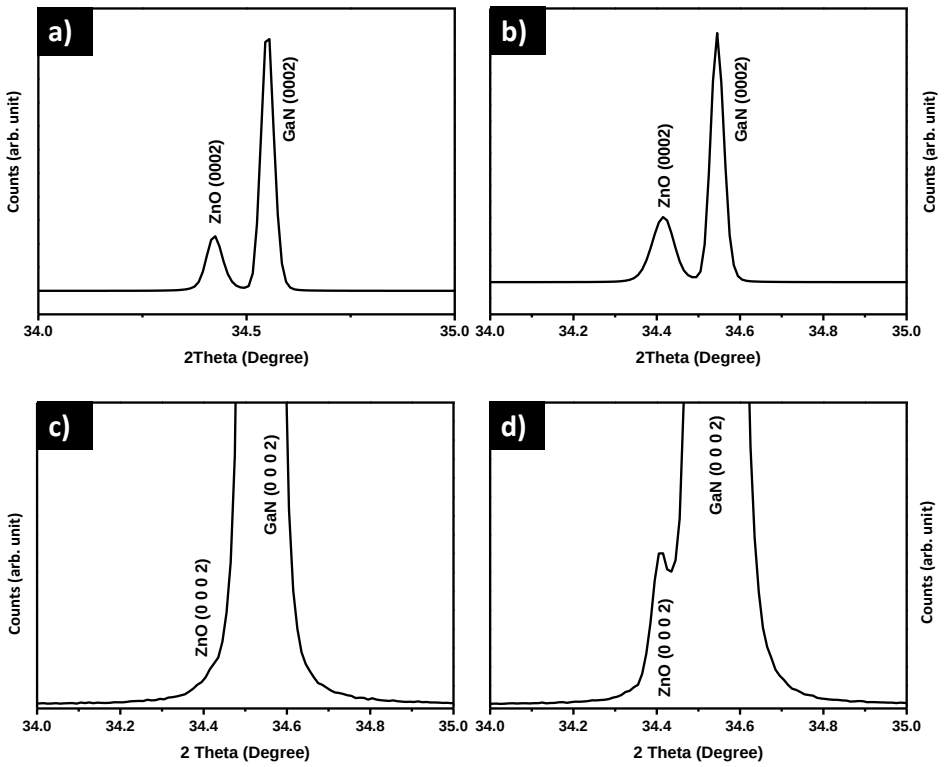

Figure 5.5: The rocking curve analysis of reflections from (0002) planes of (a) GZn, (b) GZnA, (c) GZnS and (d) GZnSA. ('A' stands for annealed, 'S' stands for seed layer).

Rocking curve analysis of all the samples are shown in figure 5.5. reflections from (0002) planes of ZnO and GaN were able to resolve for GZn, GZnA and GZnSA as shown in figure 5.5(a), (b) and (d). No extra reflections due to ZnO are observed for GZnS (figure 5.5(c)). The relative intensity of ZnO (0002) peak w.r.t. GaN (0002) peak, increased from 21.9% (for GZn) to 26.1% (for GZnA) on annealing. The peak intensity of GaN (0002) peak is found to be decreasing on annealed sample which can be attributed to the improved ZnO crystallinity on annealing. Comparing all the results from high resolution rocking curve analysis, annealed samples showed improved crystallinity, which is clear from the increase in diffracted X-ray intensity from ZnO planes.

Just like the reflections from (0002) planes of ZnO and GaN were resolved, contributions from $(10\bar{1}2)$ planes can also be resolved on HRXRD rocking curve analysis as shown in figure 5.6(a). The $(10\bar{1}2)$ reflections are obtained at ~43° Psi angle. On detailed Phi analysis at the Omega, 2θ and Psi angles, six peaks were obtained with equal separation between them. These peaks corresponds to the reflections from the family of planes $< 10\bar{1}2 >$. All observed X-ray diffraction peaks were able to resolve into contributions from ZnO and GaN, which shows that ZnO nanorods have good hexagonal wurtzite crystallinity just like the GaN layer. Similar results were obtained for ZnO nanorods grown over GaN substrate by MOCVD, showing the epitaxial growth of ZnO nanorods[14].

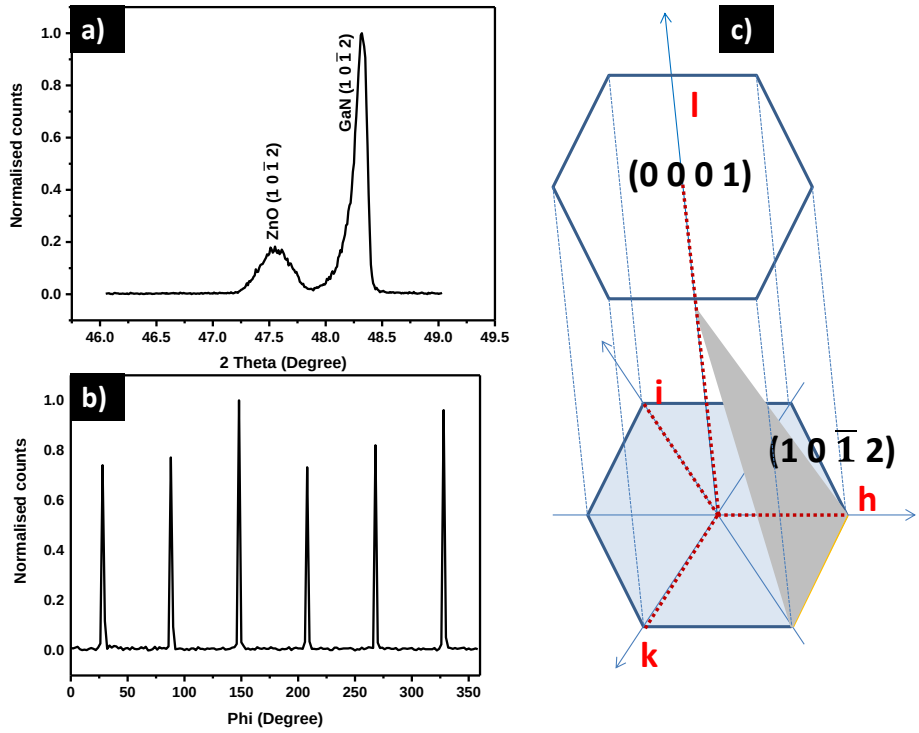

Figure 5.6: (a) Rocking curve of $(10\bar{1}2)$ plane of ZnO nanorods and GaN:Mg. (b) Single phi scan of $(10\bar{1}2)$ plane at a particular psi angle. (c) Schematic representation of crystal planes in hexagonal crystal structure.

Further, to understand the distribution of crystal planes over the samples, pole figure analysis for $< 0002 >$ and $< 10\bar{1}2 >$ planes were performed as shown in figure 5.7. Since ZnO and GaN peaks were unable to be resolved for GZnS, no pole figure analysis was performed on GZnS. The schematic diagram shown in figure 5.6(c) gives an idea about various planes in hexag-

onal crystal structure. The pole figures of GZn, GZnA and GZnSA showed single center spots as shown in figure 5.7(a), (c) and (e) respectively. The (0002) and $(000\bar{2})$ together contribute family of planes {0002}. ZnO nanorods were grown over (0002) oriented GaN substrate. Hence, on alignment, the $< 0002 >$ direction will point perpendicular to the substrate. Since both (0002) and $(000\bar{2})$ are parallel planes, only one spot should be observed in the pole figure analysis. Again, as the (0002) plane is parallel to the sample surface the observed single spot will be at Psi=0, i.e. at the center of the pole figure. At the same time $< 10\bar{1}2 >$ pole figure analysis showed six peaks for all the samples. The planes $(10\bar{1}2)$, $(1\bar{1}02)$, $(0\bar{1}12)$, $(\bar{1}012)$, $(\bar{1}102)$, $(01\bar{1}2)$ and their respective inversion planes $(\bar{1}01\bar{2})$, $(\bar{1}10\bar{2})$, $(01\bar{1}\bar{2})$, $(10\bar{1}\bar{2})$, $(1\bar{1}0\bar{2})$, $(0\bar{1}1\bar{2})$ together constitute the set of family planes of $\{10\bar{1}2\}$. Each plane and its corresponding mirror plane are a set of parallel planes. Hence, each set of parallel planes end up in contributing to each spot in the pole figure analysis. Thus observation of 6 independent spots in the pole figure spectrum is an indication of good crystallinity of as grown ZnO nanorods. The changes in intensity of the peaks from sample to sample match with the findings of rocking curve analysis. The annealed sample (GZnA) shows increased intensity compared to the as prepared sample (GZn). Also, the intensity of GZnSA was too weak compared to that of GZnA. These changes are closely related to the crystalline quality of these samples. A variation in intensity distribution among the six peaks of

the same sample is also visible. This can be caused by two reasons, (i) because of poor crystallinity or, (ii) because of the variations in sample dimensions. Since the dimensions in the samples under consideration are not ideal, the number of crystal planes in each direction will be different, and hence the number of photons reflected from each set of planes will also be different. The major contributor for the change in intensity of $< 10\bar{1}2 >$ peaks in the present samples can be attributed to the changes in sample dimensions.

Pole figure analysis of GaN:Mg substrate also showed an intense spot at the center for $< 0002 >$ planes (figure 5.7(g)). The $< 10\bar{1}2 >$ pole figure showed six intense spots with equal separation (figure 5.7(h)), showing the excellent crystalline nature of GaN:Mg substrate, used for the current study, which is consistent with previous results[15].

It is also interesting to note that the end faces of the nanorods over the entire substrate is in an ordered state with the hexagonal end faces parallel as shown in figure 5.8. That is, the (1000) planes of all the rods are parallel to each other, so is the other family of planes. This emphases the highly aligned growth of ZnO over the GaN:Mg substrate. This is the reason for the observed typical Phi scan as shown in figure 5.6 (b). Similar result has been observed for ZnO nanorod growth over GaN substrate via electrodepositoion[16]. These results suggest that on macroscopic

scale all the nanorods follow the same crystal orientation of GaN substrate.

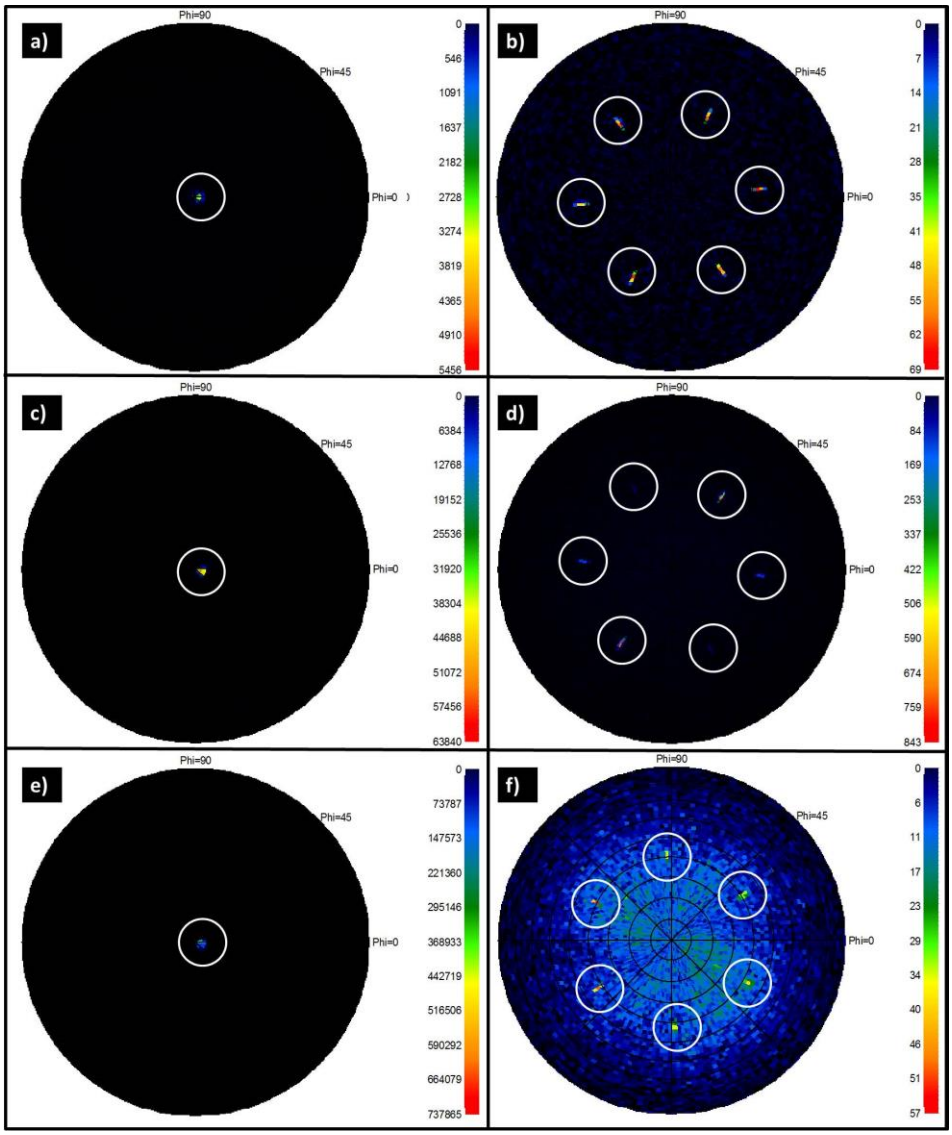

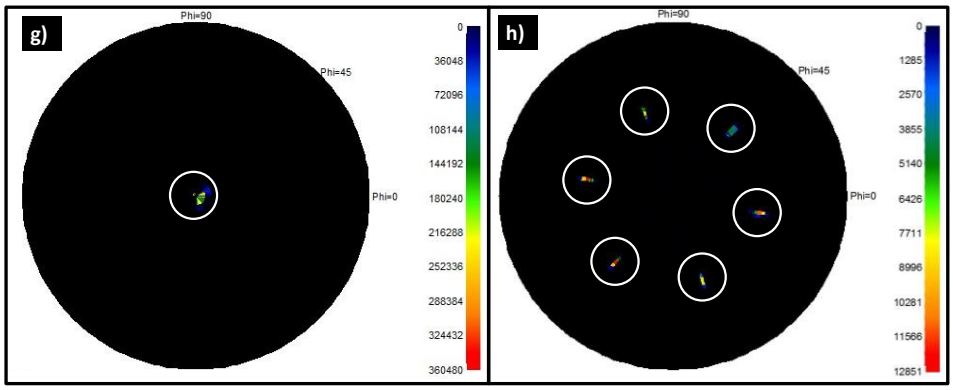

Figure 5.7: The $< 0002 >$ pole figure analysis images of (a) GZn, (c) GZnA, (e) GZnSA (g) GaN:Mg substrate and $< 10\bar{1}2 >$ pole figure analysis images of (b) GZn, (d) GZnA, (f) GZnSA and (h) GaN:Mg.

Both GZn and GZnA showed similar RSM pattern. Both has compact GaN peak showing good crystallinity of the substrate. ZnO also has almost the same peak width along Q_y axis, indicating almost similar d spacing values. While there is considerable widening of ZnO peak in Q_x axis compared to that of GaN. This indicates that the crystalline quality of ZnO (0002) peak is not as good as GaN, keeping in mind that the width is lesser than 1 degree. Comparing the RSM of as prepared and annealed samples (GZn and GZnA) we can see that the peak width along Q_x direction is lower for GZnA, indicating the crystalline quality slightly improved on annealing in air. The X-ray reflection from ZnO (0002) planes of GZnS and GZnSA were too weak to detect. Hence no significant features were obtained on RSM except that of GaN

for these samples. The only contribution from GaN (0002) observed on the corresponding RSM images are shown in Figure 5.8(c) and (d).

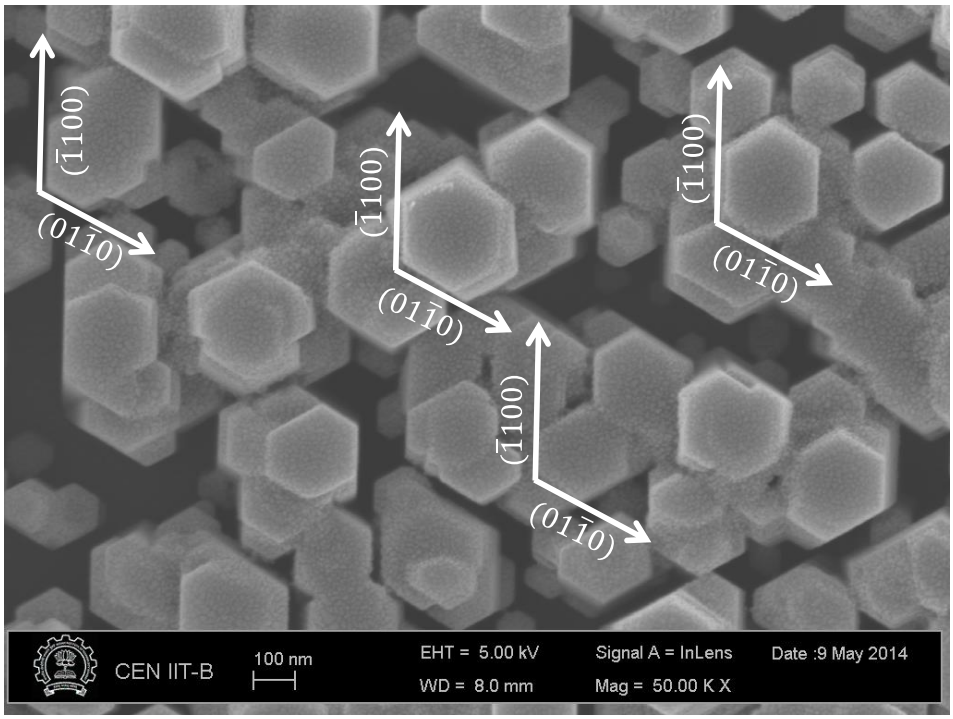

Figure 5.8: The FESEM images of ZnO nanorods (sample GZn) showing aligned hexagonal nanorod faces.

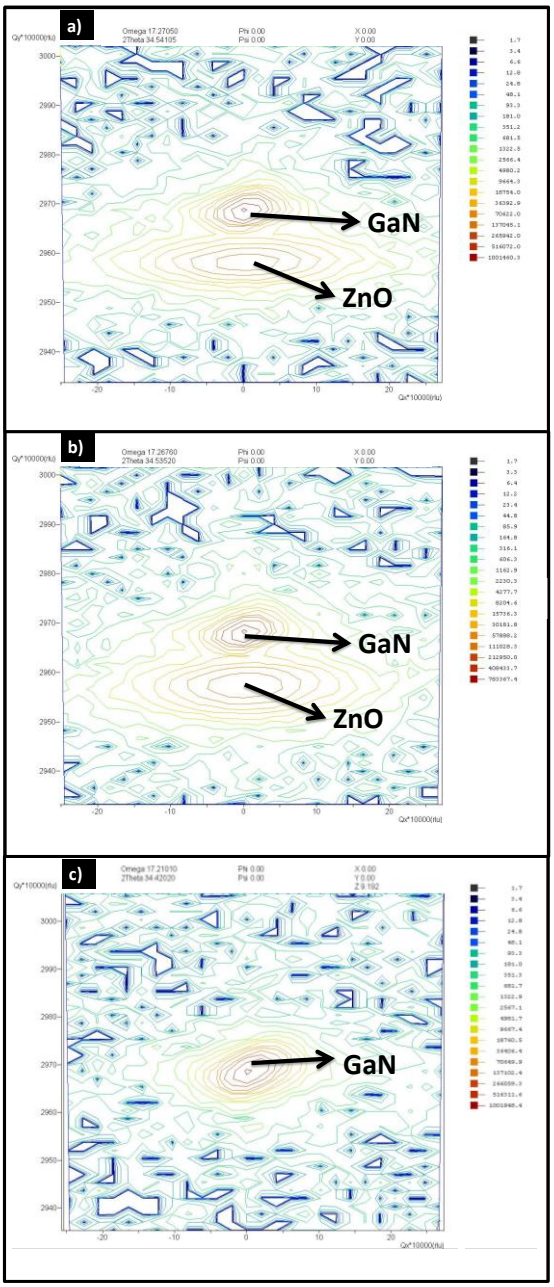
a)
GaN
ZnO
b)
GaN
ZnO
c)
GaN

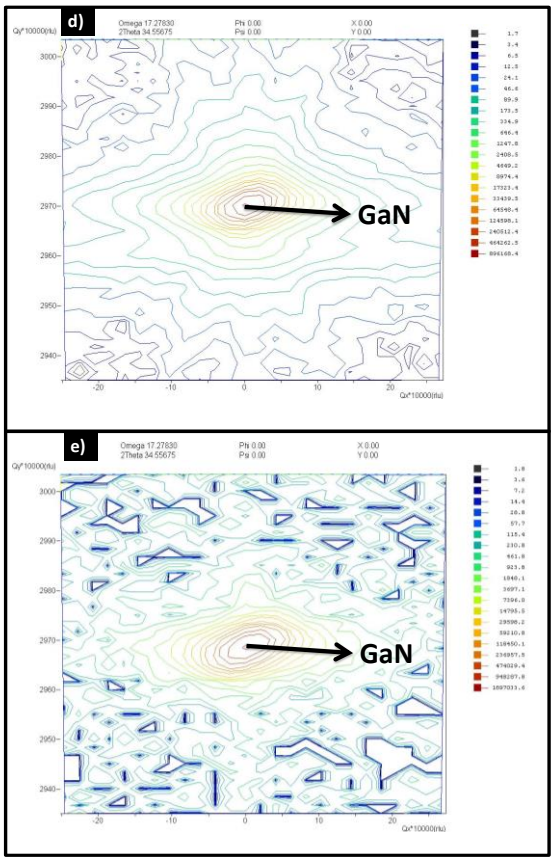

Figure 5.9: The reciprocal space mapping spectra of a) GZn, b) GZnA, c) GZnS, d) GZnSA and e) GaN:Mg substrate.

Comparing all the information obtained on structure of the material, it can be concluded that the ZnO nanorods grown over GaN:Mg substrate showed excellent crystallinity. The ZnO and GaN crystal reflection contributions were able to resolve separately. ZnO nanorods showed similar structure to that of GaN. The

RSM image showed a map of (0002) reflections of the sample, which indicated good quality crystalline growth of ZnO over the substrate.

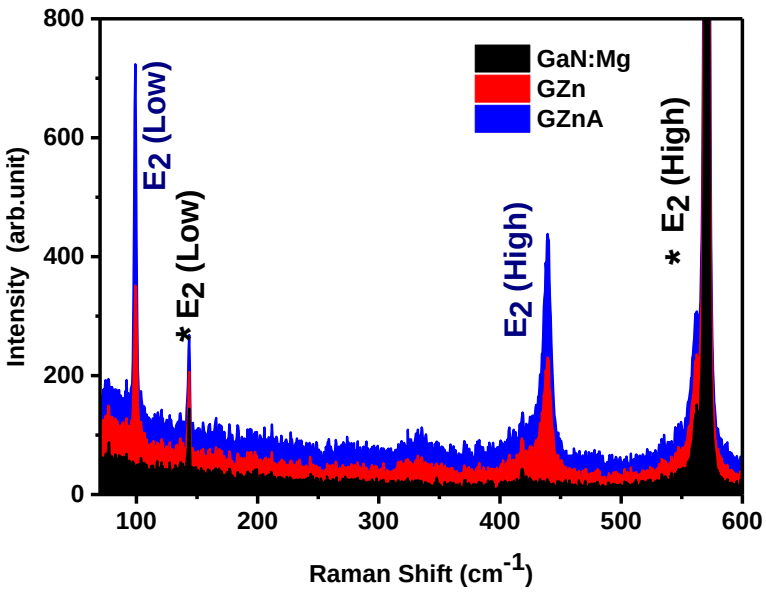

Figure 5.10: Raman spectrum of GaN substrate and GaN/ZnO heterostructure samples.

The Raman spectrum showed characteristic peaks of wurtzite crystalline structure, as shown in figure 5.10. GaN:Mg substrate showed two characteristics peaks (denoted with a "*") at 144 cm^{-1} and 570 cm^{-1} which corresponds to E_2(Low) and E_2(High) respectively[17]. For GZn and GZnA two Raman peaks at 100 cm^{-1}

and 439 cm^{-1} were obtained. The peaks corresponds to E_2(Low) and E_2 (High) phonon modes of wurtzite crystalline ZnO[18–22]. The intense E_2(High) mode is a clear indication of strong phonon vibration modes along polar c-axis[23]. The intensity of both Raman modes observed in the sample increases on annealing in air. This is a clear indication of improvement in the crystal structure of ZnO nanorods.

Photoluminescence spectrum (PL) of various samples is shown in figure 5.11. In the case of PL of GaN:Mg substrate one weak emission at 365 nm and another strong emission at 440 nm were observed. The weak emission peak at 365 nm is due to the band to band transition. It is already reported that doping of Mg in GaN will create an additional acceptor level at 2.8 eV. The 440 nm (2.8 eV) emission can be attributed to the acceptor level created due to Mg doping. For higher doping concentrations of Mg, the 2.8 eV PL emission will start to dominate[24–26]. In the case of PL of ZnO nanorods, both GZn and GZnA showed a strong emission at 380 nm and another broad emission at 580 nm. The emission at 380 nm is an intense near band edge emission (NBE) of ZnO and the broad emission at 580 nm can be attributed to deep level emissions from (DLE) defect states. The broad DLE is visibly strong for GZn, but on annealing the DLE get quenched considerably (in the case of GZnA). The relative intensity of ZnO DLE to NBE in GZn is 115% while that for GZnA is 0.28%, which shows that DLE suppressed on annealing in air. Figure 5.11(b) and (c) shows the

magnified view of DLE of GZn and GZnA respectively. For GZn, three peaks centered at 544 nm, 593 nm and 642 nm were observed on de-convoluting its DLE. Based on the observations of resolved DLE for GZn three defect levels such as oxygen interstitials (O_i), Zinc interstitials (Zn_i) and oxygen vacancy (V_o) can be proposed. The oxygen interstitials (O_i) are created at 2.28 eV below conduction band minimum of ZnO. Zinc interstitials (Zn_i) are created at 2.9 eV above valance band maximum for zinc rich samples. Oxygen vacancy (V_o) level is created at 0.9 eV above valence band maximum. The Vo is observed to be created easily due to their lower formation energy compared to Zn_i[19,27–29].

Thus in the case of GZn the transition from conduction band minimum to O_i can be a reason for 544 nm emission. The 593 nm emission can be thought of a transition to V_o from Zn_i. Also, the 642 nm emission can be connected to the transition from Zn_i to O_i. Thus, all observed emissions matches well with previously reported defect levels as shown in figure 5.11(d).

For annealed sample GZnA, the DLE can be de-convoluted in to two peaks as shown in figure 5.11(c). The 642 nm emission had quenched completely, while the intensity of other two emissions reduced considerably. The absence of 642 nm emission and very weak 544 nm emission suggests that the interstitial defect states have disappeared almost completely. The presence of 593 nm emission suggests that V_o state is still present in ZnO nano-

rods. Thus the quenching behavior of the PL DLE emissions can be attributed to reduction of defect states. Annealing in air helped in successfully removing majority of interstitial defect states previously observed in GZn.

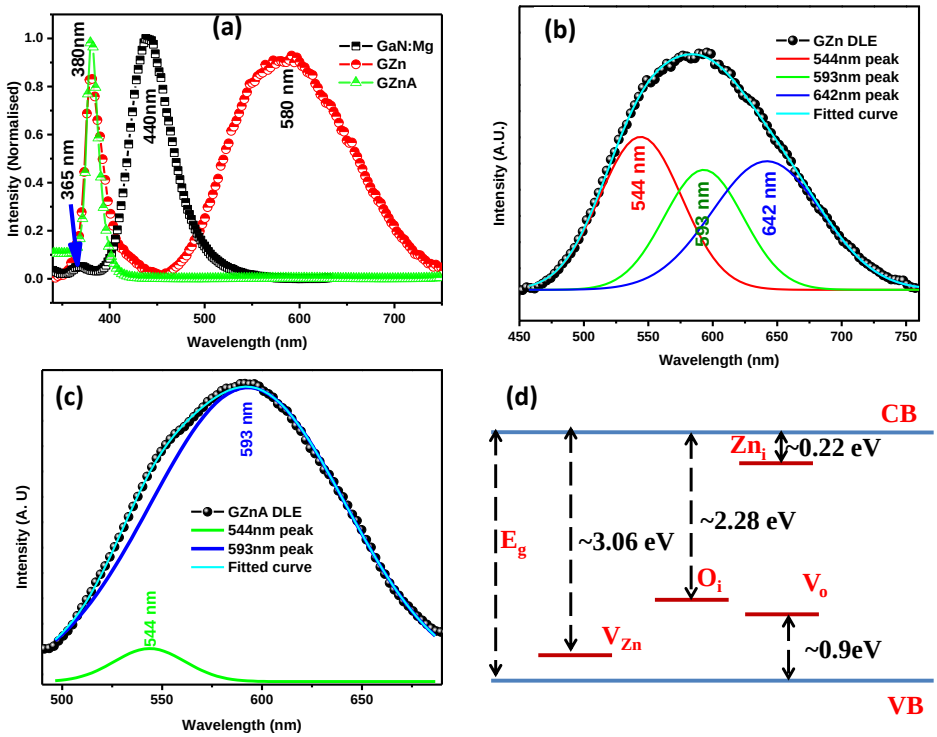

Figure 5.11: (a) Photoluminescence spectrum of ZnO nanorods and GaN substrate. (b) The magnified view of resolved deep level emissions of GZn and (c) GZnA. (d) The sub band gap defect levels in ZnO reported in the literature.

The transmission spectrum of various samples are shown in figure 5.12. The GaN:Mg substrates showed above 70% transmission in visible and infrared wavelength regions. On growth of ZnO nanorods, the transmission reduced remarkably. The seed layered sample (GZnS) showed least transmission with 20% in infrared region and nearly 0% in visible region. At the same time, for non-seed layered sample (GZn) the transmission is almost 20% in infrared region, but it showed ~5% in visible region, a slight increase from that of GZnS.

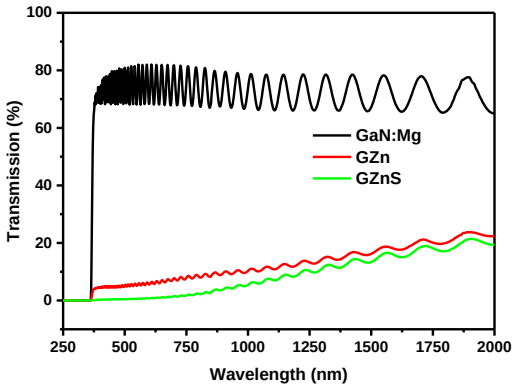

Figure 5.12: Transmission spectrum of GaN substrate and GaN/ZnO heterostructures.

The remarkable reduction in transmission can be attributed to the scattering effect of the nanorod array, as the faces of nanorods scatter the incoming light in all directions. This property can be used effectively for light capturing devices, like solar cell, photo

detectors etc. Since majority of the incoming light can be blocked from transmitting, these energies can be carefully utilized for increased device performance in these applications. High efficiency solar cells are made with patterned rough surface to increase the light collection ability. ZnO nanorods under this discussion can be utilized in those devices, where the nanorods can act as both scatterer and active material.

5.4 Conclusions

Vertically aligned ZnO nanorods were successfully grown over GaN:Mg substrate by low temperature solution process. The morphological, structural and optical properties of the nanorods were studied. FESEM analysis confirms the formation of vertically aligned ZnO nanorods, and the characteristic hexagonal phase of wurtzite crystalline structures were observed. The seed layered samples showed decreased nanorod diameter and increased number density. The high resolution X-ray studies showed good wurtzite crystallinity. Rocking curve and pole figure analysis showed preferred orientation of ZnO nanorods in $< 0002 >$ crystal planes. The observation of pole figure for $< 10\bar{1}2 >$ shows the crystalline quality of nanorods. Reciprocal space mapping studies showed the crystalline quality of (0002) planes. Seed layered samples showed poor crystalline behavior compared to non-seed layered samples. Raman studies showed intense E_2 phonon modes, a signature of c-plane preferred oriented growth of ZnO. Photoluminescence studies

revealed various defect states in the material and its changes on annealing. The transmission studies showed that majority of incoming light is being scattered in visible region. All the studies indicate that annealing has greater impact on the nanorods' crystallinity and defect states. Annealed samples showed lesser defect states with improved crystallinity. This simple solution based nanorod growth technique can be adopted for the epitaxial growth of ZnO nanorods on GaN substrate. Annealing the nanorods is an efficient way to control the defect density produced during the growth stage. The hydrothermal technique can be used for fabrication of GaN/ZnO heterostructure for various optoelectronic applications.

5.5 References

[1] E. Przeździecka, K. Gościński, M. Stachowicz, D. Dobosz, E. Zielony, J.M. Sajkowski, M.A. Pietrzyk, E. Płaczek-Popko, A. Kozanecki, Sensors Actuators A Phys. 195 (2013) 27.

[2] X. Zhang, X. Han, J. Su, Q. Zhang, Y. Gao, Appl. Phys. A 107 (2012) 255.

[3] C.H. Chen, S.J. Chang, S.P. Chang, M.J. Li, I.C. Chen, T.J. Hsueh, A. Di Hsu, C.L. Hsu, J. Phys. Chem. C 114 (2010) 12422.

[4] J.H. Wu, S.Y. Liu, S. Li, Y. long Jiang, G.P. Ru, X.P. Qu,

Appl. Phys. A 109 (2012) 489.

[5] O. Lupan, T. Pauporté, L. Chow, G. Chai, B. Viana, V.V. Ursaki, E. Monaico, I.M. Tiginyanu, Appl. Surf. Sci. 259 (2012) 399.

[6] O. Lupan, T. Pauporté, B. Viana, I.M. Tiginyanu, V. V. Ursaki, R. Cortès, ACS Appl. Mater. Interfaces 2 (2010) 2083.

[7] H. Gomez, S. Cantillana, G. Riveros, S. Favre, C.J. Pereyra, D. Ariosa, R.E. Marotti, E.A. Dalchiele, Int. J. Electrochem. Sci. 8 (2013) 10149.

[8] R. Chander, a. K. Raychaudhuri, J. Mater. Sci. 41 (2006) 3623.

[9] D.Y. Son, K.H. Bae, H.S. Kim, N.G. Park, J. Phys. Chem. C 119 (2015) 10321.

[10] J. Eisner, M. Haugk, R. Gutierrez, T. Frauenheim, Mater. Res. Soc. Symp. Proc. 482 (1998) 935.

[11] M. Seelmann Eggebert, J.L. Weyher, H. Obloh, H. Zimmermann, A. Rar, S. Porowski, Appl. Phys. Lett. 71 (1997) 2635.

[12] J.L. Weyher, S. Müller, I. Grzegory, S. Porowski, J. Cryst. Growth 182 (1997) 17.

[13] L.E. Greene, M. Law, D.H. Tan, M. Montano, J. Goldberger, G. Somorjai, P. Yang, Nano Lett. 5 (2005) 1231.

[14] D.C. Kim, W.S. Han, B.H. Kong, H.K. Cho, C.H. Hong, Phys. B Condens. Matter 401-402 (2007) 386.

[15] S. Lee, Y. Sohn, C. Kim, D.R. Lee, H.-H. Lee, Nanotechnology 20 (2009) 215703.

[16] T. Pauporté, D. Lincot, Appl. Phys. Lett. 75 (1999) 3817.

[17] V. Davydov, Y. Kitaev, I. Goncharuk, A. Smirnov, J. Graul, O. Semchinova, D. Uffmann, M. Smirnov, A. Mirgorodsky, R. Evarestov, Phys. Rev. B 58 (1998) 12899.

[18] S. Guo, Z. Du, S. Dai, Phys. Status Solidi 246 (2009) 2329.

[19] M. Gomi, N. Oohira, K. Ozaki, M. Koyano, Jpn. J. Appl. Phys. 42 (2003) 481.

[20] A. Umar, B. Karunagaran, E.K. Suh, Y.B. Hahn, Nanotechnology 17 (2006) 4072.

[21] B. Kumar, H. Gong, S.Y. Chow, S. Tripathy, Y. Hua, Appl. Phys. Lett. 89 (2006) 071922.

[22] S.S. M, J. Koshy, A. Chandran, K.C. George, Indian J. Pure Appl. Phys. 48 (2010) 703.

[23] H. Zhu, J. Iqbal, H. Xu, D. Yu, J. Chem. Phys. 129 (2008) 124713.

[24] U. Kaufmann, M. Kunzer, M. Maier, H. Obloh, A. Ramakrishnan, B. Santic, P. Schlotter, Appl. Phys. Lett. 72 (1998) 1326.

[25] B. Monemar, P.P. Paskov, G. Pozina, C. Hemmingsson, J.P. Bergman, S. Khromov, V.N. Izyumskaya, V. Avrutin, X. Li, H. Morkoç, H. Amano, M. Iwaya, I. Akasaki, J. Appl. Phys. 115 (2014) 053507.

[26] B. Monemar, S. Khromov, G. Pozina, P. Paskov, P. Bergman, C. Hemmingsson, L. Hultman, H. Amano, V. Avrutin, X. Li, H. Morkoç, Jpn. J. Appl. Phys. 52 (2013) 08JJ03.

[27] C.H. Ahn, Y.Y. Kim, D.C. Kim, S.K. Mohanta, H.K. Cho, J. Appl. Phys. 105 (2009) 013502.

[28] P.A. Rodnyi, I. V. Khodyuk, Opt. Spectrosc. 111 (2011) 776.

[29] B. Lin, Z. Fu, Y. Jia, Appl. Phys. Lett. 79 (2001) 943.

Chapter 6

Study of ZnO nanorod/GaN heterojunction devices for LED and UV photodetector applications

6.1 Introduction

One of the major applications of ZnO nanostructures is the use in heterojunction. Solution grown ZnO nanostructures in general show stable n-type conductivity. Though there are several reports on p-type conductivity in ZnO[1–3], growth of stable p-ZnO is still a challenge. Hence, to form a p-n heterojunction different p-type materials like p-Si[4,5], NiO[6–8], CuO[9–12], GaN[13], ScAlMgO$_4$[14], etc., were used as p-layer in the heterostructure. Even, heterostructure based on SnO$_2$/ZnO/PEDOT structure is also reported[15].

Table 6.1: Properties of GaN and ZnO.

	GaN	ZnO
Crystal structure	Hexagonal wurtzite	Hexagonal wurtzite
Band Gap	3.4 eV	3.3 eV
Exciton binding energy	29 meV	60 meV
Lattice parameters	a=b=3.186 Å c=12.99 Å	a=b=3.249 Å c=5.178 Å

Among various p-type materials, p-GaN has several advantages when forming heterojunction with ZnO. Both have same hexagonal wurtzite crystalline structure with very close band gap and other structural optical properties (Table 6.1). ZnO and GaN have similar exciton binding energy of 60 meV and 29 meV respectively [3,16–18]. ZnO nanorod based heterojunctions are mainly deployed in two types of devices, LEDs and light detectors.

Since, both ZnO and GaN are wide bandgap (>3 eV) semiconductors, GaN/ZnO heterojunction usually gives strong UV emission[19]. Visible emission from these devices is achieved by the addition of phosphor material or band structure modification[20]. ZnO based LED devices emitted light in various visible ranges including violet[21,22], blue[23–25], yellow[24,26], red[20] etc. Choosing right seed layer thickness along with proper experimental con-

ditions can tune emission wavelengths[27]. Nanorod dimensions have a direct impact on the intensity of emitted light. The intensity of the emission usually increases with nanorod diameter[28].

White light emitting LEDs are recently being widely used in solid state lighting industry. GaN/ZnO based LEDs also demonstrated its potential in this field[23,24]. P-Si/n-ZnO heterojunction also showed broad visible emission[4,29]. But, the GaN/ZnO based LEDs with an external quantum efficiency of ~2.5% reported to show stable operation for more than 90 hr[30]. Lupen et al. showed blue light from GaN/ZnO heterojunction changes to white light on doping with Ga[23]. GaN/ZnO LEDs showed light emission even under reverse bias[26,31,32]. Hot carrier injection and tunneling breakdown are thought to be the reason for reverse bias emission from these devices. Zhan et al. reported the shift of emission from yellow to blue and UV wavelength regions on increasing the reverse bias from 3 volt to 7 volt[24]. Recent studies demonstrated white light emission from ZnO nanorod and nanotube based devices with high junction currents like 350 mA, which is so close to the present silicon technology. This promising result suggests that in the near future these highly efficient devices can replace Si devices.

Waveguide effect of 1D ZnO nanorod allows better light coupling efficiency and enhanced emission in ZnO nanorod based LEDs[33,34]. Apart from 1D nanorod ZnO based micro cylinder[35] and cone shaped semiconductor offers more light emis-

sion efficiency, due to the multiple reflections inside the nanostructures.

Wu et al. investigated the region from where emission originates in GaN/ZnO LEDs[36]. They showed that emission originates from p-GaN side in a GaN/ZnO heterostructure when the ZnO nanorods are grown without any seed layer or when the ZnO nanorods are grown above ion-beam sputtered seed layer. If ZnO nanorods are grown over sol-gel deposited seed layer, the emission will originate from ZnO side. Since, emission originates from different regions, the emission properties will also be different. According to Ng et al. slight variations induced even at the interface can trigger dramatic changes in electroluminescent emission[27]. Even though the photoluminescence are the same, interface fluctuations change the electroluminescent emission. This points to the fact that heterojunction interface quality is an important parameter which decides the quality and reproducibility of light emission. The fluctuations in interfacial band alignment due to the changes in interface quality are expected to be the reason for the observed changes in emission properties. The theoretical study by Schuster et al. discusses the interface quality dependence on light emission[37]. Even the polarity of ion in the terminating end of ZnO nanorod is important. According to their studies choosing suitable polarity can trigger even UV lasing in these devices. The demonstration of light emission perpendicular to the polar c-axis

by Du et al. which is different from previous reports, also emphasise the need to understand the interface properties clearly[38].

Most of the previous reports in literature use expensive processes like MOCVD for fabrication of ZnO layer, where as in the present study a relatively simple solution processing is used. Compared to electrochemically grown nanorod based devices, hydrothermally grown nanorod based devices shows lower emission threshold[21].

In the present study, nanorods were grown using zinc acetate and ammonium hydroxide based hydrothermal synthesis. The fabricated devices shows low threshold emission for forward and reverse bias compared to previous reports[36]. The effect of post deposition annealing has also been investigated.

ZnO thin film has been utilized for the fabrication of ZnO based light detectors [39–42]. The variation of resistivity on light exposure especially UV light is monitored in these devices. Even micro rods of ZnO has also been used in earlier studies [43]. Recent developments in growth of ZnO based nanostructures make them appealing for light-sensing applications also. Several results showed highly spectrum-selective light sensors with good responsivity. Some recent reports on ZnO 1D nanostructure based light sensors are consolidated in table 6.2. Recent studies concentrate on ZnO based heterojunction light detectors rather than the initial resistive devices. Reports as in table 6.2 suggest that compared to

resistive devices heterojunction devices offers faster response with high responsivity.

Heterojunction device fabrication used various approaches to improve the device performance. For a MOCVD grown, p-type ZnO:As based detector, a response time of 2 ms for 368 nm, 10 W light source was observed[44]. Another idea is to form a 3D photodetector by winding Pt over ZnO nanowire in a ZnO/NiO heterojunction. Since it can couple piezoelectric properties of ZnO along with heterojunction properties, the device can respond to both UV light and tensile stress. Even the piezo electric characteristics are enhancing the photo detector capabilities[45]. Das et al. reported a single ZnO nanorod based Schottky UV detector, which can give reasonable response to very low light intensity[46]. Such a device structure is extremely helpful to detect low power light signals. In yet another approach, a surface acoustic wave(SAW) based Si/ZnO oscillator is formed, which shows frequency shift on UV light exposure. The device responded to a 551 µW/cm^2 UV light by triggering a frequency shift of 1017 kHz[47].

In a recent report by Zhan et. al., milli second response time was recorded for UV light in ZnO based heterojunction devices [13,48]. They observed a faster rise time of 64 ms and a relatively slower decay time of 270 ms. The reason for such a variation is attributed to the barriers in ZnO/GaN heterojunction. These results suggest that thorough understanding of the heterojunction

interface is necessary to fabricate a good device. Such interface engineered device can give improved performance.

Moreover, expensive and high temperature processing techniques like MOCVD, CVD, VLS etc. are generally used to fabricate good quality ZnO nanostructures to form heterojunctions. Several reports on solution based synthesis processes like electrodeposition, dip coating, hydrothermal synthesis etc. were investigated to grow ZnO nanostructures in ZnO based heterojunctions. One of the main drawbacks associated with such devices is slow response time. Poor crystalline quality of ZnO nanostructures grown by these techniques may be a reason for the lack of performance.

In the present work highly crystalline ZnO nanorods grown over p-GaN substrate by hydrothermal synthesis is used to fabricate a p-GaN/n-ZnO heterojunction. The crystalline quality of hydrothermally grown ZnO nanorods matches with those fabricated by the sophisticated techniques like MOCVD, CVD, VLS etc. Detailed analysis on heterojunction is performed

Table 6.2: Recent reports on ZnO nanostructure based light sensors.

	Type	Growth mechanism	Nanostructure	Peak detection Wavelength (nm)	Maximum photosensitivity	Responsivity (A/W)	Bias (V)	Rise time	Fall time	Year of publication	Reference
1	Resistor	Vapor phase transport	Single Nanowire	365	10^4 – 10^6		1	<1s	<1s	2002	[49]
2	Resistor	DVP	Nanowire + Sphere	~370	10^6		1	2.3s	0.5s	2007	[50]
3	Resistor	CVD	Nanowire	397	10^2				58.5s	2009	[51]
4	Resistor	ACG method	Nanowire	<400					149s	2009	[52]
5	Resistor	Sputtering	Thinfilm		10^4		5	86ms	355ms	2010	[53]
6	Heterojunction	Dip coating	Nanowire	370				10s	62s	2010	[54]
7	Resistor	Solution growth	Nanowire	UV	27		8		1min	2010	[55]
8	Schottky junction	VLS	Nanowire	325	9					2010	[56]
9	Schottky junction	MOCVD	Nanowire							2010	[46]
10	Heterojunction	Solution growth	Nanorod	370			5			2011	[57]
11	Heterojunction	MOCVD	Nanowire	365	1344.5	30	-5	<160ms	<350ms	2011	[58]
12	Resistor	VLS	Nanowire	369	24200		2.5	> 10s	> 10s	2011	[59]
13	Heterojunction	CVD	Nanowire	367	10^6	-	3	20 μs	219 μs	2011	[60]

14	Heterojunction	CVD	Nanowire	365			5	64 ms	30 ms	2012	[48]
15	Heterojunction	Molecular beam epi-taxy	Thin film	374		6.2 m	-2		<2ms	2013	[44]
16	Heterojunction	CVD	Nanowire	365	8		1	7.5s	8.6s	2014	[45]
17	Resistor	Floating Zone method	Microwire	390		5.6m	5			2014	[43]
18	Resistor	Hydrothermal	Nanorod	370	10^3	1.7	5	72s	110s	2014	[61]
19	Heterojunction	Electrodeposition	Nanorod	<400		22	0.65	> 10s	> 10s	2014	[9]
20	Heterojunction	Hydrothermal	Nanorod	365			1	1.69s	13.56s	2014	[62]
21	Heterojunction	Hydrothermal	Nanorod	362		1.81	-10	<1s	<1s	2015	[13]
22	Resistor	Hydrothermal	Nanorod	365			3	80s	20s	2015	[63]
23	Transistor	Hydrothermal	Nanorod	<350		$3X10^5$	1	1.2s	1.9s	2015	[64]
24	Heterojunction	Solution process	Nanorod	360			5	1.345s	0.132s	2015	[65]
25	Resistor	Hydrothermal	Nanorod	365	37.4		10		26.1s	2015	[66]
26	Resistor	Solution process	Nanorod				5	3s	30s	2015	[67]
27	Heterojunction	Hydrothermal	Nanorod	360	5	11	4	288 μs	323 μs	2016	[68]*

* Present study.

6.2 Experimental

ZnO nanorods were grown by hydrothermal synthesis using 0.1 M zinc acetate solution. NH_4OH solution was added to the zinc acetate solution to make the pH of the precursor solution above 9. Suitable substrate was horizontally placed inside an autoclave along with the precursor solution at 180 °C for 1 hour. In one set of samples nanorods were grown directly over GaN:Mg substrate and in another set nanorods were grown over ZnO seed layer deposited GaN:Mg substrate. The nanorod growth and seed layer deposition techniques were explained in section 5.2 in the previous chapter. Post deposition annealing at 350 °C for 6 h was also performed on selected samples.

Au is selectively deposited over ZnO nanorods through a shadow mask using thermal evaporation technique. Conducting Ag paint was applied over GaN:Mg substrate. The Ag and Au act as two electrodes which complete the heterojunction structure Ag/GaN:Mg/ZnO nanorod/Au as shown in Figure 6.1. Ag usually forms ohmic contact with GaN. Moreover, it is reported that it improves the emission properties of GaN based LEDs[69,70]. We have also observed that Ag forms ohmic contacts for GaN:Mg.

In the present study, four different types of heterojunctions were fabricated. The details of sample name and its description are given in the table below. In the sample names GZn means pre-

pared GaN/ZnO heterojunction. The last letter 'S' stands for seed layer and 'A' for post deposition annealing.

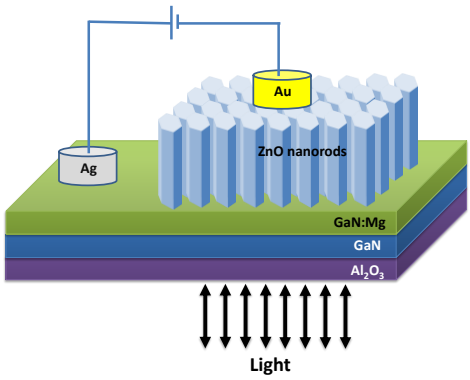

Figure 6.1: Schematic representation of n-ZnO/p-GaN heterojunction.

Table 6.3: List of sample name and its details.

Sample name	Details
GZn	Heterojunction formed by as grown ZnO nanorods over GaN:Mg substrate, without seed layer and without post deposition annealing
GZnA	Heterojunction formed by ZnO nanorods over GaN:Mg substrate without seed layer and with post deposition annealing
GZnS	Heterojunction formed by ZnO nanorods grown over GaN:Mg substrate with seed layer and without post deposition annealing
GZnSA	Heterojunction formed by ZnO nanorods grown over GaN:Mg substrate with seed layer and with post deposition annealing

Electrical characteristics of the heterojunction devices were measured in Biologic SP-300 potentiostat/galvanostat equipped with 1A current booster. The electroluminescence emission and photoresponse measurements of the devices were measured using Fluromax-3 spectrophotometer with the help of Biologic SP-300 potentiostat/galvanostat. During EL measurements the potentiostat is used to bias the device while emission was recorded in Fluromax-3 spectrophotometer. The device was illuminated with various wavelengths of light selected using Fluromax-3 spectrophotometer and photoresponse of the device for each incident wavelength was recorded with the help of a potentiostat/galvanostat. The fastness of the device performance is measured using a chopped beam of light from He-Cd continuous wave laser. Stanford research systems' optical chopper and chopper controller is used to chop 325 nm UV light from He-Cd laser. The chopped light pulses were allowed to fall on the device while a constant biasing was applied to the device as shown in figure 6.8(a). A Rohde & Schwarz RTM 1054 digital oscilloscope is used to record the current variations caused by short UV light pulses. For the EL emission and photoresponse studies, the light is allowed to pass through Al_2O_3 side of the device.

6.3 Results and Discussions

6.3.1 Electrical properties of the heterojunction

The V-I characteristics of the heterojunction devices are shown in Figure 6.2. Figure 6.2(a) gives the V-I characteristics of GZn and GZnA based heterojunctions, while Figure 6.2(b) gives the V-I characteristics of GZnS and GZnSA based heterojunctions. All the devices showed rectifying nature. Heterojunction fabricated over seed layer deposited substrate showed lower current compared to heterojunction fabricated without seed layer. The rectification ratios of these junctions are ~4.5 for heterojunctions fabricated without seed layer and ~1 for heterojunctions with seed layer. All heterojunctions showed increase in junction current on UV illumination.

A series resistance of ~12kΩ was observed for the devices without any seed layer, while seed layered samples offer very high series resistances of the order of MΩ (GZnS = 4 MΩ, GZnSA = 10 MΩ). The increase in series resistance may be the reason for obtaining reduced junction current. The V-I characteristics revealed that the seed layer is blocking the flow of charge carriers through the heterojunction by offering very high series resistance. Hence, the seed layer is effectively degrading the p-n heterojunction performance.

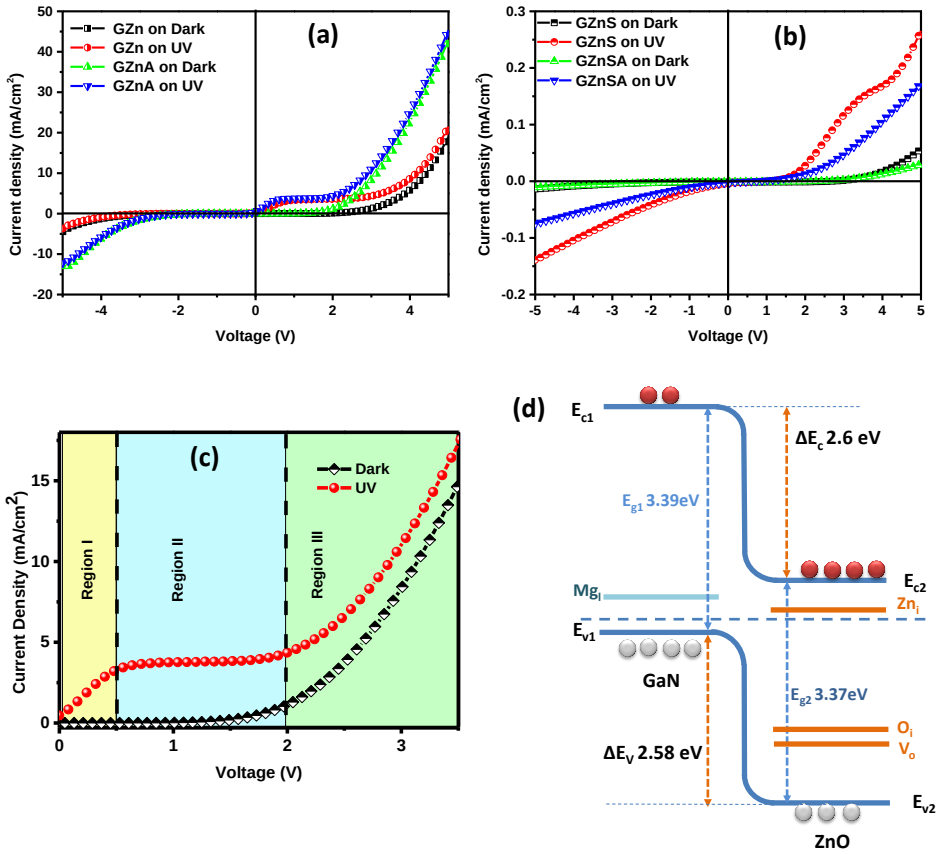

Figure 6.2: The V-I characteristics of (a) non-seed layered heterojunctions (GZn & GZnA) and (b) seed layered heterojunctions (GZnS & GZnSA). (c) The magnified view of V-I characteristics of GZnA heterojunction. (d) Proposed band structure of the heterojunction.

As synthesized sample (GZn) showed a knee voltage of 3.87 V. GZnA recorded higher current density compared to GZn and lower knee voltage (2.6 V). Annealed samples also show increase in

intensity of X-ray and Raman peaks (Chapter 5) indicating the decrease in crystalline defects. Improvement in crystalline nature results in better interface between ZnO nanorods and GaN:Mg layers with lesser grain boundaries. Reduction in interfacial defects and grain boundaries means charge carriers can cross the interface with ease. The reduction in defect states of the device on annealing is also evident from PL studies. Modification of defect states may result in slight band realignment, which in turn decreases the energy barrier height at the interface resulting in reduced knee voltage as observed in GZnA. Various heterojunction parameters obtained from the V-I characteristics are described in Table 6.4.

Table 6.4: Heterojunction parameters extracted from the V-I characteristics.

Sample	Knee voltage (V)		Series Resistance (kΩ)		Rectification ratio at 3.5V	
Name	Dark	UV	Dark	UV	Dark	UV
GZn	3.87	3.76	11.95	11.51	4.71	16.87
GZnA	2.60	2.44	12.29	12.41	4.50	5.70
GZnS	3.82	2.97	4180.69	1530.63	0.99	1.71
GZnSA	3.46	2.39	10236.89	3025.03	1.00	1.53

The photoluminescence studies (Chapter 5) revealed the presence of various defect states in GaN and ZnO nanorod layers of the device. Based on the inference from PL studies and V-I

characteristics, a band structure is proposed as shown in Figure 6.2(d). The knee voltage (ΔEc) observed for GZnA is 2.6 V. ΔEv of 2.58 is observed from the band diagram where, $\Delta Ev = Eg_2 + \Delta Ec - Eg_1$. From the PL studies (chapter 5), the creation of an additional acceptor level M_{gl} at 2.8 eV due to Mg doping in GaN is observed[71–73]. Whereas, three defect levels are identified for ZnO nanorods from its PL studies. Zinc interstitials (Z_{ni}) is observed at ~0.22 eV below conduction band minimum(E_{c2}), oxygen vacancy (V_o) is observed at ~0.9 eV above valence band maximum(E_{v2}) and oxygen interstitials (O_i) is observed at ~2.28 eV below conduction band minimum(E_{c2})[74–77].

Under dark conditions, the device performs like a normal heterojunction. On UV illumination an anomalous behavior is seen especially under low forward bias (0V - 2 V), where a sudden increase in junction current near to 0V is observed. After 2 V the V-I characteristics followed normal junction characteristics. Figure 6.2(c) shows a magnified view of the region where anomalous V-I characteristics are observed. Ideal V-I characteristics of p-n heterojunction doesn't explain this phenomenon. Possibility of formation of Schottky contact with Au/ZnO can be ruled out as band difference is ~0.5e V and or more. At the same time, the present device showed rise in current at 0V itself. Tunneling theory can be used to explain this phenomenon.

Tunneling in p-n junction will occur for highly doped p-n junctions. Typically, the carrier concentration in such devices ranges from 10^{19} to 10^{20} cm^{-3}. The band structure of such devices will be aligned in a way as the conduction band minimum of p-type semiconductor will overlap with valence band maximum of n-type semiconductor[78]. Another typical characteristic of a tunnel diode is its negative resistance[79–81]. Since heterojunction didn't show any such behavior, a modified model as described below can give some insight into the mechanism of operation in the device.

When the heterojunction is exposed to UV illumination, the photo-excited charge carriers can populate defect states in the band structure. Thus on UV illumination, these defect states can also participate in the conduction of the heterojunction. Hall measurements show that the carrier concentration of GaN:Mg layer under dark conditions is 5 x $10^{17}cm^{-3}$. Hence, on UV illumination, the carrier concentration will increase further, nearing the carrier concentration of a tunnel diode. From the proposed band structure it is clear that the E_{v1} and E_{c2} are so close. Because of the special band alignment and increased carrier concentration tunneling can happen under UV illumination. The sudden rise in junction current for smaller forward bias just after 0 V (Region I) as observed in the present heterojunction is a typical characteristic of a heavily doped tunnel diode. During UV illumination, increased carrier concentration populates various defect states such as M_{gl}, Zn_i and V_o and tunneling can happen even between these defect

states. Tunnel diodes usually possess negative resistance in forward bias region, but, the present heterojunction device showed more or less constant current (as in Region II) without any negative resistance region. For higher forward bias (Region III), the heterojunction follows normal junction properties. For any given time, the junction current has two components: (i) current due to ideal junction (current formed by forced charge carriers crossing the built in potential), (ii) the tunneling current. Below knee voltage the ideal diode current will be nearly zero. Hence in region I and II contribution from ideal diode current can be neglected and tunneling current dominates this region. In region I rapid increase in junction current is caused by the tunneling process. In region II due to the typical band structure of ZnO (where V_o and O_i are found closer to valance band) tunneling continues with almost the same rate. From the theory of tunnel diodes, it can be derived that stable junction current can be obtained with low tunnel current compared to ideal diode current[80,81]. Since the carrier concentration may be matching with the lower threshold limit of a tunnel diode, the tunneling current can be expected to be low. Thus, the absence of negative resistance region can be attributed to typical band structure of the heterojunction and also to the lower tunneling current. When it comes to region III, electrons in n-side acquire enough energy to overcome the potential barrier and reach the conduction band of p-side resulting in a normal p-n junction characteristic. At the same time due to ever increasing energy gap between p-type and n-type semiconductors, contribution from tun-

neling current will be steadily decreasing. Thus, in region III the dominating current will be current due to ideal junction characteristics. Striations of the nanorods may also be a reason for the anomalous electrical property at region II.

All devices showed similar tunneling behavior; but it is prominent for non-seed layered samples (GZn and GZnA). No significant change in current is observed between GZn and GZnA sample under UV illumination on reverse bias (figure 6.2 (a). Devices with seed layer (GZnS and GZnSA) showed increasing reverse current on UV illumination.

6.3.2 Light emission from the heterojunction

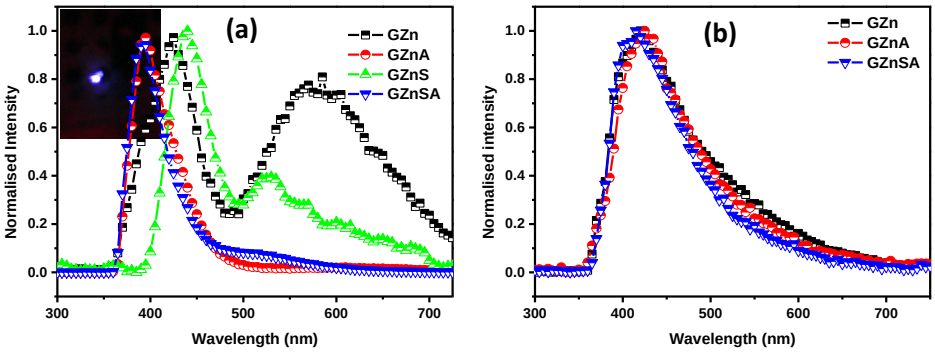

Figure 6.3: Normalised EL emission from heterojunctions (a) under forward bias of 10 V and (b) under reverse bias of -10 V. The photograph of EL emission from GZn at 10 V is shown in inset of Figure 6.3(a).

The heterojunction devices emitted light under both forward (as shown in figure 6.3(a)) and reverse (as shown in figure 6.3(b)) biasing. The emission threshold of the devices under forward bias is around 5 V and that for reverse bias is around 8 V. A plot of normalized EL intensities vs wavelength curve under forward and reverse bias of 10 V is shown in figure 6.3(a) and figure 6.3(b) respectively. Inset of figure 6.3(a) shows the photograph of GZn at 10 V. The GZn heterojunction showed a sharp emission at around 420 nm, and another broad emission around 580 nm. At the same time, the annealed counterpart GZnA showed only one sharp intense peak around 385 nm. Similar to GZn, GZnS sample also showed a sharp peak around 440 nm and a broad peak from 500 nm to 700 nm. On annealing, the broad emission peak for both GZn and GZnS quenched considerably. The annealed samples, GZnA and GZnSA, show only a very weak emission in the green-red region. This trend is very similar to the PL emissions from the corresponding samples as discussed in chapter 5 (figure 5.9). We have already discussed various defect states found in GaN:Mg and ZnO semiconductors. Comparing the EL and PL data it can be concluded that the broad emission is clearly related to various defect states. The broad emission spectra suggest a strong contribution from various defect states in the semiconductors.

On annealing the GZn device, 420 nm emission observed in GZn is shifted to 385 nm as in GZnA. GZnS also has similar emission at 440 nm, which is found to be shifted to 390 nm on anneal-

ing the sample (GZnSA). The emission observed before annealing around 420 nm to 440 nm can be attributed to emission originating from Mg acceptor level along with contributions from other defect states. After annealing, as already discussed, the defect states have been quenched, and crystallinity of ZnO is enhanced. Hence, for annealed sample, the band to band emission of ZnO starts to dominate rather than the weak broad emission, as observed in unannealed samples. In the case of GZn the EL emissions are from defect states and also due to band to band transition. For GZn heterojunction a shoulder peak is visible around 390 nm indicating weak presence of ZnO band to band emission. On annealing, the intensity due to band to band transition dominates, and gives an impression that peak blue shifts on annealing.

The EL emission of GZn for various junction current under forward and reverse bias is shown in figure 6.4 (a) and (b) respectively. Similarly, figure 6.4(c) and (d) show the EL emission of GZnA for various junction currents under forward and reverse bias, respectively. It can also be noted that the EL peak under forward bias is blue shifting for increasing junction currents. There are two processes which form the EL emission, the first one is the free electron-acceptor transition (conduction band to acceptor transition) and the second is the donor-to-acceptor (DAP) transition. As the injection current increases, the number of radiative electron-hole recombination increases. Thus, the blue shift and increase in intensity of intense EL emission peak for higher injection

currents can be attributed to the radiative electron-hole-recombination due to electron injection from ZnO nanorods to GaN:Mg thin film[82,83]. Basically, ZnO band to band emission tries to dominate the EL spectrum on increase in junction current.

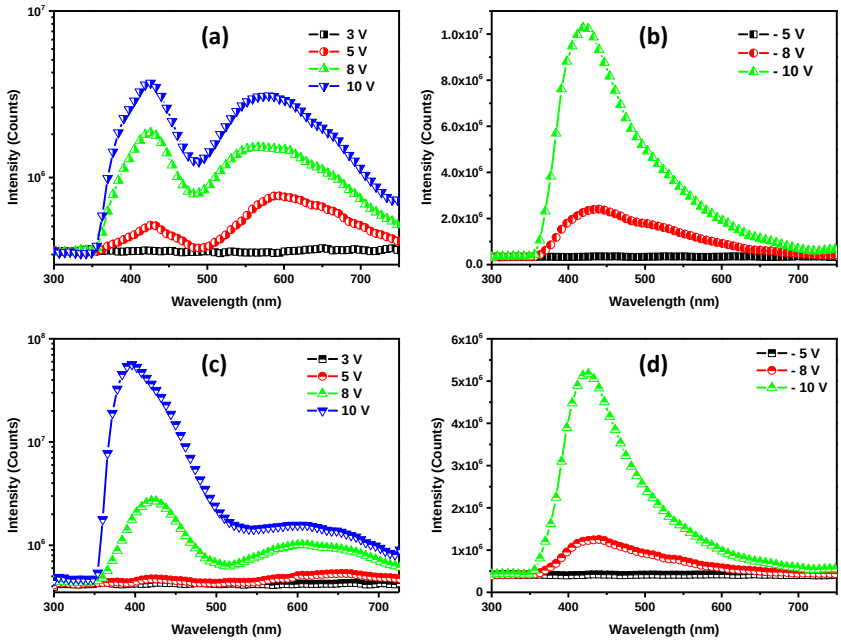

Figure 6.4: The EL emission spectrum of GZn under (a) forward and (b) reverse bias and that for GZnA under (c) forward and (d) reverse bias.

All the heterojunction devices showed similar emissions under reverse bias. For all the samples, the EL peak intensity at 430 nm is observed and it extends almost up to 700 nm. The defect

emission from Mg acceptor level match with the peak emission observed from the heterojunctions under reverse bias. Reverse bias emissions in similar heterojunctions have already been observed earlier[24,26,32,36,84]. In most cases the reverse emission is explained with the help of two possible mechanisms, (i) reverse avalanche breakdown and (ii) tunneling across the interface. Since, reverse breakdown occurs at high voltages, the avalanche breakdown can be ruled out and tunneling possibility is already proposed. But, *Wu et al.* suggest that in the case of p-GaN/n-ZnO heterojunction, the actual charge carrier recombination occurs in GaN thin film substrate[36]. This suggests that the Mg acceptor level related emission could be a possible reason; moreover the observed emission matches with this observation. Hence, the observed reverse emission can be attributed to the combined effect of tunneling and emissions from deep and shallow Mg-acceptor levels.

The CIE color co-ordinates of the emission from fabricated heterojunction devices are plotted in figure 6.5. The co-ordinates are calculated using the 1931 2° CIE Standard colorimetric observer data functions. Under reverse bias all the samples shows similar light emission characteristics (figure 6.5(c)). This observation strengthens the argument that emission originate from the substrate, as variations in ZnO layer didn't affect the emission. Under forward bias, samples without post deposition annealing showed near white emission. On annealing, the emission is shifting to the blue region. As explained, annealing quenches the defect emissions

while improving the EL emission due to band to band transition leading to UV emission from the semiconductor. GZn emits nearly same quality light for almost all forward biases. But for GZnA the emission seems blue shifting as the forward bias increases. Under 10 V forward bias GZnA emits almost UV light with its CIE co-ordinate outside triangle showing its quality for non-display applications.

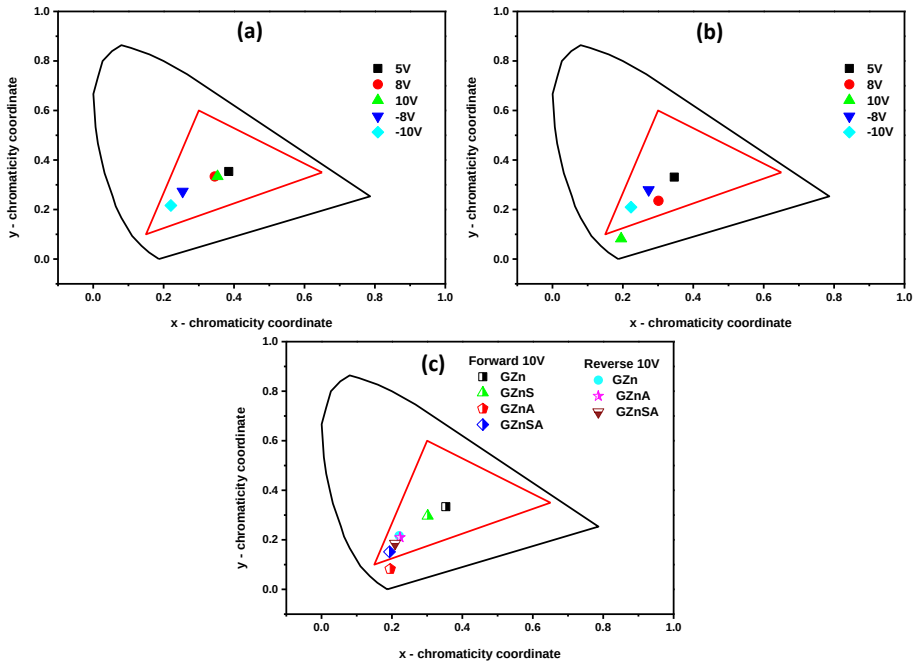

Figure 6.5: The CIE coordinates of (a) GZn and (b) GZnA under different biasing conditions. (c) The CIE coordinates of all the devices (GZn, GZnA, GZnS, GZnSA) at 10V biasing.

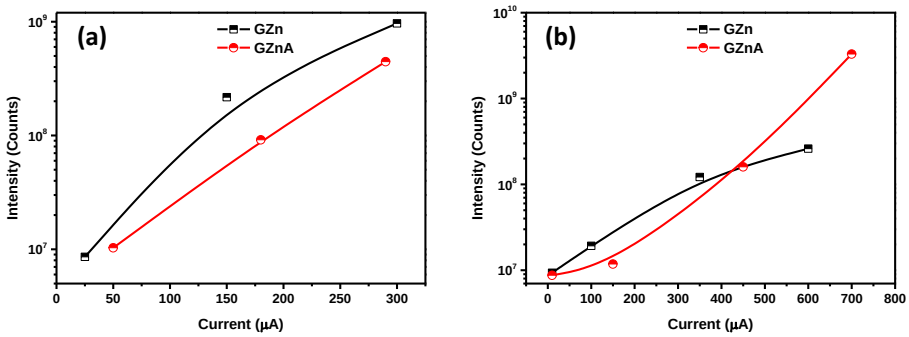

Figure 6.6: The plot of intensity vs junction current for GZn and GZnA under (a) reverse bias and (b) forward bias.

Figure 6.6 shows the dependence of output light of GZn and GZnA heterojunction with junction current under forward (figure 6.6(a) and reverse (figure 6.6(b)) bias. The EL shows non-linear dependence on junction current. The increase in EL emission intensity can be considered as increase in number of radiative recombination. As already discussed, the semiconducting layers of all heterojunctions possess inherent defect states, which are more prominent for those samples which were prepared without annealing (GZn & GZnS). Since, the carrier life time in these defect states are high, it can be viewed as trap levels. When the device is under operation, the charge carriers needs to go through these defect states, and can get trapped. Trapped carriers can result in non-radiative recombinations. Hence, at any time, junction current results in radiative recombinations and trapping of carriers (non-radiative recombinations). The rate of radiative recombination will

be comparable to the rate of carrier trapping for lower injection current as the number of defect states is constant. For higher injection current, the number of radiative recombinations increase with injection current, as the trap states will get filled. This may be the reason for the observed nonlinear dependence of junction current vs EL intensity plot. It is to be noted that under forward bias, the rate of increase in intensity is higher for GZnA, where the defect density is lower.

Thus, emission wavelength of p-GaN/n-ZnO heterojunction showed broad EL emission, while similar device fabricated by annealed ZnO nanorods shows sharp emission in UV-blue region. Observed broad EL emission is due to the presence of various deep level defect states. Thus EL output wavelength is tuned by tuning the defect states in the semiconductor. By selectively altering the defect states, suitable emissions can be achieved successfully. The output power showed nonlinear dependence on junction current.

6.3.3 UV detection

Heterojunction showed increase in junction current on UV light illumination (figure 6.2(a) and (b)). There is remarkable change in current for all heterojunctions under illumination.

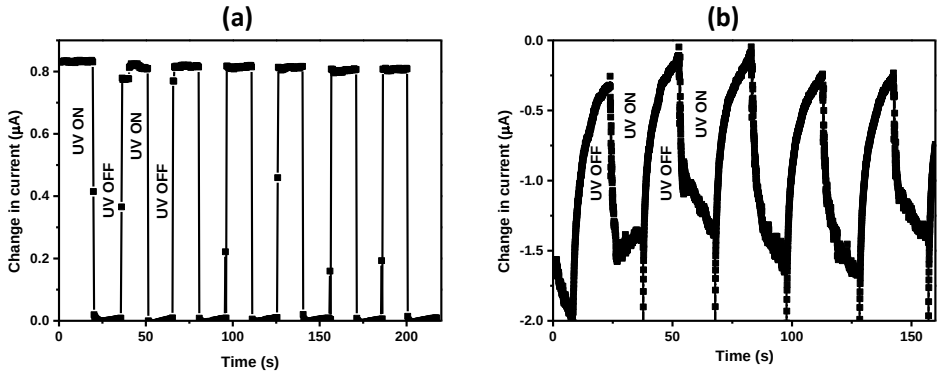

Figure 6.7: Response current of the detector for pulsed UV light under (a) forward bias and (b) reverse bias.

Figure 6.7(a) and (b) show the response of the junction current under forward and reverse bias of 3V. Under forward biasing clear and stable photo current levels for UV illumination and dark conditions were observed, but the same is not saturating over time for reverse bias. Also, the response time for reverse bias seems too slow with the non-linear variation of current over time. Hence, for rest of the measurements the devices were forward biased. GZnS and GZnSA also showed UV response, but the both devices failed to show stable photo currents for UV and dark conditions, even after few seconds. The photoresponse levels also found to shift over time for GZnS and GZnSA devices. Hence, further detailed study on fastness of the heterojunction detectors was restricted to GZn and GZnA only.

The fastness of the device response is measured using a pulsed UV light and a digital oscilloscope as shown in figure 6.8(a). The UV light pulses (325 nm) are created by chopping the laser beam from He-Cd laser with Stanford research systems' optical chopper and chopper controller. Light chopping frequency is precisely controlled by the feedback controller. A dc power supply is connected in series with the heterojunction and a resistance R as shown in figure 6.8(a). A voltmeter is kept across the device to keep exact device biasing before each measurement. A Rohde & Schwarz RTM 1054 digital multi meter measures change in voltage (ac component) across the resistor R. As periodic UV light pulses fall on the device, there will be periodic change in current. This current produces effective voltage changes across the resistance R. Hence, the change in voltage across R can be used to determine the change in current caused by the heterojunction on UV illumination. The response data was then transferred to PC for further study.

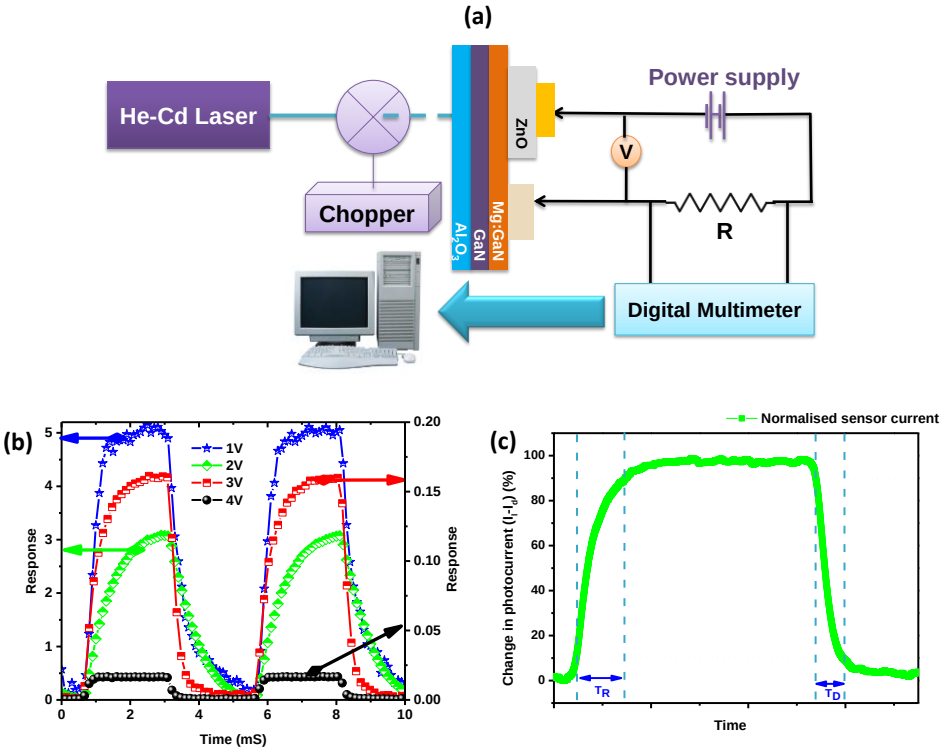

Figure 6.8: (a) Schematic representation of light response measurement setup. (b) GZnA response to UV light pulses at 200 Hz frequency for different bias voltages. (c) Schematic diagram showing rise time and fall time calculations.

Figure 6.8 (b) shows the response of the detector for various forward biasing voltages, by keeping the frequency of UV light pulse at 200 Hz. The response of the detector was measured using the formula

$$Response = \frac{I_l - I_d}{I_d} \quad 6.1$$

Where I_l and I_d denote the photocurrent observed for light and dark conditions respectively.

The total change in photocurrent on UV illumination for each condition was determined, and the rise time (T_R) and fall time (T_D) is taken as the time taken for the photocurrent to change between 10% and 90% of the maximum photocurrent, as shown in figure 6.8(c). Rise time is measured from the leading edge (time to change the current from 10% level to 90% level), and fall time is measured from the trailing edge (time to change the current from 90% level to 10% level) of the junction current response[85,86]. Response parameters of GZn and GZnA, for various forward biasing and light pulse frequencies were extracted and tabulated in table 6.5 and table 6.6 respectively.

Table 6.5: Response parameters of GZn.

Forward bias	Response time	100 Hz	200 Hz
1 V	Rise time (μS)	1918	1522*
	Fall time (μS)	3627	1945*
2 V	Rise time (μS)	3154	1855*
	Fall time (μS)	2506	1723*
3 V	Rise time (μS)	1753	1342*
	Fall time (μS)	1360	1069*
4 V	Rise time (μS)	823	816
	Fall time (μS)	1086	879*

Table 6.6: Response parameters of GZnA

Forward bias	Response time	100 Hz	200 Hz	500 Hz
1 V	Rise time (μS)	605	524	458*
	Fall time (μS)	1510	1210	706*
2 V	Rise time (μS)	1460	1360	656*
	Fall time (μS)	1580	1440	687*
3 V	Rise time (μS)	921	943	492*
	Fall time (μS)	485	477	355*
4 V	Rise time (μS)	290	288	281
	Fall time (μS)	300	323	293

* denotes, stable values not reached.

The "*" denote that stable saturation current levels have not been reached. The response timings for GZn are higher compared

to that observed in GZnA. GZn has stable photoresponse upto 100 Hz only. For 200 Hz, only at forward bias of 4V, rise time showed comparable value. For all other biasing conditions, GZn photocurrent showed no stable saturation current for UV illumination or dark conditions. If the photocurrent does not reach stable levels for UV illumination and dark, calculation of photoresponse gives erroneous values. Under operating frequencies, both devices showed stable photocurrent levels at 3 V and 4 V biasing. Moreover, at 3 V and 4 V biasing, the response timings of the samples were lower (means faster response) compared to lower voltages for both the heterojunction devices.

It is clear from the V-I studies (figure 6.2 (a) &(b)) and band diagram (figure 6.2 (d)) that under forward bias of 1 V and 2 V due to the mismatch in the conduction band bottom edges of GaN:Mg and ZnO semiconductors, the major possibility of the heterojunction is to tunnel charge carriers through the junction. But, under 3V and 4V biasing, the charge carriers will get enough energy to overcome the band mismatch for smooth passage of charge carriers through the junction, resulting in faster response timings. It is also seen that the fall time of the detector is higher than the rise time, indicating the de-excitation process is harder than the excitation process. V-I and PL studies reveal that the conduction mechanism is assisted by defect states present in both semiconductors. As defect states are known to hold the charge carriers longer, the decay process is taking longer time to de-excite

the carriers, which may be a possible reason for obtaining larger fall time. Altogether, the heterojunction device showed good response to UV light pulses and showed its capability to detect light pulses having pulse width well below milli seconds. In the case of GZnS and GZnSA, the presence of increased defect states can be a reason for obtaining slow response behavior. GZnA showed fastest response time of ~300 μs under 4V forward biasing.

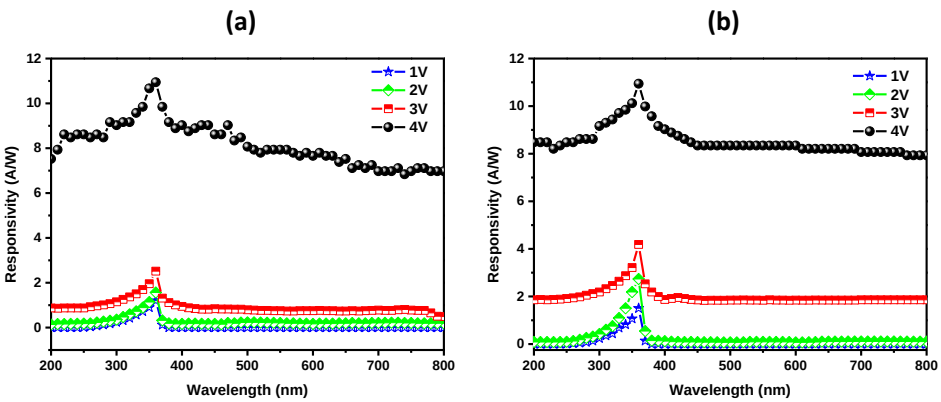

Figure 6.9: Responsivity curve for (a) GZn and (b) GZnA detectors.

Figure 6.9 (a) and (b) shows photoresponse of the GZn and GZnA heterojunctions respectively. Both devices showed selective response to UV wavelength region. Both heterojunctions showed a maximum response at 360nm where the corresponding energy is comparable to the band gap energy of GaN:Mg. Hence, p-GaN has major role in the sensing behavior of the heterojunctions. A gradual decrease in photo current is seen on both sides of the peak re-

sponse point at 360 nm, for both 3 V and 4 V bias. For lower forward biasing of 1V and 2V, a sharp increase in photoresponse at 360nm is observed, as we move from higher wavelength light to lower wavelength light. This indicates that junction current increases rapidly when a light of wavelength 360 nm falls on the device. Since 360 nm light matches with the band gap of p-GaN layer, photo-absorption and carrier generation may occur in p-GaN on 360 nm illumination. This observation also supports the proposed tunneling behavior as tunneling may be happening below knee voltage due to photo excited excess charge carriers. Above knee voltage charge carriers can cross the junction even on absorption of photons with energy slightly lesser than band gap energy, as charge carriers can cross the barrier offered by the junction at this moment. Majority of recent reports on ZnO nanorod based heterojunctions, as discussed in table 6.2, has response in seconds. Present device showed a faster micro second response time close to the response observed in CVD grown ZnO based detector[60]. The improvement observed in the crystallinity of nanorods, (as discussed in chapter 5) may be the reason for the observed improvements on device performance. Present device showed fastest response time for a solution grown ZnO based UV detector.

6.4 Conclusions

Ag/GaN:Mg/ZnO nanorod/Au heterojunction devices were successfully fabricated. The fabricated devices showed good rectifying behavior. The V-I characteristics of the heterojunction was studied and junction parameters were extracted. Based on V-I and PL analyses, a band diagram of the device is proposed.

The heterojunction emitted light under forward bias. From the EL studies it is clear that the defect states in the semiconductor plays a crucial role on the quality of emitted light. Altering the defect states in the semiconductor can result in tuning of emission wavelength. The heterojunction showed both light detection and light emission properties.

Heterojunction device showed increasing current on UV illumination. The anomalous V-I characteristics found on forward bias under UV illumination is explained using tunneling modes. The fastness of the heterojunction devices were determined by calculating the response timings. Photoresponse studies revealed that the device has highly selective UV response which can be utilized for UV detector applications.

The study gave clear idea on light emission from p-GaN/n-ZnO heterojunction. The emission wavelength tuning was demonstrated. Simple process for fabrication of the p-GaN/n-ZnO heterojunction is demonstrated. The device shows very fast response with stable UV and dark photo current levels. Heterojunctions un-

der the present study showed faster response and stable UV and dark response levels compared to other previous reports[44]. Present device has second fastest response time among the ZnO nanorod based photodetector and it has fastest response time for a solution grown ZnO nanorod based UV photodetector.

6.5 References

[1] D.C. Look, B. Claflin, Y.I. Alivov, S.J. Park, Phys. Status Solidi A,201 (2004), 2203.

[2] G.D. Yuan, W.J. Zhang, J.S. Jie, X. Fan, J.A. Zapien, Y.H. Leung, L.B. Luo, P.F. Wang, C.S. Lee, S.T. Lee, Nano Lett. 8 (2008) 2591.

[3] Y.S. Choi, J.W. Kang, D.K. Hwang, S.J. Park, IEEE Trans. Electron Devices 57 (2010) 26.

[4] J. Bao, M. a Zimmler, F. Capasso, X. Wang, Z.F. Ren, Nano Lett. 6 (2006) 1719.

[5] Y. He, J. Wang, W. Zhang, X. Chen, Z. Huang, Q. Gu, J. Phys. Conf. Ser. 152 (2009) 012054.

[6] J.Y. Wang, C.Y. Lee, Y.T. Chen, C.T. Chen, Y.L. Chen, C.F. Lin, Y.F. Chen, Appl. Phys. Lett. 95 (2009) 131117.

[7] Y.Y. Xi, Y.F. Hsu, A.B. Djurišić, A.M.C. Ng, W.K. Chan, H.L. Tam, K.W. Cheah, Appl. Phys. Lett. 92 (2008) 113505.

[8] M.A. Abbasi, Z.H. Ibupoto, M. Hussain, O. Nur, M.

Willander, Nanoscale Res. Lett. 8 (2013) 320.

[9] L.S. Vikas, K.C. Sanal, M.K. Jayaraj, A. Antony, J. Puigdollers, Phys. Status Solidi A 211 (2014) 2493.

[10] S. Jung, K. Yong, Chem. Commun. 47 (2011) 2643.

[11] a. Zainelabdin, S. Zaman, G. Amin, O. Nur, M. Willander, Appl. Phys. A 108 (2012) 921.

[12] S. Wang, C. Hsiao, S. Chang, S. Member, Z.Y. Jiao, S. Young, IEEE Trans. Nanotechnol. 12 (2013) 263.

[13] L. Zhang, F. Zhao, C. Wang, F. Wang, R. Huang, Q. Li, Electron. Mater. Lett. 11 (2015) 682.

[14] A. Tsukazaki, M. Kubota, A. Ohtomo, T. Onuma, K. Ohtani, H. Ohno, S.F. Chichibu, M. Kawasaki, Jap. J. Appl. Phys. 44 (2005) L643.

[15] R. Könenkamp, R.C. Word, M. Godinez, Nano Lett. 5 (2005) 2005.

[16] U. Özgür, Y.I. Alivov, C. Liu, A. Teke, M.A. Reshchikov, S. Doğan, V. Avrutin, S.J. Cho, H. Morkoç, J. Appl. Phys. 98 (2005) 041301.

[17] O. Lupan, T. Pauporté, B. Viana, Adv. Mater. 22 (2010) 3298.

[18] D.J. Rogers, F. Hosseini Teherani, A. Yasan, K. Minder, P. Kung, M. Razeghi, Appl. Phys. Lett. 88 (2006) 141918.

[19] S. Jha, C.D. Wang, C.Y. Luan, C.P. Liu, H. Bin, O.

Kutsay, I. Bello, J. a. Zapien, W.J. Zhang, S.T. Lee, J. Electron. Mater. 41 (2012) 853.

[20] B. Viana, T. Pauporte, O. Lupan, L. Devis, T. Gacoin, Proc. SPIE 8987 (2014) 89871T.

[21] O. Lupan, T. Pauporté, L. Chow, G. Chai, B. Viana, V.V. Ursaki, E. Monaico, I.M. Tiginyanu, Appl. Surf. Sci. 259 (2012) 399.

[22] S.J. Jiao, Z.Z. Zhang, Y.M. Lu, D.Z. Shen, B. Yao, J.Y. Zhang, B.H. Li, D.X. Zhao, X.W. Fan, Z.K. Tang, Appl. Phys. Lett. 88 (2006) 031911.

[23] C.H. Chen, S.J. Chang, S.P. Chang, M.J. Li, I.C. Chen, T.J. Hsueh, A. Di Hsu, C.L. Hsu, J. Phys. Chem. C 114 (2010) 12422.

[24] L. Zhang, Q. Li, C. Qu, Z. Zhang, R. Huang, F. Zhao, J. Opt. 15 (2013) 025003.

[25] M.C. Jeong, B.Y. Oh, M.H. Ham, S.W. Lee, J.M. Myoung, Small 3 (2007) 568.

[26] X. Chen, A. Man Ching Ng, F. Fang, Y. Hang Ng, A.B. Djurišić, H. Lam Tam, K. Wai Cheah, S. Gwo, W. Kin Chan, P. Wai Keung Fong, H. Fei Lui, C. Surya, J. Appl. Phys. 110 (2011) 094513.

[27] A.M.C. Ng, X.Y. Chen, F. Fang, Y.F. Hsu, A.B. Djurišić, C.C. Ling, H.L. Tam, K.W. Cheah, P.W.K. Fong, H.F. Lui,

C. Surya, W.K. Chan, Appl. Phys. B 100 (2010) 851.

[28] K.H. Dai, L.S. Wang, D.X. Huang, C.B. Soh, S.J. Chua, Chinese Phys. Lett. 28 (2011) 098501.

[29] S.W. Lee, H.D. Cho, G. Panin, T. Won Kang, Appl. Phys. Lett. 98 (2011) 093110.

[30] S. Xu, C. Xu, Y. Liu, Y. Hu, R. Yang, Q. Yang, J.-H. Ryou, H.J. Kim, Z. Lochner, S. Choi, R. Dupuis, Z.L. Wang, Adv. Mater. 22 (2010) 4749.

[31] X. Wang, J. Cole, A.M. Dabiran, H.O. Jacobs, NSTI-Nanotech 2007 4 (2007) 526.

[32] A.M.C. Ng, Y.Y. Xi, Y.F. Hsu, a B. Djurisić, W.K. Chan, S. Gwo, H.L. Tam, K.W. Cheah, P.W.K. Fong, H.F. Lui, C. Surya, Nanotechnology 20 (2009) 445201.

[33] K.S. Kim, S.M. Kim, H. Jeong, M.S. Jeong, G.Y. Jung, Adv. Funct. Mater. 20 (2010) 1076.

[34] K.K. Kim, S. dong Lee, H. Kim, J.C. Park, S.N. Lee, Y. Park, S.J. Park, S.W. Kim, Appl. Phys. Lett. 94 (2009) 071118.

[35] Z. Yin, X. Liu, H. Yao, Y. Wu, X. Hao, M. Han, X. Xu, IEEE Photonic Technol. Lett. 25 (2013) 1989.

[36] J.H. Wu, S.Y. Liu, S. Li, Y. long Jiang, G.P. Ru, X.P. Qu, Appl. Phys. A 109 (2012) 489.

[37] F. Schuster, B. Laumer, R.R. Zamani, C. Magén, J.R.

Morante, J. Arbiol, M. Stutzmann, ACS Nano 8 (2014) 4376.

[38] C.F. Du, C.H. Lee, C.T. Cheng, K.H. Lin, J.K. Sheu, H.C. Hsu, Nanoscale Res. Lett. 9 (2014) 446.

[39] Z. Bi, J. Zhang, X. Bian, D. Wang, X. Zhang, W. Zhang, X. Hou, J. Electron. Mater. 37 (2007) 760.

[40] Z. Xu, H. Deng, J. Xie, Y. Li, Y. Li, X. Zu, S. Xue, J. Sol-Gel Sci. Technol. 36 (2005) 223.

[41] V.A. Krivchenko, D. V. Lopaev, P. V. Pashchenko, V.G. Pirogov, A.T. Rakhimov, N. V. Suetin, A.S. Trifonov, Tech. Phys. 53 (2008) 1065.

[42] Y.S. Choi, J.Y. Lee, S. Im, S.J. Lee, J. Vac. Sci. Technol. B 2384 (2011) 10.

[43] M. Ding, D. Zhao, B. Yao, Q. Qiao, X. Xu, Appl. Phys. A 118 (2014) 1267.

[44] E. Przeździecka, K. Gościński, M. Stachowicz, D. Dobosz, E. Zielony, J.M. Sajkowski, M.A. Pietrzyk, E. Płaczek-Popko, A. Kozanecki, Sensors Actuators A Phys. 195 (2013) 27.

[45] J. Chen, L. Ding, X. Zhang, L. Chu, N. Liu, Opt. Express 22 (2014) 7090.

[46] S.N. Das, K.J. Moon, J.P. Kar, J.H. Choi, J. Xiong, T. Il Lee, J.M. Myoung, Appl. Phys. Lett. 97 (2010) 022103.

[47] C.L. Wei, Y.C. Chen, C.C. Cheng, K.S. Kao, D.L. Cheng, P.S. Cheng, Thin Solid Films 518 (2010) 3059.

[48] X. Zhang, X. Han, J. Su, Q. Zhang, Y. Gao, Appl. Phys. A 107 (2012) 255.

[49] H. Kind, H. Yan, B. Messer, M. Law, P. Yang, Adv. Mater. 14 (2002) 158.

[50] S.S. Hullavarad, N. V. Hullavarad, P.C. Karulkar, A. Luykx, P. Valdivia, Nanoscale Res. Lett. 2 (2007) 161.

[51] S. Hullavarad, N. Hullavarad, D. Look, B. Claflin, Nanoscale Res. Lett. 4 (2009) 1421.

[52] A. Bera, D. Basak, Appl. Phys. Lett. 94 (2009) 2009.

[53] H.K. Yadav, K. Sreenivas, V. Gupta, J. Appl. Phys. 107 (2010) 1.

[54] A. Bera, D. Basak, ACS Appl. Mater. Interfaces 2 (2010) 408.

[55] J. Liu, J. Park, K.H. Park, Y. Ahn, J.Y. Park, K.H. Koh, S. Lee, Nanotechnology 21 (2010) 485504.

[56] M.W. Chen, C.Y. Chen, D.H. Lien, Y. Ding, J.H. He, Opt. Express 18 (2010) 14836.

[57] H. Chang, Z. Sun, K.Y.F. Ho, X. Tao, F. Yan, W.M. Kwok, Z. Zheng, Nanoscale 3 (2011) 258.

[58] D.C. Kim, B.O. Jung, J.H. Lee, H.K. Cho, J.Y. Lee, J.H. Lee, Nanotechnology 22 (2011) 265506.

[59] S. Dhara, P. Giri, Nanoscale Res. Lett. 6 (2011) 504.

[60] Y.Q. Bie, Z.M. Liao, H.Z. Zhang, G.R. Li, Y. Ye, Y.B. Zhou, J. Xu, Z.X. Qin, L. Dai, D.P. Yu, Adv. Mater. 23 (2011) 649.

[61] Q. Humayun, M. Kashif, U. Hashim, A. Qurashi, Nanoscale Res. Lett. 9 (2014) 29.

[62] F. Yi, Q. Liao, X. Yan, Z. Bai, Z. Wang, X. Chen, Q. Zhang, Y. Huang, Y. Zhang, Phys. E Low-Dimensional Syst. Nanostructures 61 (2014) 180.

[63] B.A. Albiss, M.A. AL Akhras, I. Obaidat, Int. J. Environ. Anal. Chem. 95 (2015) 339.

[64] V.Q. Dang, T.Q. Trung, D. Il Kim, L.T. Duy, B.U. Hwang, D.W. Lee, B.Y. Kim, L.D. Toan, N.E. Lee, Small (2015) 3054.

[65] Q. Humayun, U. Hashim, C.M. Ruzaidi, K.L. Foo, IOP Conf. Ser. Mater. Sci. Eng. 99 (2015) 012017.

[66] Y.H. Ko, G. Nagaraju, J.S. Yu, Nanoscale Res. Lett. 10 (2015) 1032.

[67] N. Al Hardan, M. Abdul Hamid, N. Ahmed, A. Jalar, R. Shamsudin, N. Othman, L. Keng, S. Mohammad, IEEE Sens. J. 15 (2015) 8611.

[68] L.S. Vikas, K.A. Vanaja, P.P. Subha, M.K. Jayaraj, Sensors Actuators A Phys. 242 (2016) 116.

[69] J.O. Song, D.S. Leem, Y. Park, S.W. Chae, T.Y. Seong, IEEE Photonics Technol. Lett. 17 (2005) 291.

[70] J.O. Song, H.G. Hong, J.W. Jeon, J.I. Sohn, J.S. Jang, T.Y. Seong, Electrochem. Solid-State Lett. 11 (2008) H36.

[71] U. Kaufmann, M. Kunzer, M. Maier, H. Obloh, A. Ramakrishnan, B. Santic, P. Schlotter, Appl. Phys. Lett. 72 (1998) 1326.

[72] B. Monemar, P.P. Paskov, G. Pozina, C. Hemmingsson, J.P. Bergman, S. Khromov, V.N. Izyumskaya, V. Avrutin, X. Li, H. Morkoç, H. Amano, M. Iwaya, I. Akasaki, J. Appl. Phys. 115 (2014) 053507.

[73] B. Monemar, S. Khromov, G. Pozina, P. Paskov, P. Bergman, C. Hemmingsson, L. Hultman, H. Amano, V. Avrutin, X. Li, H. Morkoç, Jpn. J. Appl. Phys. 52 (2013) 08JJ03.

[74] M. Gomi, N. Oohira, K. Ozaki, M. Koyano, Jpn. J. Appl. Phys. 42 (2003) 481.

[75] C.H. Ahn, Y.Y. Kim, D.C. Kim, S.K. Mohanta, H.K. Cho, J. Appl. Phys. 105 (2009) 013502.

[76] P.A. Rodnyi, I. V. Khodyuk, Opt. Spectrosc. 111 (2011) 776.

[77] B. Lin, Z. Fu, Y. Jia, Appl. Phys. Lett. 79 (2001) 943.

[78] L. Esaki, Phys. Rev. 109 (1957) 603.

[79] G. Moaga, Appl. Opt. 40 (2001) 6086.

[80] D. Thomas A, D.P. Knott, Solid. State. Electron. 13 (1970) 131.

[81] D.K. Roy, Solid. State. Electron. 14 (1970) 520.

[82] M.C. Jeong, B.Y. Oh, M.H. Ham, S.W. Lee, J.M. Myoung, Small 3 (2007) 568.

[83] J.M. Myoung, K.H. Shim, C. Kim, O. Gluschenkov, K. Kim, S. Kim, D. a. Turnbull, S.G. Bishop, Appl. Phys. Lett. 69 (1996) 2722.

[84] M.K. Wu, Y.T. Shih, W.C. Li, H.C. Chen, M.J. Chen, H. Kuan, J.R. Yang, M. Shiojiri, IEEE Photonicss Technol. Lett. 20 (2008) 1772.

[85] Thorlabs, https://www.thorlabs.com/tutorials.cfm?tabID=31760 (2016).

[86] Newport, http://www.newport.com/Tutorial-High-Speed-Detectors/851593/1033/content.aspx (2016).

Chapter 7

Study of dependence of ZnO nanostructures on the light collection ability of Dye sensitized solar cells

7.1 Introduction

The constant search for an alternative renewable energy source led to the development of solar cells. Various techniques have been employed to increase the cell efficiency and to decrease the cost of photovoltaic modules. One such attempt is the dye sensitized solar cell (DSSC) proposed in 1991[1]. In a standard DSSC, photo excited dye molecule injects an electron to the conduction band of TiO_2 semiconductor, which is then transported to the electrode.

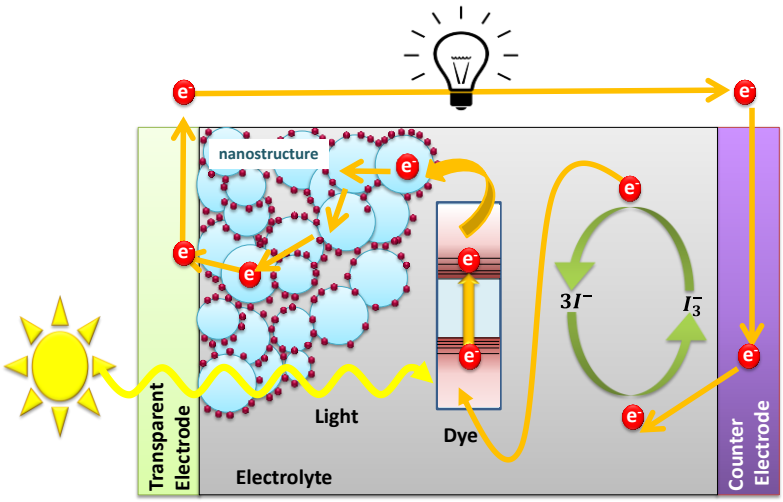

Figure 7.1: Schematic diagram of working of a DSSC.

The photo conversion takes place at the dye-semiconductor interface. Hence, to increase the interface area nonporous TiO_2 is generally used. But, the large number of grain boundaries in a porous nanoparticle network weakens the electron transport process. Also, the growth of anisotropically crystalline and ordered nanostructure TiO_2 is challenging. Hence, the use of ZnO nanostructures such as nanoparticles, nanowire, nanorod, nanobelts, nanosheets, etc. can reduce this limitation to an extent[2–6]. The photo generated electron needs to cross about 10^3 to 10^6 nanoparticles in a nanoparticle based solar cell. The disorder and defects in the nanoparticle network further enhances the scattering of free electrons. Increased scattering due to grain boundaries in the nanoparticle network reduces the effective electron mobility and

increases the electron recombination rate. Replacing the nanoparticle network with a highly crystalline nanorods reduces the grain boundaries, which increases the photo generated charge collection properties[7]. Though, charge transfer path can be refined in nanorod based solar cells, the effective surface area can give further hurdle. The charge transfer in a DSSC occurs at the semiconductor-dye interface. Decreasing the surface area thus can adversely affect the overall efficiency of the solar cell. To increase the surface area in DSSC, the shape and size of the nanostructures were varied.

ZnO was proposed as an effective photoanode by Gerischer and Tributsch even before the development of DSSC[8]. Compared to TiO_2, ZnO has higher electron mobility. At the same time, they both have similar band gap and electron affinity. Due to the higher electron mobility, the number of recombinations will be lesser which makes ZnO a good electron transport material compared with TiO_2[9–12]. Most of the reports on ZnO based DSSCs concentrates on various surface modification techniques. Some studies concentrated on surface decoration with metal nanoparticles and quantum dots, whereas some other studies used different shapes of nanostructures like ZnO nanowires[13], aligned ZnO nanorods[14,15], branched ZnO nanorods[9,16,17], ZnO hierarchical structures[18] etc. Rao et al. reported a solution processed c-axis oriented ZnO nanorod based device showing 3.2% efficiency and a fill factor of 50%[19]. Their studies revealed that UV ozone treat-

ment can improve the device performance. Recent report by Son et. al., showed a remarkable 11% absorbed photon to current conversion efficiency for ZnO based perovskite solar cell[20]. They reported the impact of seed layer on growth of ZnO and its dependence on solar cell efficiency. After successfully tuning the nanorod growth conditions they were able to obtain a photo conversion efficiency of 14%[21]. Even ZnO nanotube based solar cells have already been reported, which possess relatively lesser efficiency of 1.6%[22]. New studies on the use of ZnO nanorods for flexible DSSC cells are really promising[23,24].

In the present study, the dependence of quantum conversion efficiency of DSSC on the shape of nanostructured ZnO photoanode is investigated. The three types of ZnO nanostructures used in this study are ZnO nanoparticles, ZnO nanorods (powder form) and aligned grown ZnO nanorods.

7.2 Experimental

7.2.1 ZnO nanoparticle preparation (Hydrothermal)

The precursor solution containing zinc acetate dihydrate ($Zn(CH_3COO)_2$ $2H_2O$) and sodium hydroxide (NaOH) in distilled water is kept inside a hydrothermal autoclave at 100°C for 1hr. After synthesis, formed nanoparticles were filtered and dried at 60°C in a laboratory oven.

7.2.2 ZnO rod preparation (Hydrothermal)

Similar to nanoparticle preparation, precursor solution of zinc acetate dihydrate ($Zn(CH_3COO)_2$ $2H_2O$ and ammonium hydroxide (NH_4OH) in distilled water were kept inside an autoclave. The autoclave was then kept at 180°C for 1 hour to complete the hydrothermal synthesis. After synthesis, the rods were filtered out and dried at 60°C to obtain ZnO rods in powder form.

7.2.3 Electrodeposition of ZnO nanorod

ZnO nanorods were grown over FTO coated glass substrate(Solaronix) as mentioned in chapter3. An aqueous solution of 0.05 mM $ZnCl_2$ and 0.1 M KCl is used as the electrolyte for the synthesis. In the three terminal electrochemical cell, FTO coated glass plate was working electrode and saturated calomel electrode is used as reference electrode. A Pt wire was used as counter electrode. A suitable electrodeposition voltage of -1.2 V is applied between working electrode and reference electrode. The electrolyte was kept at a temperature of 80°C during growth and constant bubbling of O_2 and constant stirring was performed.

7.2.4 DSSC fabrication

The schematic diagram of DSSC is as shown in figure 7.1. Two FTO coated glass plates (Solaronix) used to fabricate the DSSC. Desired nanostructures are deposited over the FTO coated

glass substrate by doctor blade technique. In the case of electrodeposited samples, the ZnO nanorods were grown directly over the FTO coated glass substrate. After nanostructure deposition, the nanostructure containing glass plate was kept inside a N719 dye (Solaronix) solution to adsorb the dye over the surface of the nanostructures. After staining, the substrate is washed in ethanol to wash out any unwanted dye contents and allowed to dry. A second FTO coated glass plate was taken and Platisol solution (Solaronix) was painted over FTO coated glass plate. The painted substrate is annealed at 450°C for half an hour to get a Pt coated FTO substrate. The two substrates were sandwiched together by keeping their conducting surfaces face to face. A high stability I^-/I^{3-} electrolyte (Iodolyte (Solaronix)) was filled inside the cell to complete the cell structure. Meltronix (Solaronix) thermoplastic materials is kept in between the glass plates to avoid short circuit. The two FTO coated region of the glass plates will work as two electrodes of the solar cell. The final structure of the DSSC was as shown in figure 7.2.

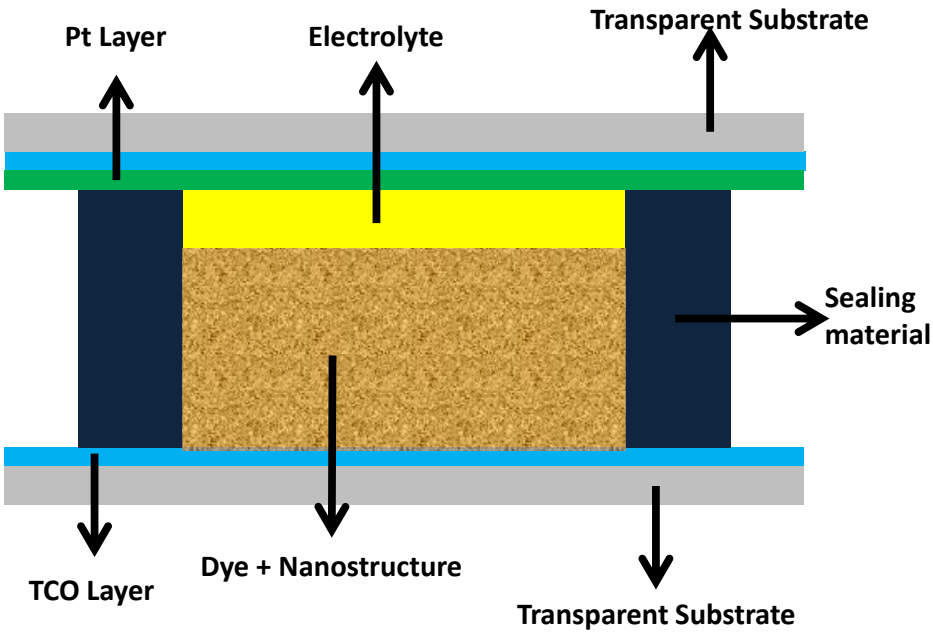

Figure 7.2: The schematic diagram of cross section of a DSSC.

The effect of shape of nanostructures on the charge collection ability in a solar cell was studied by fabricating dye sensitized solar cells. To fabricate reference solar cell, TiO_2 P25 particles (Degussa) were used in the semiconductor layer. The semiconductor layer in DSSCs prepared with ZnO rods and ZnO nanoparticles were named HTrod (for hydrothermally grown ZnO rods) and HTparticle (For hydrothermally grown ZnO particles) respectively. The FTO coated glass substrate with electrodeposited nanorods used to fabricate DSSC and named as EDrod (ED stands for electrodeposition) solar cells. The morphological studies were per-

formed and are correlated with the measured solar cell performance parameters.

7.3 Results and Discussions

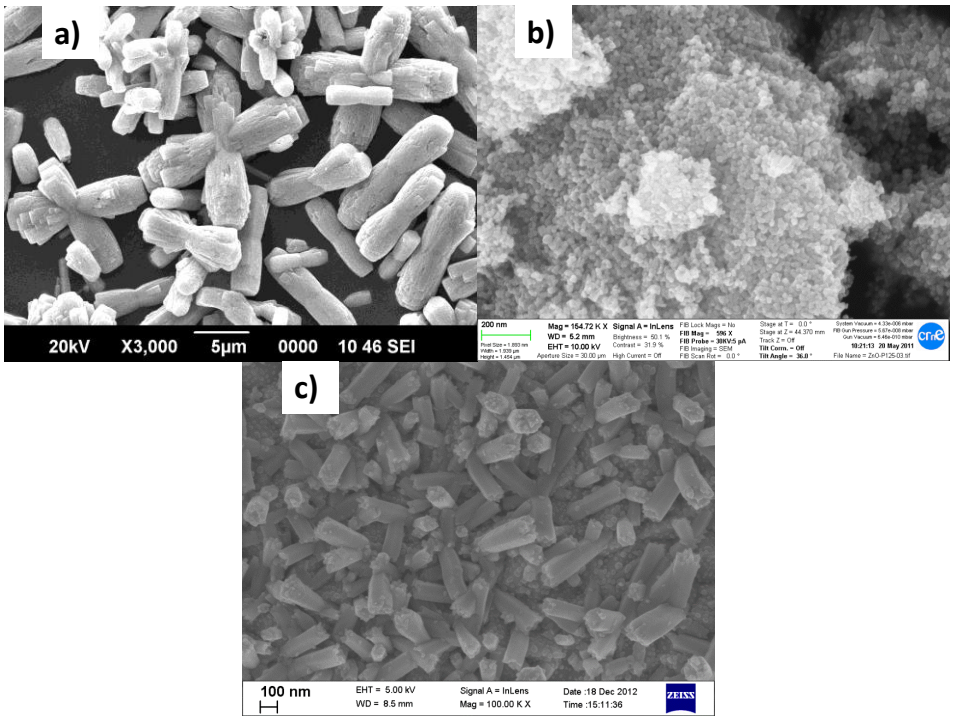

Figure 7.3: The FESEM image hydrothermally synthesized (a)ZnO nanorods, (b) ZnO nanoparticles and electrodeposited (c)ZnO nanorods.

The FESEM images of ZnO nanostructures are shown in figure 7.3. Figure 7.3(a) shows the FESEM image of hydrothermally synthesized ZnO rod which has a length of ~8.25 µm and a

width of ~2 µm. The hydrothermally synthesized ZnO nanoparticles(figure 7.3(b)) showed a particle size of ~25 nm.

The electrodeposition of ZnO over FTO coated glass substrate showed a preferred oriented growth for ZnO nanorods. The nanorods had hexagonal structure. The length of the nanorods were 450±25 nm and the diameter were 130±10 nm.

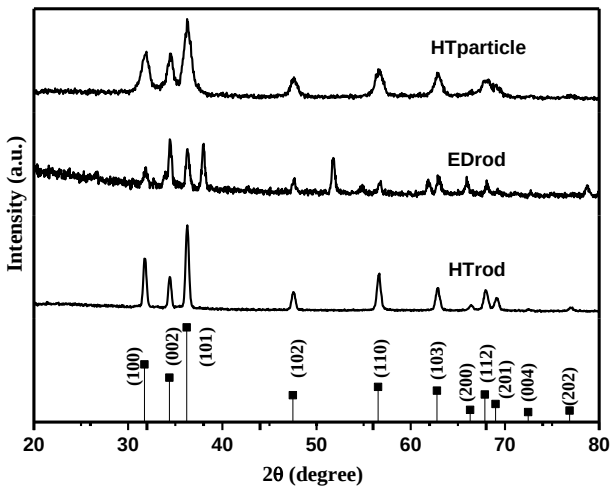

Figure 7.4: X-ray diffraction spectra of different ZnO nanostructures.

The X-ray diffraction spectrum of nanostructures showed wurtzite hexagonal crystal structure. Hydrothermally synthesized ZnO rods shows preferred orientation in (0 0 0 2) direction.

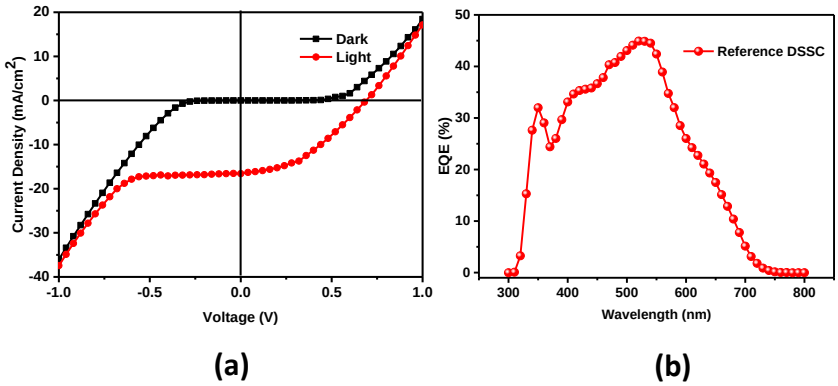

Figure 7.5: (a) The V-I characteristics and (b) external quantum efficiency of the reference DSSC.

The reference solar cell fabricated using TiO_2 P25 nanoparticles showed good cell response. The solar cell showed an efficiency of 4.52% and a fill factor of 39.46%. The open circuit voltage was 0.69 V and the short circuit current density was 16.59 mA/cm^2. The external quantum efficiency of the cells also were studied, which showed a good response from 320nm to 730nm.

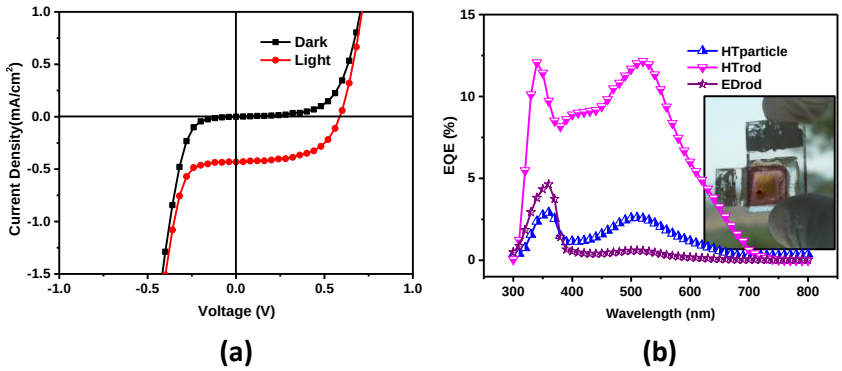

Figure 7.6: (a) The V-I characteristics of HTrod solar cell and (b)the external quantum efficiency of DSSCs fabricated with various nanostructures. Inset of (b) shows the photograph of EDrod DSSC.

Hydrothermally synthesized ZnO rod based DSSC showed the best cell parameters among various ZnO nanostructure based cells as shown in figure 7.6. The cell showed an efficiency of 0.143 % with an open circuit voltage of 590 mV and short circuit current density of 0.43 mA/cm^2. The EQE measurements showed a maximum value for ZnO rod (HTrod) based DSSC. For electrodeposited ZnO nanorod based DSSC the quantum efficiency is too low, which shows poor response in the visible region. Only in the UV region the DSSC showed a peak response. Highly transparent nature of nanorods in EDrod as shown in inset of figure 7.6(b) may be the reason for its poor performance, as high transparency allows majority of photons to pass through the solar cell without absorbing it. For ZnO nanoparticle based DSSC the overall trend of EQE

follows that of reference DSSC yet the efficiency values are very low.

In the case of a nanoparticle based DSSC, the conduction occurs by transferring charge from one grain to the other till it reaches electrode. During this period, the charge carrier needs to face a number of barriers and interfaces. While for ZnO rod (HTrod) based device the photo generated charge carriers face lesser number of barrier interfaces compared to the HTparticle. Hence, the total number of charge reaching electrodes will be lesser. This may be the reason for the observed decrease in quantum efficiency for HTparticle compared to HTrod.

7.4 Conclusions

Dye sensitized solar cells based on different shape ZnO nanostructures were successfully fabricated. Solar cells showed lower quantum efficiency compared to reference DSSC. Among various ZnO nanostructure based cells electrodeposited ZnO based cells showed poor performance. ZnO rod based solar cells showed better quantum efficiency compared to ZnO nanoparticles. This may be due to the better electron transport mechanism in rods compared to nanoparticles. Thus, ZnO rod based solar cells can be a potential candidate for efficient DSSC. Fine tuning this structure may find applications in smart coloured windows.

7.5 References

[1] B. O'Regan, M. Gratzel, Nature 353 (1991) 737.

[2] D.W. Bahnemann, C. Kormann, M.R. Hoffmann, J. Phys. Chem. C 91 (1987) 3789.

[3] N. Karst, G. Rey, B. Doisneau, H. Roussel, R. Deshayes, V. Consonni, C. Ternon, D. Bellet, Mater. Sci. Eng. B 176 (2011) 653.

[4] Q.F. Zhang, C.S. Dandeneau, X.Y. Zhou, G.Z. Cao, Adv. Mater. 21 (2009) 4087.

[5] X. Zhang, J. Solid State Chem. 173 (2003) 109.

[6] F. Zhao, W. Lin, M. Wu, N. Xu, X. Yang, Z.R. Tian, Q. Su, Inorg. Chem. 45 (2006) 3256.

[7] A.B.F. Martinson, J.E. McGarrah, M.O.K. Parpia, J.T. Hupp, Phys. Chem. Chem. Phys. 8 (2006) 4655.

[8] A.B. Kashyout, M. Soliman, M. El Gamal, M. Fathy, Mater. Chem. Phys. 90 (2005) 230.

[9] W.H. Chiu, C.H. Lee, H.M. Cheng, H.F. Lin, S.C. Liao, J.M. Wu, W.F. Hsieh, Energy Environ. Sci. 2 (2009) 694.

[10] N. Karst, G. Rey, B. Doisneau, H. Roussel, R. Deshayes, V. Consonni, C. Ternon, D. Bellet, Mater. Sci. Eng. B 176 (2011) 653.

[11] A. Omar, H. Abdullah, M. a Yarmo, S. Shaari, M.R. Taha, J. Phys. D-Applied Phys. 46 (2013) 8.

[12] L. Lu, R. Li, T. Peng, K. Fan, K. Dai, Renew. Energy 36 (2011) 3386.

[13] A. Omar, H. Abdullah, Renew. Sustain. Energy Rev. 31 (2014) 149.

[14] I. Gonzalez-Valls, M. Lira-Cantu, Energy Environ. Sci. 3 (2010) 789.

[15] A. Yengantiwar, R. Sharma, O. Game, A. Banpurkar, Curr. Appl. Phys. 11 (2011) S113.

[16] J.B. Baxter, E.S. Aydil, Appl. Phys. Lett. 86 (2005) 053114 1.

[17] C.Y. Jiang, X.W. Sun, G.Q. Lo, D.L. Kwong, J.X. Wang, Appl. Phys. Lett. 90 (2007) 263501 1.

[18] R. Zhang, S. Kumar, S. Zou, L.L. Kerr, Cryst. Growth Des. 8 (2008) 381.

[19] A.D. Rao, S. Karalatti, T. Thomas, P.C. Ramamurthy, ACS Appl. Mater. Interfaces 6 (2014) 16792.

[20] D.Y. Son, J.H. Im, H.S. Kim, N.G. Park, J. Phys. Chem. C 118 (2014) 16567.

[21] D.Y. Son, K.H. Bae, H.S. Kim, N.G. Park, J. Phys. Chem. C 119 (2015) 10321.

[22] A.B.F. Martinson, J.W. Elam, J.T. Hupp, M.J. Pellin, Nano Lett. 7 (2007) 2183.

[23] S. Chu, D. Li, P.C. Chang, J.G. Lu, Nanoscale Res. Lett. 6 (2010) 38.

[24] Y. Chae, J.T. Park, J.K. Koh, J.H. Kim, E. Kim, Mater. Sci. Eng. B 178 (2013) 1117.

Chapter 8

Summary and scope for future study

8.1 Summary of the present study

The present work concentrates on aligned growth of ZnO 1D nanostructures and its optoelectronic properties. ZnO is a known oxide semiconductor with promising optoelectronic applications. In recent studies on ZnO, the main emphasis is on applications of nanostructured ZnO. Solution growth techniques are, in general, a simple and economic method for growing ZnO nanostructures. Earlier studies have reported that ZnO nanostructures grown by solution growth techniques had poor crystalline quality compared to vacuum assisted sophisticated techniques like CVD, MOCVD, MBE, VLS, PLD etc. Seed layer is expected to improve ZnO nanorod growth especially in the case of solution growth of ZnO nanorods. As nanorods are used for device fabrication, aligned growth of nanorods over a substrate also plays an important role on optoelectronic properties. In the first part of the thesis, the growth of ZnO nanostructures over different substrates are discussed. Properties affecting the orientation of nanorods were

investigated. The effect of seed layer on nanorod growth and its optoelectronic properties were investigated.

ZnO nanorods were grown by two techniques: (i) electrodeposition and (ii) hydrothermal synthesis. In electrodeposition process, ZnO nanorods were successfully synthesized over four different TCO substrates. It was found that post deposition annealing after electrodeposition process improves the crystallinity of ZnO nanorods, while decreasing its defect states. The oriented growth of ZnO nanorods depends on the substrate surface and its lattice. For a substrate with high lattice mismatch, as the roughness of the substrate surface decreases, the preferred orientation of nanorods increases. The density of nanorods found to increase with ZnO seed layer thickness. At the same time the dimensions of the nanorods (length and breadth) decreases with seed layer thickness. Thus for substrate with lattice mismatch, the roughness of the substrate along with its modification by seed layer decides the orientation of ZnO nanorods grown over it. For substrates with lattice matching, highly preferred oriented growth of nanorods irrespective of the substrate roughness was observed. The nanorod dimensions, density of nanorods and preferred orientation were found to be almost constant in this case.

Heterojunction devices were fabricated using p-CuO layer over the electrodeposited nanorods. To study the effect of seed layer on the electrical properties, one set of devices with seed layer and another set with nanorods grown directly over the substrate (without seed layer) were fabricated. All heterojunction devices showed rectifying nature. The series resistance of devices with seed layer was 24 kΩ, while that of devices without seed layer was 17 kΩ. This indicates that seed layer is giving additional series re-

sistance to the overall electrical performance of the device. Fabricated heterojunction device showed a selective response to UV light. The rise time of the device was found to be faster compared to decay time. The large decay time is expected to be because of the slow decay process due to the presence of defect states in the material.

Growth of ZnO nanorods on epitaxially matched GaN:Mg single crystal substrate was performed using hydrothermal synthesis. Introduction of sputter deposited ZnO seed layer over the GaN:Mg substrate showed poor crystalline quality and orientation of ZnO nanorods. Detailed analysis by high resolution X-ray diffraction studies revealed highly oriented ZnO nanorod growth, when nanorods are grown directly over the substrate without seed layer. In this case, the nanorods followed the crystal structure of GaN:Mg substrate without any tilting or twinning. Reciprocal space mapping and pole figure analysis confirmed the growth of epitaxial ZnO nanorods. Photoluminescence study revealed the dramatic reduction of defect states in ZnO nanorods on annealing in air.

Electrical studies of n-ZnO/p-GaN:Mg heterojunction showed a rectifying behaviour. Introduction of seed layer for ZnO nanorod growth over the substrate is again giving a series resistance to the device. The devices showed light emission and detection properties. As grown nanorod based devices without post deposition annealing showed white light emission. For devices with annealed nanorods as its defect states are largely reduced, the emission shifted from white to UV. Response of the device towards light showed selective nature in UV wavelength region. Device responded very fast to chopped UV light from a He-Cd laser. The

rise and decay time showed response in micro seconds time scale. The fastest response is obtained for 4V biasing with ~300 μs rise and decay time. The observed response is the fastest response for a solution processed ZnO nanorod based UV detector.

The effect of shape of nanostructures on the light collection ability is evaluated using a dye sensitized solar cell (DSSC). Different ZnO structures are used for mesoporous semiconductor layer in DSSC. Hydrothermally synthesized ZnO rods show better charge collection ability compared to hydrothermally synthesized ZnO nanoparticles or electrodeposited ZnO rods. The results indicate the promising nature of ZnO nanorods for DSSC applications.

8.2 Scope for future work

ZnO nanorods showed promising optoelectronic properties, but the aging effect on the performance and stability of these heterojunction devices need to be performed before practical deployment. One challenge with vertically aligned ZnO nanorod based devices is the high leakage current (or low rectification ratio), which can be improved by encapsulating the inter nanorod gap with suitable material. Packaging the fabricated device may be performed for easy integration in practical circuits. Present study used an array of nanorods for heterojunction device fabrication. Single ZnO nanorod based heterojunction device may be fabricated and its properties can be compared with the array of nanorod based devices. Heterojunction devices of ZnO nanorods can be fabricated over various flexible substrates to investigate the effectiveness of a transparent flexible device.